# Advanced Nonintrusive Load Monitoring System



by

Warit Wichakool

S.B. Massachusetts Institute of Technology (2001)
M.Eng. Massachusetts Institute of Technology (2001)



Submitted to the Department of Electrical Engineering and Computer Science
in partial fulfillment of the requirements for the degree of

Doctor of Philosophy

at the

Massachusetts Institute of Technology

February 2011



Author _____
Department of Electrical Engineering and Computer Science
January 5, 2011

Certified by _____
Steven B. Leeb
Professor of Electrical Engineering and Computer Science
Thesis Supervisor

Accepted by _____
Terry P. Orlando
Chairman, Departmental Committee on Graduate Theses

# Acknowledgments

I would like to acknowledge many individuals and organizations for their valuable assistance throughout the course of this thesis work. Without them, this work would not have been successful.

First of all, I would like to thank Professor Steven Leeb, my advisor, for his guidance throughout my study. Professor Leeb has been one of the greatest mentor I have ever met. His advises have improve myself professionally and personally.

Next, I would like to thank my thesis committee: Professor Leslie K. Norford, Professor James L. Kirtley, and Professor David J. Perreault for their recommendations and suggestions regarding the thesis work. Their questions and comments have make the thesis more completed.

In addition, I would like to extend my acknowledgments to many LEES friends and colleagues. I would like to thank Robert Cox, Al-Thaddeus Avestruz, Jim Paris, Christopher Laughman, John Cooley, Zachery Remscrim, Chris Schantz, Amy Englehart, and Uzoma Orji for their contributions to my works. Also, I would like to thank them for many great times in LEES. Also, I would like to thank David Otten, Brandon Pierquet, Robert Pilawa, William Richoux, Anthony Sagneri, George Hwang, Benjamin Cannon, Jackie Hu, Jiankang Wang, Makiko Wada, Vivian Mizuno, and many LEE for making LEES a great place to work and live throughout my stay at MIT.

Furthermore, I would like to thanks many friends: Numpon Insin, Chakrapan Tuakta, Jin Suntivich, Pin Anupongongarch, Wisuwat Songnuan, Petch Jearanaisilawong, Piyatida Hoisungwan, Arance Techawiboonwong, Sirimas Sudsakorn, Sappinandana Akamphon, Yotsawan Chaturapornkul, Nisanart Chalcarnlarp, Wang Nuitragool, Lalita Chanwongpaisarn, Yui Sanchatjate, Patcharee Srisawasdi, Sira Srisawasdi, Somponnat Sampattavanich, Siwanon Jirawatnotai, and many others for being great friends throughout the great time I have spent throughout the U.S.

# Advanced Nonintrusive Load Monitoring System

by

Warit Wichakool

Submitted to the Department of Electrical Engineering and Computer Science
on January 5, 2011, in partial fulfillment of the
requirements for the degree of
Doctor of Philosophy

## Abstract

There is a need for flexible, inexpensive metering technologies that can be deployed in many different monitoring scenarios. Individual loads may be expected to compute information about their power consumption. Utility providers, facilities managers, and other consumers will likely find innumerable ways to mine information if made available in a useful form. However, appropriate sensing and information delivery systems remain a chief bottleneck for many applications, and metering hardware and access to metered information will likely limit the implementation of new electric energy conservation strategies in the near future.

This thesis presents solutions for two long standing problems in nonintrusive power and diagnostic monitoring. First, a high-resolution, physically windowed sensor architecture that is well-suited for energy score-keeping and diagnostic applications will be discussed. The sensor can track a large-scale main signal while capturing small-scale variations. The prototype system uses digital techniques to reconstruct an observed current with a high effective bit resolution. The sensor measures a small current signal using a closed-loop Hall sensor, and extends the range by driving a compensation current with a high performance current source through an auxiliary winding. The system combines the compensation command and the sampled output of the residual sensor to reconstruct the input signal with high bit resolution and bandwidth.

Second, a long-standing problem in nonintrusive power monitoring involves the tracking of power consumption in the in the presence of loads with a continuously variable power demand. Two new techniques have been developed for automatically disaggregating, in real-time, different classes of continuously variable power electronic loads which draw distorted line currents. Experimental results of the proposed power estimator extracting the power consumption of common variable power loads such as a variable speed drive, a computer, and a light dimmer are presented.

Thesis Supervisor: Steven B. Leeb
Title: Professor of Electrical Engineering and Computer Science

I am also greatly thankful for my family for their encouragement and support through all my life.

Finally, I would like to thank many sponsors including Thai Government for the financial support and more importantly the opportunity to pursue the study at M.I.T.

# Contents


**1 Introduction** **13**
- 1.1 Nonintrusive load Monitoring . . . 14
- 1.2 Scalability . . . 23
- 1.3 Challenges . . . 24
- 1.4 Thesis Organization . . . 25

**2 Physically-Windowed Sensor** **28**
- 2.1 Introduction . . . 28
- 2.2 System Design . . . 29
  - 2.2.1 Current Measurement . . . 29
  - 2.2.2 System Architecture . . . 32
  - 2.2.3 Signal Reconstruction . . . 34
  - 2.2.4 Resolution and Range . . . 36
  - 2.2.5 Windowing . . . 37
  - 2.2.6 Bandwidth . . . 38
- 2.3 Benefits and Motivation . . . 39
  - 2.3.1 Resolution . . . 40
  - 2.3.2 Bandwidth . . . 40
- 2.4 Prototype Implementation . . . 42
  - 2.4.1 Closed-Loop Hall Sensor . . . 43
  - 2.4.2 Clamp Circuit . . . 45
  - 2.4.3 Residual Current Measurement . . . 45
  - 2.4.4 Compensation Current . . . 47
  - 2.4.5 Microcontroller . . . 49
    - 2.4.5.1 Sampling . . . 49
    - 2.4.5.2 Windowing Strategy . . . 51
    - 2.4.5.3 Communication . . . 52
    - 2.4.5.4 Calibration . . . 52
- 2.5 Prototype Results . . . 53
  - 2.5.1 Full system functionality . . . 53
  - 2.5.2 Static resolution tests . . . 55

2.5.3 Dynamic resolution tests . . . 57
2.5.4 Residual sensor transient response . . . 57
2.6 Summary . . . 60

**3 Variable Speed Drive Power Estimator** **61**
3.1 Introduction . . . 61
3.2 Background . . . 63
3.3 VSD Model . . . 68
3.4 Switching Function . . . 71
3.5 Estimator Derivation . . . 75
3.5.1 Switching Function Approximation . . . 75
3.5.1.1 Ideal Switching Function . . . 76
3.5.1.2 Approximated Switching Function . . . 78
3.5.2 Dc-side Harmonics Approximation . . . 80
3.5.3 Estimator Coefficients . . . 87
3.6 Results and Discussion . . . 88
3.6.1 Balanced Input Voltage Cases . . . 89
3.6.2 Distorted input voltage cases . . . 89
3.7 Summary . . . 95

**4 Waveform-Based Estimator** **96**
4.1 Introduction . . . 96
4.2 Background . . . 98
4.3 Waveform-Based Estimator . . . 107
4.4 Estimator Derivation . . . 109
4.4.1 Signal Constraints . . . 110
4.4.2 Matrix Equation . . . 116
4.4.3 Reduced Row Echelon Form . . . 117
4.4.4 Estimator Evaluation . . . 118
4.4.5 Numerical Instability . . . 121
4.5 Cyclotomic Field Representation . . . 123
4.5.1 Roots of Unity . . . 123
4.6 Experimental Results . . . 126
4.6.1 Variable Speed Drive . . . 127
4.6.2 Computer . . . 130
4.6.3 Light Dimmer . . . 132
4.7 Summary . . . 136

**5 Conclusion and Future Work** **140**

A Circuit Schematic for Physically-Windowed Sensor 145

B Computations of weighting coefficients for the VSD estimator 158

C Waveform-Based Estimator Program 161

# List of Figures


1.1 Coast Guard Cutter *USCGC Escanaba* . . . . . 16
1.2 Simplified block diagram of a NILM system . . . . . 17
1.3 NILM sensing hardware . . . . . 18
1.4 Current sensor installation . . . . . 18
1.5 Turn-on transient of an induction motor . . . . . 19
1.6 Turn-on transient of an incandescent lamp . . . . . 19
1.7 Power consumed by the three-phase induction motor . . . . . 21
1.8 Real power consumed by the incandescent light bulb . . . . . 21

2.1 Examples of isolated current sensors . . . . . 30
2.2 System block diagram of the physically-windowed sensor . . . . . 32
2.3 Example of a signal reconstruction for the physically-windowed sensor 33
2.4 Detailed block diagram of the prototype system. . . . . 34
2.5 Overlap of the DAC output, relating to compensation current, and the ADC input, relating to the residual measurement . . . . . 36
2.6 Detailed block diagram of the prototype system. . . . . 43
2.7 Full system block diagram . . . . . 43
2.8 Circuit diagram of the customized closed-loop Hall sensor and the active clamp . . . . . 44
2.9 System block diagram of the closed-loop Hall sensor . . . . . 44
2.10 Calibration curves showing 11-bit residual current measurement versus 10-bit compensation current command, at various fixed primary currents 46
2.11 Compensation current driver circuit diagram . . . . . 47
2.12 Output stage of the compensation current subsystem, showing the OTA implementation . . . . . 48
2.13 Prototype implementation . . . . . 50
2.14 Windowing approach in the prototype implementation . . . . . 51
2.15 Oscilloscope traces showing the measured primary, compensation, and residual measurement currents while the prototype physically windowed current sensor is in a normal operation . . . . . 54

2.16 Reconstructed current from the prototyped sensor . . . . . 55
2.17 Histogram of the measured errors during a test of dc performance . . 56
2.18 Example of measuring a small dc current on top of a large ac current 58
2.19 System response during a high current transient . . . . . 59

3.1 A snapshot of the line current consumed by an incandescent light bulb and a VSD over one cycle of the line voltage from the experimental setup 65
3.2 Experiment result showing the power consumption of a VSD, a three-phase rectifier, and an incandescent light bulb . . . . . 65
3.3 Experimental result showing the in-phase components of harmonic currents consumed by the VSD and three-phase rectifier. . . . . 66
3.4 Experimental data and the correlation function between the in-phase component of the fundamental and the fifth harmonics used to derive the empirically-based estimator. . . . . 67
3.5 Block diagram of the model-based VSD power estimator . . . . . 68
3.6 A simple circuit model of the VSD equipped with an uncontrolled rectifier used to simulate the VSD current waveforms . . . . . 69
3.7 Reference input voltage and simulated line current consumed by the three-phase uncontrolled rectifier . . . . . 70
3.8 Examples of the dc-bus current, the switching function, and the ac-side current when the input voltages are balanced and the VSD system is operating in a steady state from the simulation . . . . . 71
3.9 The process of computing the line current harmonic as a modulation of the dc-bus current by the switching function . . . . . 74
3.10 Block diagram showing the process of estimating the VSD fundamental harmonic current from a set of higher harmonic currents . . . . . 76
3.11 Simulation results showing the ideal switching function for phase-A current and the ideal three-phase voltage when the input voltages are balanced . . . . . 77
3.12 Simulation results showing the non-ideal input voltage and approximated switching function for the phase-A current . . . . . 79
3.13 Simulated dc-bus current of the VSD three-phase uncontrolled rectifier 81
3.14 Simulated dc-side harmonic current of the three-phase uncontrolled rectifier normalized by the averaged value of the dc-side current . . . 82

3.15 Examples of dc-bus and ac-side current waveforms in a general case. . 85
3.16 Experimental setup . . . . . 88
3.17 Experimental results of the VSD power estimator resolving the power consumption of VSD and rectifier from the 50-W incandescent light bulb under balanced input voltages . . . . . 90
3.18 Experimental result showing the estimated power of the 50-W light bulb after the empirically-based estimator has removed power of the VSD and the rectifier under the balanced input voltages . . . . . 91
3.19 Experimental results showing the estimation errors in the VSD real power prediction using when the input voltages are distorted with different levels of fifth harmonic . . . . . 92
3.20 Experimental results showing the estimation errors in the VSD real power prediction using different VSD power estimators when the input voltages are distorted with different levels of seventh harmonic . . . . 93
3.21 Experimental results showing the estimation errors in the VSD real power prediction using the model-based estimator with four input harmonics . . . . . 94

4.1 Simulated current waveforms and normalized harmonic currents of a variable speed drive . . . . . 100
4.2 Experimental current waveforms and normalized harmonic currents of a computer . . . . . 101
4.3 Experimental current waveforms and normalized harmonic currents of an incandescent light dimmer . . . . . 102
4.4 Correlation functions of the harmonic currents of the computer . . . . 103
4.5 Real and reactive power consumed by the light dimmer . . . . . 104
4.6 Correlation functions of the harmonic currents of the light dimmer . . 105
4.7 Current waveforms of multiple variable power loads . . . . . 106
4.8 Regions of zero-current of the VSD . . . . . 111
4.9 Estimator evaluation error plots . . . . . 120
4.10 Floating-point arithmetic errors . . . . . 122
4.11 Complex exponentials roots for $N = 12$ . . . . . 125
4.12 Experimental setup for testing the VSD estimator . . . . . 128
4.13 Demonstration the waveform-based estimator extracting the real power consumption of the VSD from the incandescent light . . . . . 129

4.14 Regions of zero-current of the computer . . . . . 131
4.15 Experimental setup for testing the computer estimator . . . . . 132
4.16 Demonstration of the waveform-based estimator extracting the real power consumption of the computer from the incandescent light. . . . 133
4.17 Regions of zero-current of the light dimmer . . . . . 134
4.18 Experimental setup for testing the light dimmer estimator . . . . . 136
4.19 Demonstration the waveform-based estimator extracting the real power consumption of the light dimmer from the incandescent light . . . . . 137
4.20 Demonstration the waveform-based estimator extracting the real power consumption of the light dimmer from the incandescent light. . . . . 138

A.1 Schematic of the control power . . . . . 146
A.2 Schematic of the unregulated power supply . . . . . 147
A.3 Schematic of the power supply for the control circuit . . . . . 148
A.4 Schematic of the command voltage . . . . . 149
A.5 Schematic of the digital-to-analog converter (DAC) . . . . . 150
A.6 Schematic of the DAC isolation circuit and the microcontroller power supply . . . . . 151
A.7 Schematic of the USB peripheral . . . . . 152
A.8 Schematic of the microcontroller connection . . . . . 153
A.9 Schematic of the 12-bit analog-to-digital converter (ADC) . . . . . 154
A.10 Schematic of the 12-bit ADC isolation circuit . . . . . 155
A.11 Schematic of the the 24-bit ADC . . . . . 156
A.12 Schematic of the 24-bit ADC isolation circuit . . . . . 157

C.1 Pseudo-code for the waveform-based estimator . . . . . 162

# *Chapter 1*

# *Introduction*

The U.S. government realizes the importance of the electricity sector and its future, the Energy Independent and Security Act of 2007 has been passed to encourage and focus the effort to improve the current electricity grid and distribution system. The Title XIII of this law has identified a list of actions to characterize a "Smart Grid." One of the action items includes a "deployment of 'smart' technologies ... for metering, communications concerning grid operations and status, and distribution automation." Another action item includes an "integration of 'smart' appliances and consumer devices." Additionally, the law also calls for a "development and incorporation of demand response, demand-side resources, and energy-efficiency resources" [1].

The Smart Grid would require "smart" metering devices and communication networks to collect and deliver necessary information about the power system for the operation of the power grid. Given a require communication networks, smart meters can provide the information about the power consumption for utilities and electricity consumers almost instantly. Many smart metering projects can be seen many places in the U.S. and other countries such as England. The real-time information is one of the tools for the dynamic pricing program, where the electricity price could change depending on the time-of-use for example [2, 3]. The accessibility of the power consumption in real time would allow the consumers to adjust the electricity utilization in order to minimize the electricity bill. In fact, the project report on the smart meter in England has shown that some consumers become more energy efficient users and lower their electrical bills [4].

These smart metering projects have shown that the electrical distribution net-

work can provide not only the power distribution but also an information provider for power planning and adjustment in real-time. The power consumption is not the only information that a "smart" meter can extract from the electrical voltage and current signals. Many diagnostic parameters of loads can also be measured and learned from the electrical signals as well. Diagnostic parameters such as the rotor speed of the induction motor and high frequency variation of the power consumption can provide additional information about the health of these loads. These diagnostic parameters require complex sensing hardware and information extracting algorithms to obtain key parameters from the electrical measurements. The need to collect detail information about individual load has led to the development of a nonintrusive load monitoring (NILM) system.

## 1.1 Nonintrusive load Monitoring

The development of high bandwidth networks has made an old dilemma increasingly more apparent: although networking makes it easy and inexpensive to obtain information from remote sensors, useful information can only be gathered by a potentially expensive and intrusive sensor array. Although mass production may ultimately reduce sensor cost, especially for solid-state or technologically advanced microelectromechanical sensors, installation and analysis will likely remain expensive. The overall reliability of a monitoring system with many sensors may be reduced in comparison to a system with relatively fewer sensors. The utility of data collected with a monitoring system is critically dependent on the ability to perform relevant and fast analysis of the collected data. More sensors may provide more potentially useful information, but at increased cost and increased burden in collating and correlating relevant observations.

On combat vessels, modern propulsion plant monitoring systems, for example, rely on hundreds of sensors installed throughout the main machinery space. Although

these sensor networks enable increased levels of automation, they are costly to install and to maintain. As these networks grow to include more sensors, there is a corresponding drop in the in the overall reliability of the monitoring system.

Fortunately, the growing reliance on electrically actuated systems provides a new opportunity to reduce sensor count. The basis for this clam lies in the fact that electrical currents contain significant information about the physical condition of individual loads. A device that monitors aggregate current at a central location can then disaggregate and track the behavior of multiple downstream components.

A nonintrusive load monitor (NILM) is a system that can determine the operating schedule of electrical loads at a target site using centralized measurements [5,6]. In contrast to other systems, the NILM reduces sensor cost by using relatively few senors. The NILM disaggregates and reports the operation of individual electrical loads like lights and motors using only measurements of voltage and aggregate current at the service entry to an electrical panel.

Over the last decade, the NILM system has been developed and improved as a nearly sensor-less platform for monitoring mission critical electromechanical loads on warships and office buildings [5, 7 19]. Field experiments have been conducted on board two US Cost Guard Famous Class Cutters, the *USCGC Escanaba* and *USCGC Seneca*. The Coast Guard Cutter *USCGC Escanaba* is shown in Figure 1.1. Additional load monitoring research opportunities have been explored for US Navy ships, including the DDG-51 class destroyer, through experiments conducted at the Navy's land-based engineering site (LBES). Until recently, most of these experiments have focused on particular engineering subsystems [20, 21].

In the recent years, new hardware and software have been developed for the NILM. Experimental results have shown the ability of the improved load monitoring system to provide useful information while underway, augmenting the routine observations traditionally made by a maintenance crew. In some cases, the NILM system has provided new information for which no sensor has been previously installed. The

Figure 1.1: Coast Guard Cutter *USCGC Escanaba*

NILM has been installed to monitor small collections of electrical loads and also initiates studies that consider how many electrical loads a NILM can successfully monitor on a shipboard power system. The goal was to develop a practical lower bound on the power changes that can be effectively detected by a NILM installed at the switchboard level.

Power system monitoring is an exciting approach for creating an inexpensive, highly capable "black-box" for monitoring the performance of critical shipboard systems. With remarkably little installation effort and expense, the NILM has been installed that can reliably monitor and track diagnostic conditions for multiple devices. The NILM can be used to determine the need for maintenance, to identify fault conditions, to find power quality problems, to help configure a power system after damage, and to provide reliable verification of load operation. Generally, the power distribution system can, with the proper signal processing and data analysis, be made to serve "dual-use." Specifically, it can simultaneously be used for its intended function of power delivery and as an information network for monitoring critical loads.

As previously noted, the NILM makes measurements of voltage and current solely at a single point in the electric utility service. The NILM characterizes individual loads by their unique signatures of power drawn from the utility. A transient detection algorithm can identify when each load turns on and off, even when several

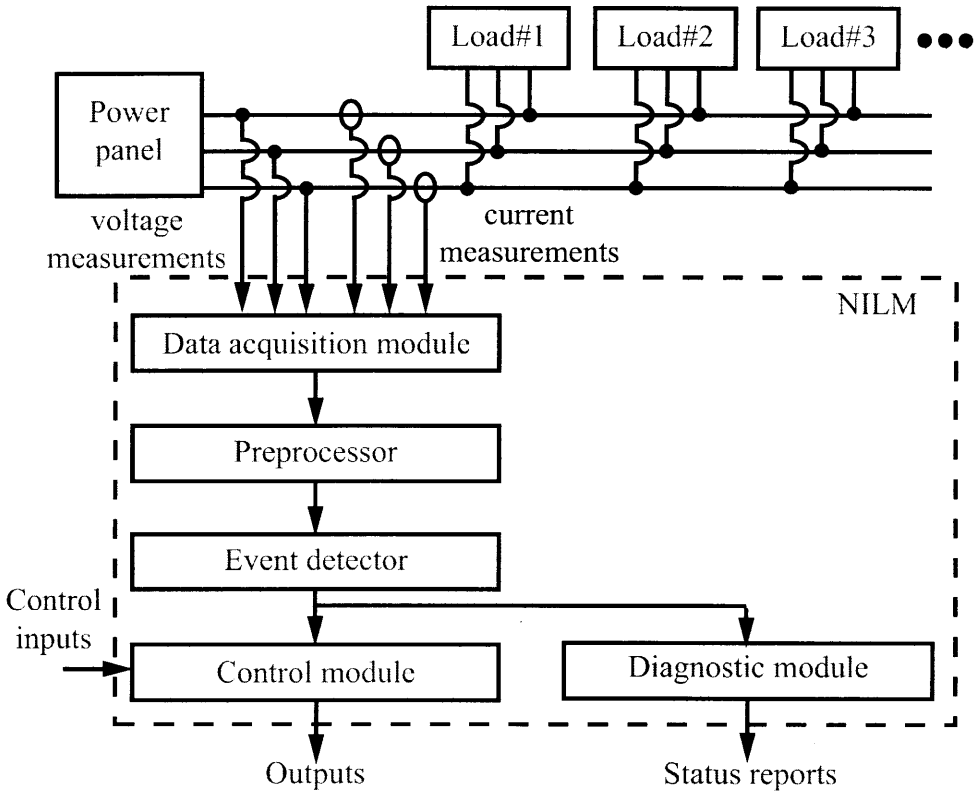


Figure 1.2: Simplified block diagram of a NILM system

loads do act nearly simultaneously. This monitoring can be performed with relatively little hardware: a computer, an analog-to-digital converter (ADC), and a single set of current and voltage sensors. A simplified block diagram of the NILM is shown in Figure 1.2. The NILM sensing hardware and the sensor installation are shown in Figures 1.3 and 1.4.

When installing a NILM to monitor multiple loads on a ship or other target system, the NILM undergoes a training phase. During training, the NILM observes individual electrical transient events that occur during the operation of particular loads. Examples of transient events that might be observed by a NILM are shown in Figures 1.5 and 1.6. Figure 1.5 shows the turn-on transient of an induction motor. Figure 1.6 shows the turn-on transient of an incandescent light bulb. Each electrical load performs a different physical task, and each load consumes power in a relatively

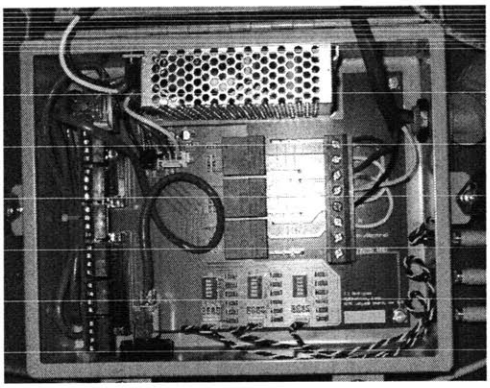

Figure 1.3: NILM sensing hardware

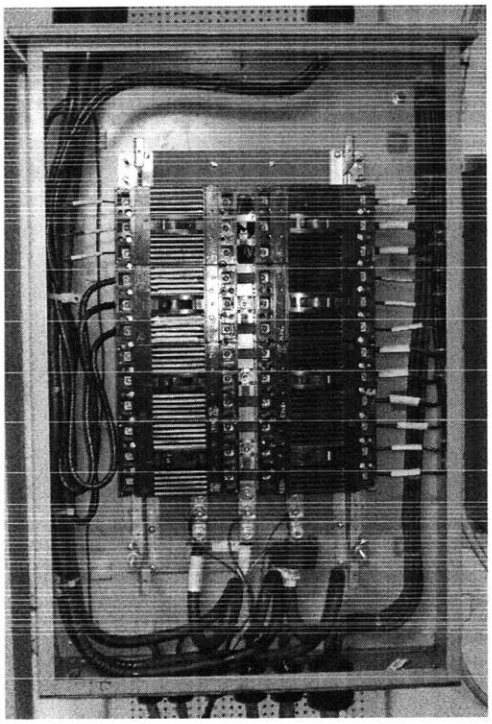

Figure 1.4: Current sensor installation

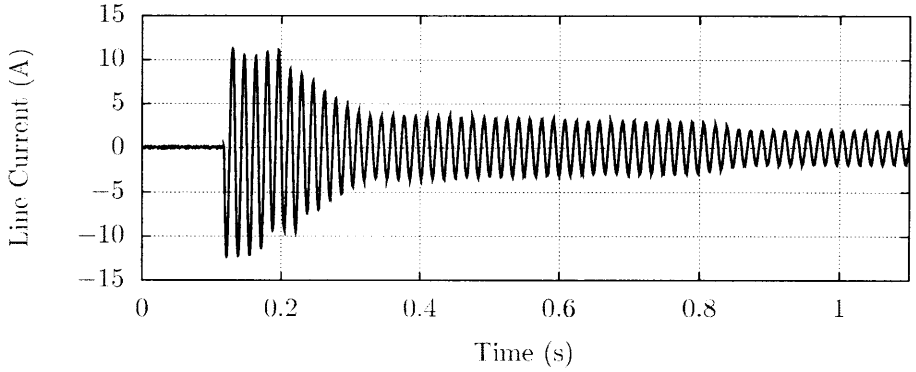


Figure 1.5: Turn-on transient of an induction motor

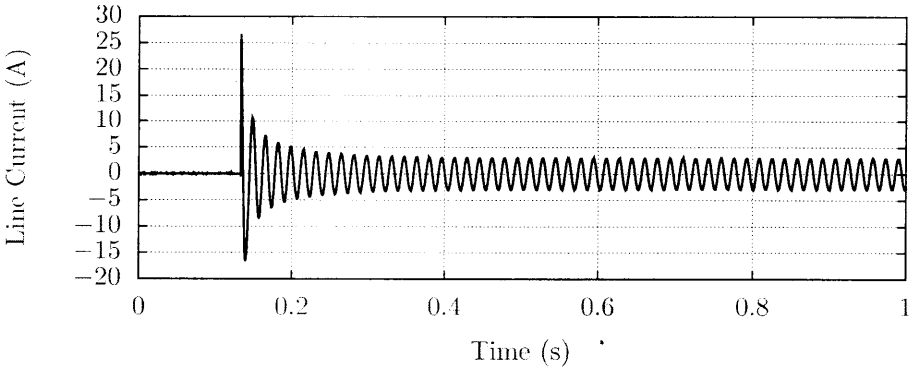


Figure 1.6: Turn-on transient of an incandescent lamp

unique way associated with its task. The three-phase induction motor shown in Figure 1.5, for example, shows a large pulse of current during the acceleration of the rotor, and then settles to a smaller steady state current. The incandescent light bulb shown in Figure 1.6 also draws a pulse of current at the turn-on transient, and settles down to a smaller but different steady state current demand. These transients serve as "fingerprints" that can be used to identify the operation of a particular type of load, even when several loads are operating at the same time.

In practice, the NILM examines and recognizes fingerprints by looking for known shapes in "spectral envelopes" or short-time estimates of the envelope of frequency content in the current waveform. Examples of the spectral envelopes of the three-phase induction motor are shown in Figure 1.7. An example of the spectral envelope of the incandescent light bulb is shown in 1.8. The NILM examines the spectral envelopes of the line frequency currents both in-phase and quadrature to the line voltage, as well as higher harmonics. The spectral envelope that is computed using the in-phase component of the fundamental frequency current can be referred as the real fundamental power or the real power. On the other hand, The spectral envelope that is computed using the quadrature component of the fundamental frequency current can be referred as the reactive fundamental power or the reactive power. The spectral envelope can be computed for higher harmonics such as the third harmonic as well, 180 Hz on a 60 Hz utility.

In the past, many researches have been conducted to explore the possibility of using a nonintrusive approach to diagnostic monitoring. The NILM has been installed at many sites, including the Coast Guard ships. Several key systems in the Coast Guard ships have been monitored, including auxiliary seawater (ASW) pumps, vacuum-assisted wast disposal system (collection-hold- transfer or CHT), and reverse osmosis (RO) water purification systems. The observations have been done both in-port and underway during operational cruising.

The unique signatures presented by different classes of loads create an op-

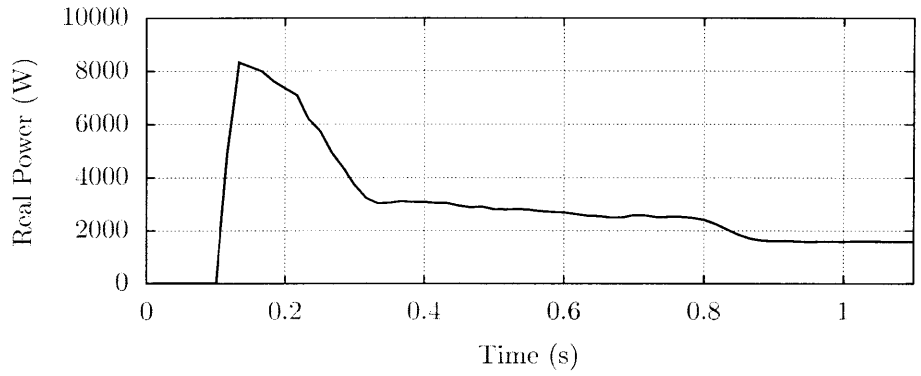


(a)

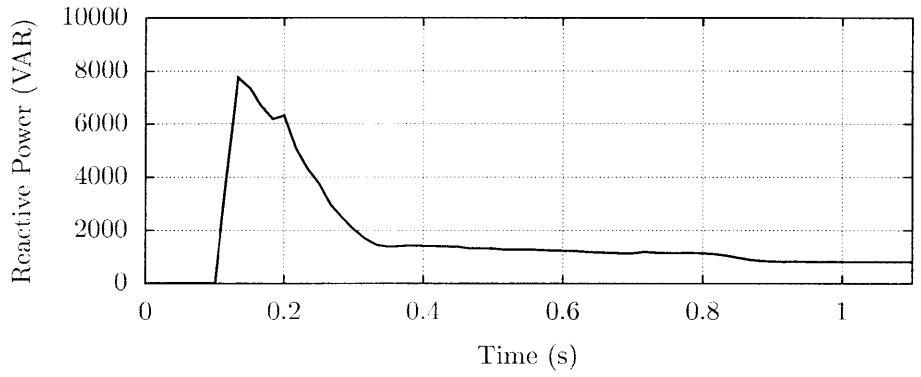


(b)

Figure 1.7: Power consumed by the three-phase induction motor. The real power consumed by the three-phase induction motor is shown in (a). The reactive power consumed by the three-phase induction motor is shown in (b).

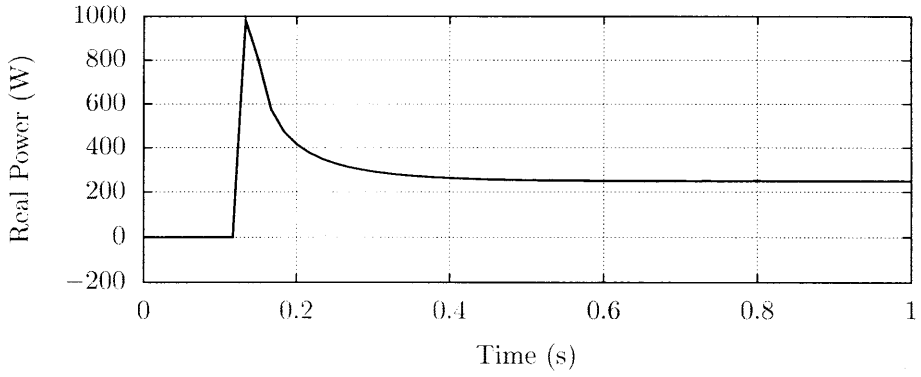


Figure 1.8: Real power consumed by the incandescent light bulb

portunity for diagnostic monitoring. Once it becomes possible to associate observed waveforms or segments with specific loads, it is possible to perform state and parameter estimation non the observed waveforms to track diagnostic parameters for individual loads. For example, the NILM has been used to determine several important operating parameters of the ASW system. The ASW system provides cooling for all heat loads on board the ship with the exception of those associated with the main diesel engine cooling. Heat loads are cooled by the ASW include the heating ventilation and air-conditioning (HVAC) units, refrigerators, freezers, diesel engine air coolers, and diesel engine lube oil coolers. The ASW system provides an excellent example of the diagnostic capabilities of the NILM. A coupling that connects the ASW pump motor to the pump head can fail leaving the ship temporarily without cooling, which is a major mission complication. Field data collected from the ship has shown that the high frequency "ripple" resents in the spectral envelopes during the transients increased as the coupling progressively failed [11, 22].

To further demonstrate the diagnostic capability of the NILM system, the non-intrusive monitoring system was installed at the entry service of the vacuum-assisted wast disposal system (collection-hold-transfer or CHT) in the *USCGC Escanaba*. The CHT system represents a common auxiliary system used to transfer sewage throughout the ship to a sanitary collection tank where it is pumped overboard. The operation of the CHT system has been described in [23, 24]. In these diagnostic experiments, the NILM monitored two vacuum pumps that are responsible for maintaining the pressure to operate the sewage collection system. The NILM diagnostic module has detected a possible failure in the system based on excessive cycling of the pumps [24]. An additional research has been done to automate the diagnostic monitoring and load tracking algorithms [15].

Examples in diagnostic monitoring applications shown above have demonstrated the benefit of the NILM system to provide crucial information maintaining effective mission critical system, verifying the health of subsystems, and preventing

any major failure by warning of any potential problem. The nonintrusive monitoring concept can be applied in to detect potential problems for a new load in the future as well.

## 1.2 Scalability

As the NILM has continued to track power consumption and diagnostic parameters of the loads, the NILM system is naturally expanded to cover more loads. Additional loads may be added to the power distribution increases the power consumed at the monitored site. Effectively, the range of measured current increases accordingly. This increased signal range directly affect the size of measuring sensors. More importantly, a larger range of measured signals could impact the ability of the NILM to track the power consumption of individual loads and extract key diagnostic parameters from the aggregate measurements. A different area of the nonintrusive load monitoring research is to find the limitation of the sensitivity of the NILM.

In the field, the NILM has been installed to monitor a subset of loads at the sub-panel of the power system. By monitoring the power panel close to the load, the NILM can collect information about a particular load without much interference from other loads, assuming the local sub-panel only services a few loads. A current transducer (CT) installed at the local sub-panel is usually chosen such that it can measure the entire range of current delivered by the sub-panel without saturation. If the sensor becomes saturated, the output signal will be distorted. As a result, many crucial diagnostic parameters such as transient spectral envelopes derived from the distorted input waveform could be incorrect. In addition, the diagnostic conclusion obtained from the output of the saturated sensor would be incorrect.

In the situation where the NILM is installed at a larger power panel that is located further from the load. In this case, the NILM is expected to monitor a group of loads that consume more power. Typically, the power panel for these loads is

located further from the load. Also, the breaker panel is usually rated for higher current value. As a result, a bigger CT is installed to account for a larger current range. A bigger CT prevents the measured current signal from saturating the sensor circuit. At the same time, a larger CT could reduce the measuring resolution of the signal.

As shown in Figure 1.2, the output of the CT is sampled by the analog-to-digital converter (ADC) in order to convert the measured current for the digital processing programs in the computer. Given the same electrical load consuming the same power, the larger CT of the same type will output a smaller signal. Therefore, the digitized signal will be small as well. One important issue arises as a consequence of the smaller input signal is a measurement error because of a lower signal-to-noise ratio (SNR). The error can come from a random noise source or a quantization error. The impact of the quantization error for the NILM system has been studied in [16]. The study has shown that NILM system can still detect and track certain classes of loads even though the sensing signal has been scaled down and heavily quantized by the ADC using an improved matching algorithm [16].

## 1.3 Challenges

For a given current sensor, the algorithm presented in [16] has improved the NILM in terms of load recognition for a larger group of load. However, the diagnostic monitoring applications that rely on a small amplitude signal embedded in a larger current signal such as a principal slot harmonic (PSH) would suffer from a small input signal. The PSH can be used to determine the speed of the induction machine, which can be useful to determine other physical parameters in the system [18, 33]. Specifically, a lower SNR signal has a higher noise floor that might corrupt the PSH signal causing an error in the speed estimation. When the interested signal is very small compared to the overall signal, it would be advantageous to have a sensing

module that can extract the detail information from the large signal with a good resolution and dynamic range.

In addition to the resolution and sensitivity issue of the sensor as the NILM is expanded to monitor more loads, the NILM is likely to include different classes of loads. In fact, many electrical loads do not have a fixed power consumption. The application of power electronics allows the load to operate continuously across a wide power range. This ability to dynamically adjust the operating point enables the appliances to perform the task more efficiently and optimally depending on the program settings. This behavior means that the load would not have a unique power consumption level nor a unique start-up transient anymore. As a result, the fixed pattern recognition algorithm would not work with the variable power loads. Variable power loads can been seen in many modern appliances such as variable speed drives, computers, dimmer, washing machines, dryers, heaters, etc. These loads are common in many industries and office buildings. The introduction of variable power loads causes the NILM to adjust the load disaggregation strategy to address the load disaggregation method.

The sensor resolution and the disaggregation of variable power loads have presented long standing problems for the nonintrusive load monitoring applications. This thesis explores the solution to these two issues and provides feasible solutions both problems. The sensor resolution is addressed by the modification of the current sensor design. On the other hand, the tracking of the variable power loads can be addressed by two different algorithms that can extract the power consumption of the variable power loads from the aggregate measurements.

## 1.4 Thesis Organization

This thesis addresses two long standing issues that the traditional NILM has encountered: the sensor sizing and the tracking of variable power loads. The proposed

solutions for this two problems are separated into the sensing hardware and the detection algorithm. In Chapter 2, the thesis describes an alternative way to measure the current waveform that decouples the dynamic range and the resolution in the design process. The ability to separate these two competing parameters allows the design of the sensor to be optimized for a specific application. The chapter explains the design process and trade-offs of design parameters. The sensor prototype has been built and demonstrated in the chapter as well. The proposed prototype has proved the concept of separating the dynamic range and bandwidth for the NILM application.

In Chapter 3, the thesis describes the circuit model-based estimator that can track the power consumption of the variable speed drive using higher harmonic currents uniquely associated with the VSD at the monitoring site. The proposed algorithm uses a simplified circuit model to study the behavior of the VSD system. From the circuit model, the system approximation is done to the generation of the current signal by thinking of the problem in term of the modulation between the internal current signal and the switching function. The switching function is derived from the behavior of the uncontrolled rectifier in the VSD system. Experimental results are included to demonstrate the ability of the proposed VSD power monitoring algorithm based on the simplified circuit model.

In Chapter 4, the estimator for the variable power loads have been revisited and modified. The second estimator is based on the observation of the current waveforms of the variable power loads. The structural features of the waveforms can be formulated into a set of linear constraints based on the Fourier analysis and synthesis equations. By applying a linear algebra method such as the Gaussian elimination, the estimator coefficients can be computed. The waveform-based estimator generalizes the process to derive the estimator for any load that consumes non-sinusoidal current waveform. The most useful benefit is that the algorithm does not need to know about the internal circuit construction of the load. Only the behavior of the current is required in order to compute the coefficients. In this case, the process is an

iterative method. Experimental results show the power tracking of VSDs, computers, and TRIAC-based light dimmer.

These three proposed solutions enable the NILM system to continue to use the patter recognition algorithm for the fixed power loads and use the proposed power estimator algorithms for the variable power loads. The proposed current sensor also allows the NILM to collect detailed information of the small load in the aggregate stream by using the physically-windowed sensor. The improved NILM can provide the necessary information for the demand side management program and other load diagnostic applications. The proposed solutions could potentially be integrated in the future "smart" metering device can provide information other than an overall power consumption of the consumer.

# *Chapter 2*

# *Physically-Windowed Sensor*

## 2.1 Introduction

In energy score-keeping and diagnostic applications, current sensors are often deployed to collect and analyze current waveforms from a collection of loads [5]. Analysis provides load disaggregation and detection, power consumption profiling, and diagnostics based on electrical signatures [5, 8, 10, 11, 13]. Many current sensors are available according to dynamic range and sensitivity. Hall sensors, flux-gate sensors, and Rogowski coils have all been used for non-contact current measurement [25–31]. As monitoring systems grow to include more loads and to provide more detailed information about the loads, the scalability and utility of the system depends on the quality of data acquired by the current sensor [16]. When monitoring large loads or collections of loads, some relevant features may be found in harmonics or aperiodic contents that are small compared to the current drawn at the fundamental line frequency. For other features, the full amplitude signal may be required. In order to collect both small details and overall picture of the signal of interests, the sensing unit should have a wide dynamic range to follow the overall behavior of the signal and good sensitivity to resolve fine features in the signal. These requirements could present opposing specifications for the sensor front-end.

For example, in an electrical system, an induction motor draws the current whose main component is at 60 Hz. On the other hand, a small signal such a principal slot harmonic (PSH) of the induction machine is embedded in the current signal at higher frequency [18]. In this situation, it is advantageous to have a single sensor that

can capture both the power and the PSH of the induction machine altogether.

To offer a flexible trade-off between bandwidth and dynamic range, a physically windowing sensor architecture is introduced. Large-scale variations are canceled so that the measured signal remains within a small operating window, which can be measured with a very accurate sensor. This architecture is similar to that of pipelined analog-to-digital converters [32], but utilizes a physical cancellation approach that can be applied to magnetic flux-based current sensors, strain gauges, pressure transducers, and many other physical systems. The cancellation is controlled by an embedded microcontroller, permitting a variety of windowing techniques and flexible processing and analysis. This thesis presents an initial application of this concept to power electronics and power system monitoring by developing a physically-windowed sensor for a current measurement that demonstrates high accuracy over a wide input range.

## 2.2 System Design

### 2.2.1 Current Measurement

In NILM applications, the NILM system extracts power consumption information and device parameters from the collected current measurements through digital signal processing (DSP) techniques. The underlying voltage and current measurements are converted into a digital format through an analog-to-digital converter (ADC) unit. The sensing system must provide a method to convert the current into a digital form that can be promptly used by the DSP unit. Practically, the ADC unit can be carefully chosen to have enough bits and bandwidth to satisfy the system requirements.

A simple way to measure the current is to pass the current through a shunt resister and measure the voltage across the resistor according to Ohm's law,

$$v_{\text{meas}} = i_{\text{actual}} R. \tag{2.1}$$

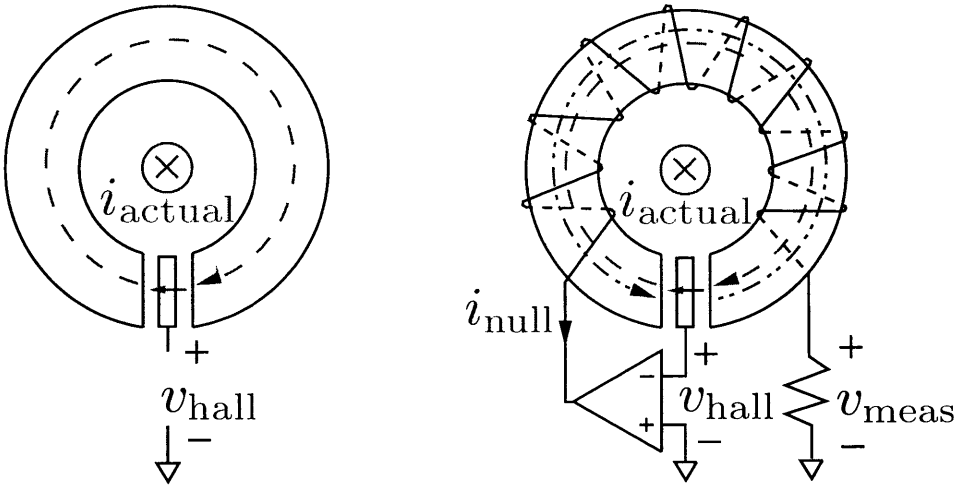


(a) Open-loop (b) Closed-loop

Figure 2.1: Examples of isolated current sensors

The voltage is proportional to the current assuming the resistor value remain unchanged. The measuring resistor that can stay stable for the required resolution is also available. A high value resistor provides a large output signal but also dissipates more power from the system. On the other hand, a small value resistor does not dissipate much power. However, the sensed voltage is small. The choice will be system dependent, and requires additional circuitry for galvanic isolation.

An isolated current measurement technique can employ a magnetically coupling system to infer the measured current by measuring the magnetic field strength $H$ along the closed path $C$ produced by the enclosed current $i_{\text{enclosed}}$ according to Ampère's law,

$$\oint_C Hdl = i_{\text{enclosed}}. \tag{2.2}$$

Examples of isolated current sensing systems are shown in Figure 2.1. The isolated sensing method provides a galvanic isolation between the input circuit and the sensing system. This sensing system usually consists of a flux concentration core and a flux measuring element. The flux measuring device such as a Hall element that give the

output voltage, $v_{\text{hall}}$, proportional to the magnetic flux density $B$,

$$v_{\text{hall}} \propto B = k_{\text{hall}} B. \tag{2.3}$$

In turn, the magnetic flux density $B$ is proportional to the the magnetic field strength $H$ in by a permeability $\mu$,

$$B = \mu H. \tag{2.4}$$

The sensing system can measure this voltage directly to infer about the input current. This system is an open-loop Hall sensor as shown in Figure 2.1a. The system performance depends largely on the Hall element in both resolution and range. A variety of Hall sensors and core structures can be used. Accuracy and precision will depend both on the Hall effect sensor and also the magnetic core, which may have significant nonlinearity.

The sensor performance can be enhanced by using a closed-loop Hall sensing system as shown in Figure 2.1b. In this case, the system uses the output voltage of the Hall element to drive a nulling current $i_{\text{null}}$ to keep the flux in the air-gap near zero. The nulling current $i_{\text{null}}$ is then measured through a ballast resistor. This nulling current $i_{\text{null}}$ is proportional to the actual current by a turns ratio. In this case, the use of the feedback with a high gain operational amplifier (OpAmp) can reduce the measurement error by the inverse proportion of the open-loop gain of the system. The small signal bandwidth of the sensor is also extended by the feedback loop. The closed-loop senor can provide a favorable bandwidth and accuracy trade-offs for a sensing system. The chosen sensing system must provide adequate dynamic range and resolution.

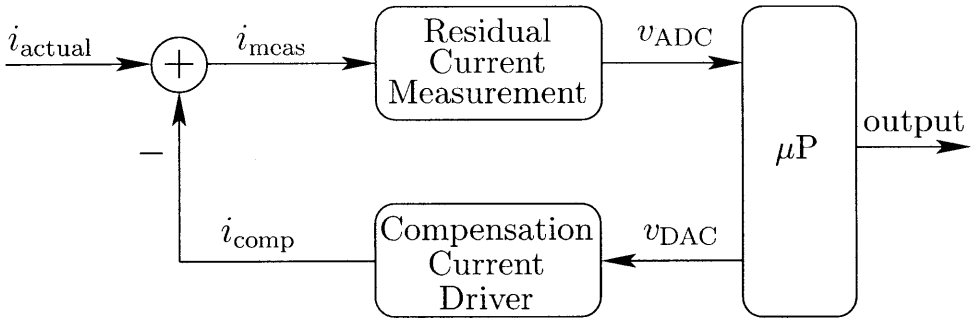


Figure 2.2: System block diagram of the physically-windowed sensor. The system consists of three primary components: the compensation current driver, the residual current measurement, and the microcontroller logic. The compensation current $i_{\text{comp}}$ is subtracted from the primary input current $i_{\text{actual}}$ by physical cancellation of magnetic flux.

### 2.2.2 System Architecture

In contrast to a traditional method that uses a single sensor and an analog-to-digital converter (ADC) combination to measure the signal, the proposed architecture aims to achieve both wide dynamic range and high resolution by dividing up the measuring range into smaller pieces. This smaller range can be measured with a reasonable resolution sensor, while the whole system keeps shifting a measuring window up and down according to the input current. This concept can be shown for the current measurement in Figure 2.2.

The windowed sensor architecture resolves the signal as a compensation offset and a measured detail signal. The system must reassemble the actual signal to faithfully represent the input measurement. Figure 2.3 depicts the signal reconstruction used to determine the total current using the windowed measurement.

Like the closed-loop Hall sensor, the proposed architecture uses physical input to apply a calibrated cancellation signal to the front-end sensor. In the windowed approach, two cancellation signals are used. The first cancellation signal has a coarse resolution and potentially lower bandwidth. The second cancellation signal has a relatively higher bandwidth. The initial implementation applies this approach to a

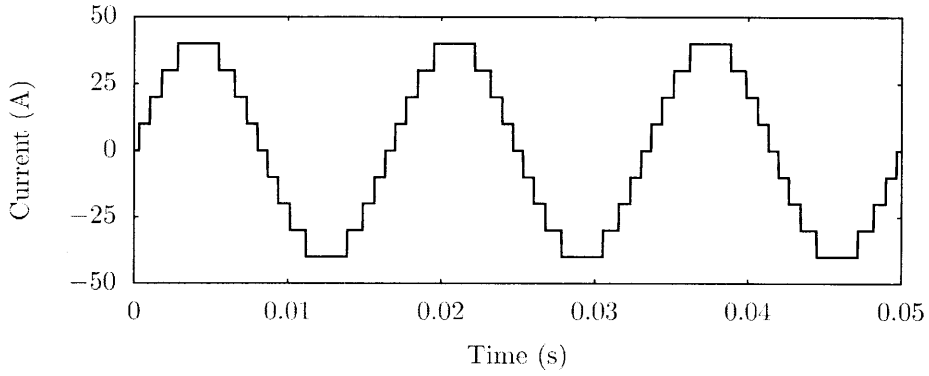


(a) Compensation

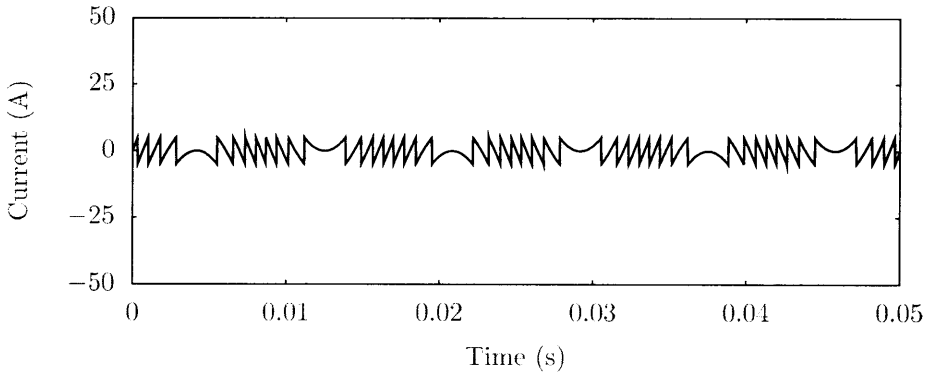


(b) Residual

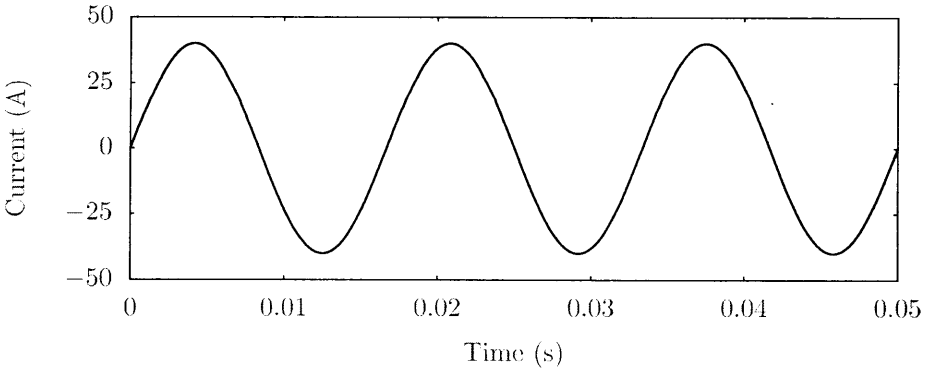


(c) Reconstructed

Figure 2.3: Example of a signal reconstruction. The compensation current and measured residual current are combined to determine the total current through the full sensor.

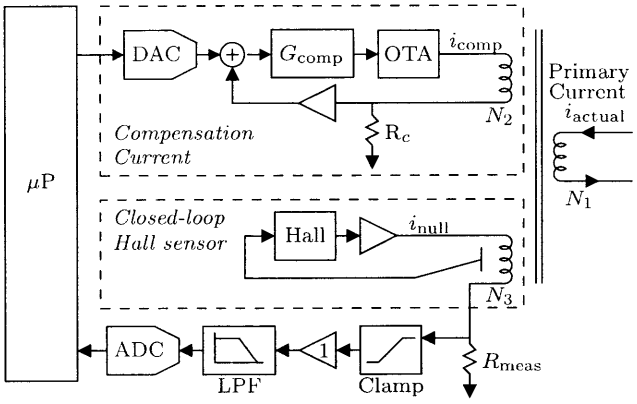


Figure 2.4: Detailed block diagram of the prototype system.

current sensor and follows the overall design shown in Figure 2.2. The residual current measurement is a customized closed-loop Hall sensor. A compensation current driver consists of an auxiliary winding and a current driver. The compensation current $i_{\text{comp}}$ is driven anti-parallel to large input currents such that the effective total current $i_{\text{meas}}$ seen by the sensing element remains within its designated operating range. The microcontroller coordinates and controls the system, performing calibration at startup and adjusting the compensation as necessary to keep the sensor at the desired operating point [34]. The detailed block diagram of the whole system is shown in Figure 2.4.

### 2.2.3 Signal Reconstruction

The total input current $i_{\text{actual}}$ is calculated from the instantaneous compensation current and sensor measurement as

$$i_{\text{actual}} = k_c \cdot i_{\text{comp}} + k_m \cdot i_{\text{meas}}, \tag{2.5}$$

where the variables $k_c$ and $k_m$ are calibration values determined by physical factors such as the number of turns on the sensing core and the amount of magnetic coupling between coils. The compensation current $i_{\text{comp}}$ is generated by an operational

transconductance amplifier (OTA), explained in Section 2.4.4. This current $i_{\text{comp}}$ is set by the microcontroller using a digital-to-analog converter (DAC) to generate a command voltage, $v_{\text{DAC}}$. The total compensation current is given by

$$i_{\text{comp}} = k_{\text{DAC}} \cdot v_{\text{DAC}}, \tag{2.6}$$

where the variable $k_{\text{DAC}}$ is determined by the OTA design.

Residual current is measured using a closed-loop Hall sensor, detailed in Section 2.4.1. This current $i_{\text{meas}}$ is read from an analog-to-digital converter (ADC) as the voltage $v_{\text{ADC}}$, and is given by

$$i_{\text{meas}} = k_{\text{ADC}} \cdot v_{\text{ADC}}, \tag{2.7}$$

where the variable $k_{\text{ADC}}$ is determined by the sensor front-end design.
Combining these equations, the complete reconstruction is

$$i_{\text{actual}} = k_c \cdot k_{\text{DAC}} \cdot v_{\text{DAC}} + k_m \cdot k_{\text{ADC}} \cdot v_{\text{ADC}}.$$

The constants can be simplified as:

$$i_{\text{actual}} = k_s(v_{\text{DAC}} + k_r \cdot v_{\text{ADC}}), \tag{2.8}$$

where the variable $k_r$ represents the ratio between the DAC command voltage and the corresponding change in ADC input voltage, and the variable $k_s$ represents a scaling to convert to actual current. This simplified form is used both for discussion and by the internal calibration and windowing procedures described in Section 2.4.5.

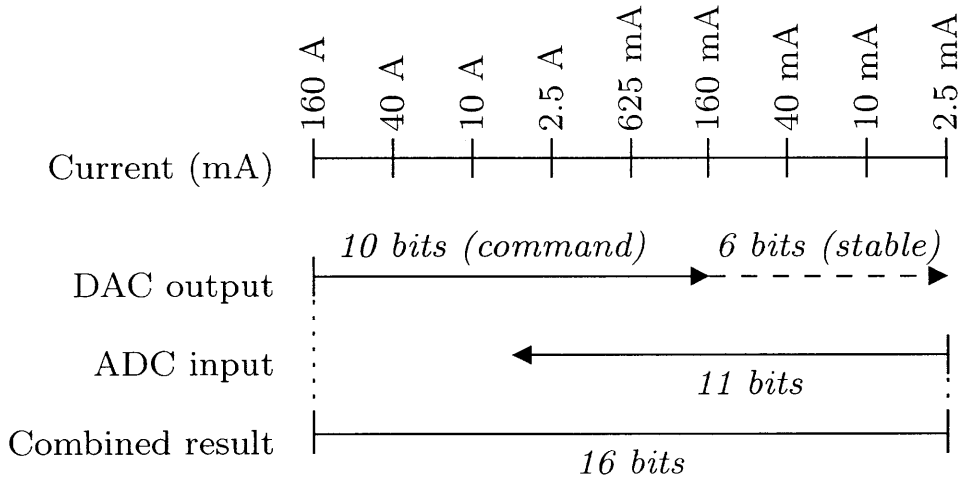


Figure 2.5: Overlap of the DAC output, relating to compensation current, and the ADC input, relating to the residual measurement. The ranges and overlapped positions are related to the parameters in (2.8). The combined result shows high accuracy over the full range.

### 2.2.4 Resolution and Range

The performance of the overall physically-windowed sensor system is determined by the parameters of its components. The ranges and resolutions of the compensation current and the residual measurement overlap, as depicted in Figure 2.5. In this example, the ADC is accurate to 11 bits over a range of 5 A, while the DAC command is accurate to 10 bits over a range of 160 A. The amount of overlap directly relates to the parameters $k_r$ and $k_s$ in (2.8).

A key requirement for physically-windowed sensing is that the compensation output must remain stable and predictable over the full desired system resolution. In Figure 2.5, this requirement is depicted as a dashed line on the DAC output. Here, for the lowest-order bits of the combined result to be accurate, each of the $2^{10}$ possible DAC commands must result in a voltage stability of one part in $2^{16}$. Certainly, a 16-bit DAC would suffice. However, only stability is needed, not accuracy. If a lower-resolution DAC is, or can be made to be, similarly stable in output, it is sufficient for

the sensor architecture. Using such a DAC may provide cost or performance benefits.[1]

Given that the stability requirement is met, then the actual output voltage $v_{\text{DAC}}$ can be related to the DAC command $x$ as

$$v_{\text{DAC}}(x) \propto \frac{x}{2^{10}} + \frac{\text{LOOKUP}[x]}{2^{16}} \tag{2.9}$$

where LOOKUP$[x]$ is a $2^{10}$-entry table that stores these 6 extra stable bits. This table can be populated by the micro-controller in a calibration step that uses the ADC input to determine the low-order bits of each DAC output.

### 2.2.5 Windowing

The front-end current measurement is "windowed" by the compensation current in the sense that the compensation sets a particular current window as an operating point, and the Hall sensor and ADC measure a small range of current in this window. The microcontroller has significant flexibility in the windowing approach, and the behavior can be adjusted based on expected bandwidth requirements and system parameters.

A basic approach to windowing is to continuously recenter the window so that the ADC measurement is zeroed; that is, the residual current is driven to zero after each sample. However, this requires that the OTA change its current output nearly continuously as the input signal changes, increasing the bandwidth requirements and potentially making the data less accurate if changes in compensation current are slow to settle. This extreme case fails to take advantage of signals that may be large amplitude low frequency content mixed with smaller amplitude high frequency contents. These types of signals are observed in the NILM environments and many

[1]The prototype implementation in Section 2.4 simulates this stability by using a 16-bit DAC with fixed random low-order bits on a 10-bit command. The low-order bits are set by the micro-controller and can be adjusted for testing purposes.

other applications.

The approach illustrated by the reconstruction in Figure 2.3 is to change the DAC command when the residual current in the sensor approaches the limits of the ADC front-end. The compensation current will remain constant for small input signal changes, and only change for larger input signals that exceed the window range. For many input signals, this may allow the compensation to change relatively slowly, reducing bandwidth requirements for the compensation driver.

Other approaches are possible, particularly for loads with known characteristics. A predictive estimator in the micro-controller can perform an anticipatory change in the compensation current so that the residual sensor current would be expected to fall within the sensor limits at the next sample interval. Such techniques can potentially increase the slew rate capability of the system.

### 2.2.6 Bandwidth

The bandwidth of the physically windowed sensor system depends on the input signal and its relation to the sensor window. There are two fundamental regions of operation: the first, within the windowed range of the residual current measurement, and the second, over the full range of the compensation current. For input currents that fall entirely within the window, the bandwidth performance of the system is equal to that of the residual current sensor front-end, as the compensation current is held constant. For full-scale input signals, the bandwidth is instead limited by how fast the compensation current can track the input change.

Maximum slew rate may be further affected by the windowing algorithm in use. Once the residual current exceeds the range of the sensor window, the compensation command must be adjusted. In the absence of prediction, the micro-controller will not know the extent to which the residual current exceeds the window range, and will be limited to stepping the compensation by one "window" worth of current at a time.

This, combined with the sampling rate of the residual sensor and the bandwidth of the compensation driver, will set the maximum $\frac{di}{dt}$ that can be accurately tracked. For slew rates outside this limit, the subsequent front-end sample will still exceed the window, and the micro-controller can report the potential inaccuracy as part of the output data stream.

The bandwidth and slew rate limits are a function of the resolution, range, and bandwidth of the system components. Flexible trade-offs can be made, for example, by adjusting the system to increase $k_r$ in (2.8). This would have the effect of increasing the relative size of the sensor window, increasing the region in which the recorded signal retains full bandwidth, and increasing the maximum slew rate. Conversely, decreasing $k_r$ increases the overall resolution of the reconstructed signal.

## 2.3 Benefits and Motivation

In many physical systems, large-scale changes occur at relatively slow speed while small-scale details can change rapidly. For example, an electric motor draws a 60 Hz fundamental current from the utility, but it may be desirable to observe a principal slot harmonic (PSH) at several hundreds or thousands of Hertz to track the motor speed [33]. These small, high-frequency details are superimposed on top of the 60 Hz current and need to be examined without saturating the sensor front-end. Conventional current sensors like the closed-loop Hall-effect sensor utilize a single compensation circuit to measure current. The physically-windowed sensing system, instead, divides the measurement into two subsystems, the compensation current driver and the residual current measurement. By dividing the problem and taking advantage of the fundamental differences between the requirements of the large-scale and small-scale measurements, the windowed system can utilize power and bandwidth trade-offs in the design of design each subsystem. This section describes these trade-offs and their design considerations.

### 2.3.1 Resolution

To obtain an accurate measurement, the system needs a reference that is stable to the required resolution specification. A conventional current sensor can utilize a single high-resolution ADC to perform the measurement, or it can use a single high-resolution DAC as a reference against which to compare a measurement. In both cases, it is required that the ADC or DAC be both stable and accurate to the full resolution.

With the physically-windowed approach, it is sufficient that the DAC be stable, but not necessarily accurate. A DAC with fewer controllable bits, but stable to the full resolution, can still be used. Initial experiments, testing the output voltage of a 16-bit AD7846 DAC with a HP34401A multimeter, demonstrated an accuracy of approximately 26 $\mu$V on a $\pm$5 V range, or approximately 18.5 bits, in a controlled environment. This example shows that, under some conditions, the output of the DAC is more stable than the controllable input.

The physically-windowed sensor design can then use a moderately accurate DAC and a moderately accurate ADC to create a compound data acquisition system that can accurately resolve more than the number of bits provided by either the DAC or ADC alone. For example, assuming proper calibration is performed, the system may be able to use one 10-bit DAC and one 10-bit ADC to create an effective 12-bit data acquisition system.

### 2.3.2 Bandwidth

A key consideration in the design process for analog circuits is the trade-off between power consumption and bandwidth. In this application, the measurement accuracy takes priority over the power consumption. The design can be tailored towards higher bandwidth at the price of high power consumption. If the signal of interest is comprised of both low-frequency and high-frequency contents that are reasonably far

apart, the current sensor may be able to take advantage of this separation by utilizing two separate compensation circuits, each optimized for one frequency region. In the physically-windowed sensor, the system measurement relies upon two subsystems: the residual current sensor and the compensation current driver. The residual current sensor is responsible for a high frequency and small magnitude signal; while the compensation current keeps track of the slow moving envelope of the signal.

The basic topology of a typical current sensor based on zero-flux sensing consists of three parts: a magnetic flux sensor, a compensation circuit, and a compensation winding as shown in Figure 2.1b. The input current creates a magnetic flux which is focused in the air gap of the gapped magnetic core. The magnetic flux sensor senses any magnetic flux in the air gap, and provides an output signal for the compensation circuit. This circuit drives a cancellation current to cancel the magnetic flux. Effectively, the system forces the magnetic flux in the air gap to zero, keeping the magnetic core around the zero-flux operating point and away from the saturation region. In order to measure a fast dynamic signal accurately, the measuring system should have a large bandwidth. In a closed-loop Hall sensor design, the system achieves the bandwidth using a compensation circuit and a feedback loop to ensure a high accuracy and wide bandwidth. A typical compensation circuit is an integration with a lead compensation network to drive the nulling current around the core. The detailed implementation of the modified closed-loop Hall sensor is shown in the next section.

The compensation circuit must cancel the flux by driving an equivalent current through the magnetic core, typically using an output stage consisting of an operational amplifier and push-pull current driver circuit. If the compensation current coil consists of $N_2$ turns, the primary winding consists of $N_1$ turns, and the maximum input current is $i_{\text{actual\_max}}$, then the compensation circuit must be able to drive $\frac{N_1}{N_2} i_{\text{actual\_max}}$ through the coil. Because the compensation current is only responsible for the slow variation of the signal, the bandwidth of this circuit can be lower.

However, the ability to track the large signal is dictated by the slew rate of the compensation current driver. As $N_2$ is increased, the drive current is lowered, but this also affects the inductance that the compensation circuit has to drive. Specifically, the inductance of the compensation coil is proportional to ${N_2}^2$. Large inductance will limit the maximum slew rate that the buffer circuit can provide for compensation. The slew rate $\frac{di}{dt}$ of the current in an inductor is given by

$$\frac{di}{dt} = \frac{v_L}{L} \propto \frac{v_{supply}}{{N_2}^2}, \tag{2.10}$$

where $v_L$ represents the voltage across the inductor, which is limited by the supply voltage of the system. For a smaller residual measuring range, the number of winding turns $N_2$ can be reduced, effectively lowering the inductance of the coil. The lower inductance allows this compensation circuit to follow the higher $\frac{di}{dt}$ rate according to (2.10), given the same supply voltage. Because the power is not the limitation, the choice of supply voltage can be designed to fit a specific application. The implementation of the compensation current driver is shown in the next section.

By separating the compensation current into two subsystems, the design process can be divided into two problems which may be tailored to take advantage of the input signal characteristics. In this case, two compensation circuits add complexity to the system, but provide more flexible power and bandwidth trade-offs.

## 2.4 Prototype Implementation

The prototype system was implemented according to the design introduced in Section 2.2. The system block diagram is shown in Figure 2.6. The physical coupling of the subsystems occurs on a single toroidal core. The primary current to be measured passes through $N_1$ turns on the core. The cancellation current passes through $N_2$ turns, wound in the opposite direction. The residual current is measured by a closed-

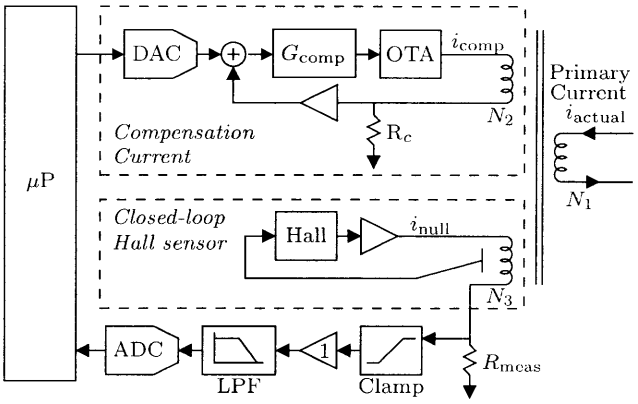


Figure 2.6: Detailed block diagram of the prototype system.

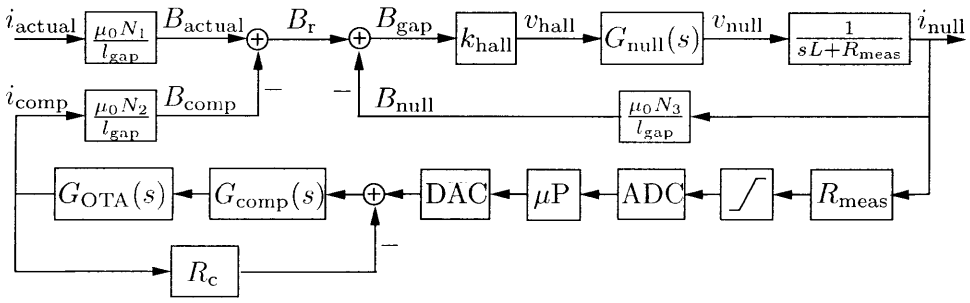


Figure 2.7: Full system block diagram

loop Hall sensor that utilizes $N_3$ additional turns. The $N_2$ and $N_3$ loops are co-wound to minimize the leakage inductance. Typical values for our testing are $N_1 = 50$ and $N_2 = N_3 = 200$. The overall block diagram of the whole system is shown in Figure 2.7. The block diagram shows a nested closed-loop systems. The inner loop is for the residual current measurement, while the other loop is for the compensation current controlled by the microcontroller. The compensation current itself is also an independent closed-loop system. The following sections describes the actual circuit design of each subsection in details.

### 2.4.1 Closed-Loop Hall Sensor

The residual current measurement is performed by the closed-loop Hall-effect sensor shown in Figure 2.8. The basic structure of this circuit consists of a nulling coil rep-

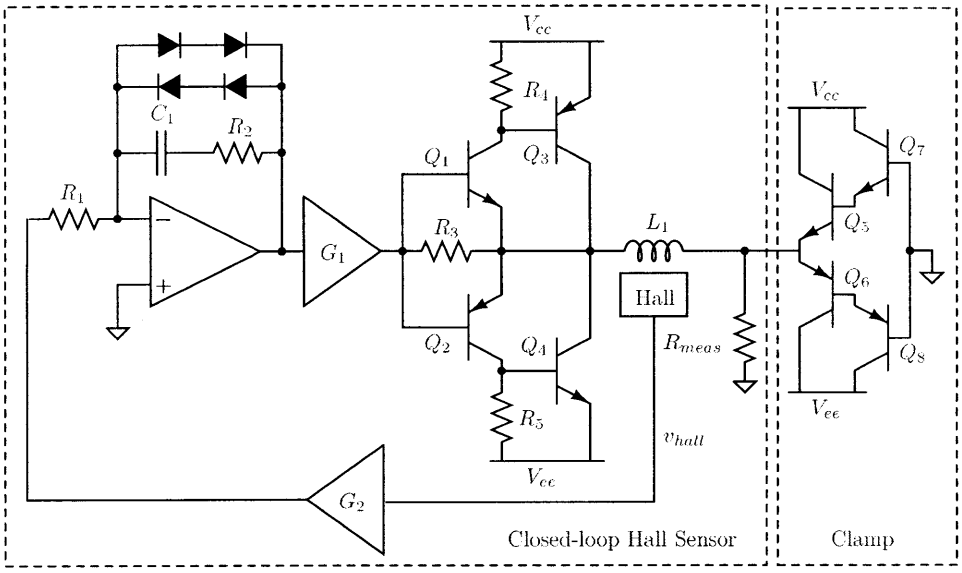


Figure 2.8: Circuit diagram of the customized closed-loop Hall sensor and the active clamp

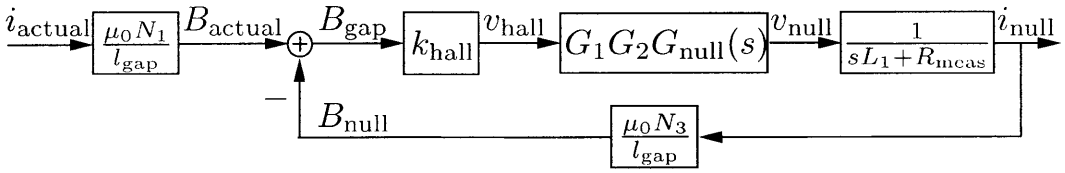


Figure 2.9: System block diagram of the closed-loop Hall sensor

resented by the inductor $L_1$. The Hall element drives the output $v_{\text{hall}}$ proportional to the air-gap magnetic flux, $B_{\text{air-gap}}$. The gain blocks $G_1$ and $G_2$ use a standard inverting amplifier gain circuit. The compensation circuit is comprised of an integrator with a lead compensation network showing by $R_1$, $R_2$ and $C_1$ for the nulling current. The modified push-pull driver is connected after the gain block $G_1$ to provide the nulling current, $i_{\text{null}}$. The resistor $R_3$ allows the gain block to drive the current without the cross-over distortion from transistors $Q_1$ and $Q_2$. Extra transistors $Q_3$ and $Q_4$ supply additional current when needed. The nulling current is then read by an 11-bit ADC to produce the residual measurement.

The block diagram of the closed-loop Hall sensor is shown in Figure 2.9. This

compensation network has a transfer function,

$$G_{\text{null}}(s) = \frac{sC_1R_2 + 1}{sC_1R_1}. \tag{2.11}$$

This compensation network gives the system with a high open-loop gain from the integrator. The zero at $z = -\frac{1}{C_1R_2}$ can be used to adjust the phase margin by placing near the inductor pole, $p = -\frac{R_{\text{meas}}}{L_1}$. The open-loop gain can be affected by the number of turns $N_3$ as well. As the turn number $N_3$ increases, the gain also increases. However, the inductance $L_1$ increases proportional to $N_3^2$, lowering the bandwidth of the front-end sensor. Furthermore,

### 2.4.2 Clamp Circuit

Additionally, the clamp circuit is also shown in Figure 2.8. In the event that the compensation current circuit could not cancel the main current fast enough, the front-end sensor will have to take care of the nulling the flux in the air gap. Once the nulling current gets larger, the voltage across the measurement resistor $R_{\text{meas}}$ becomes high enough to fully turn on the Darlington transistor pair $Q_5 - Q_7$ or $Q_6 - Q_8$. Effectively, the output voltage $v_{\text{meas}}$ is also clamped at about $2V_{be}$ above and below the ground reference. The voltage $V_{be}$ is the transistor threshold voltage, normally around 0.7 V. Furthermore, the clamp also protects the over-voltage condition of the ADC input stage as well. Once the compensation current catches up with the main current, the clamp is automatically deactivated and the front-end sensor acts normally again. This circuit protects both the Hall sensor and the ADC system from extreme conditions.

### 2.4.3 Residual Current Measurement

In our system, the Hall sensor is designed to measure over a small current range of approximately $\pm 2.5$ A. If the input signal starts to exceed this range, the compensa-

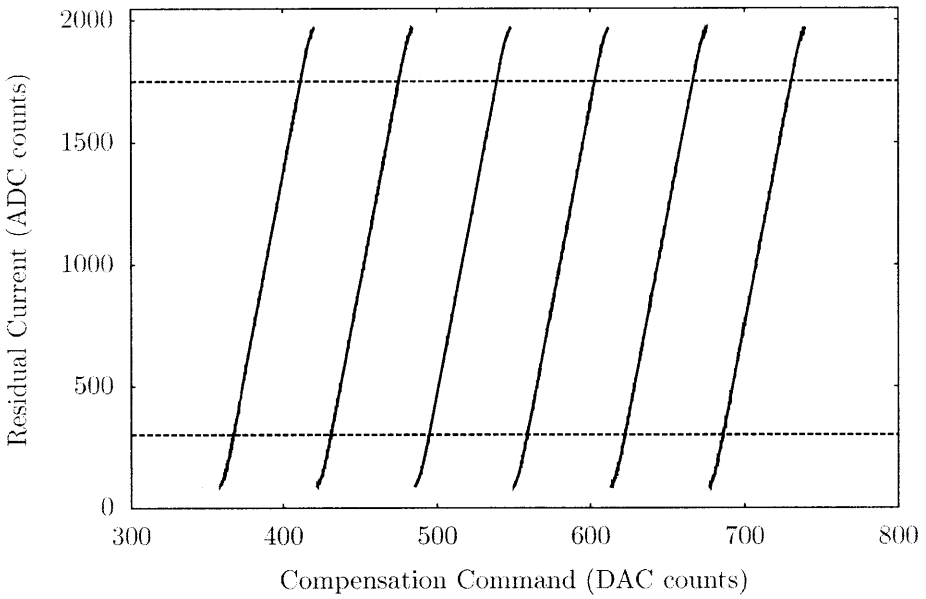


Figure 2.10: Calibration curves showing 11-bit residual current measurement versus 10-bit compensation current command, at various fixed primary currents. The curves are generally linear with slope $k_r$ and flatten out as the clamps begin to activate outside of the dashed lines.

tion current driver is separately commanded to cancel a portion of the flux in order to keep the residual sensor operating normally.

Figure 2.10 shows measured calibration curves between the compensation current output and residual sensor input, for various operating points set by the primary current. The slope of each line corresponds to the constant $k_r$ in (2.8). The dashed lines indicate the approximate measuring range of the ADC for the residual current. The digital controller attempts to maintain the window so that the residual current always falls within this range.

During a high current transient, the input current may temporarily exceed the ability of the system to compensate. To prevent the residual sensor from overloading in this condition, a clamp circuit is added at the output of the Hall sensor. This extra clamp current serves to cancel the primary current and limit maximum residual. The clamp current is not reflected in the ADC reading, causing the measured values to

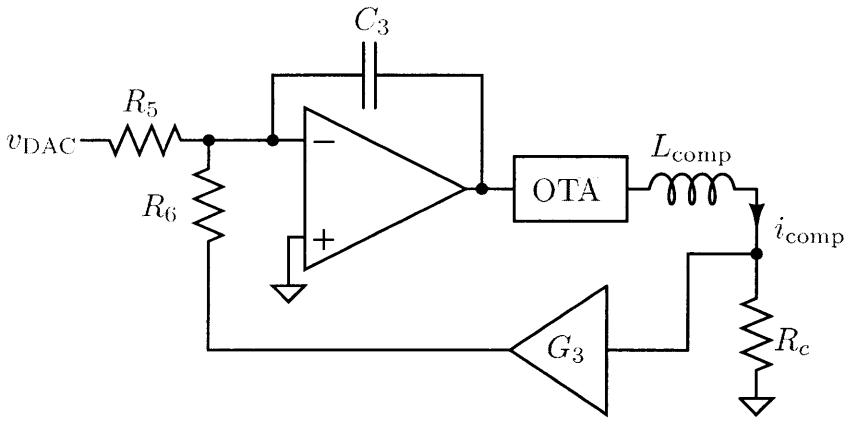


Figure 2.11: Compensation current driver circuit diagram

saturate, as shown shown in Figure 2.10. After the overload condition, the clamp deactivates and the Hall sensor returns to normal operation. The system utilizes a magnetic core with a low remnant flux to further minimize the offset error after experiencing such a transient.

### 2.4.4 Compensation Current

The compensation current driver uses a highly stable digital-to-analog converter (DAC) to establish a voltage command reference. A closed-loop circuit is designed to scale and convert the voltage command into the desired output current. The compensation current is driven through an auxiliary winding that is co-wound with the nulling coil to minimize the leakage inductance. The voltage command is controlled by the microcontroller. The compensation circuit block diagram is shown in Figure 2.11.

To minimize interaction between the two feedback loops, the output stage of the compensation circuit is high-impedance and appears as an open circuit to the residual sensor circuit. The OTA design is shown in Figure 2.12. In this implementation, the OTA includes a voltage buffer front-end to receive the voltage command from the compensation current feedback op-amp. The buffered command is used to

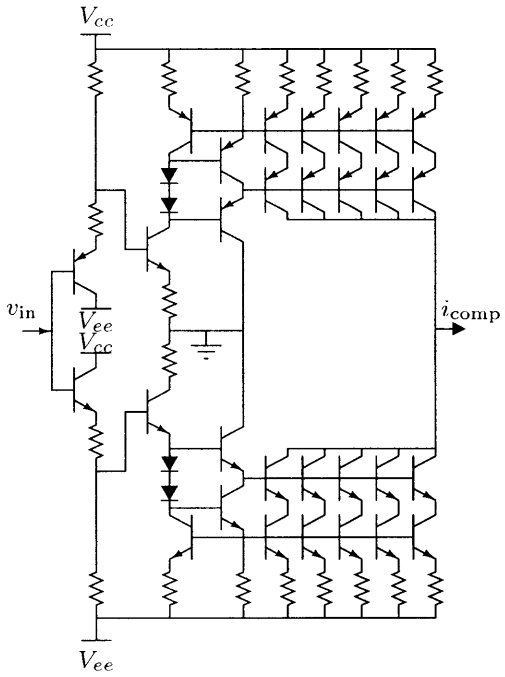


Figure 2.12: Output stage of the compensation current subsystem, showing the OTA implementation

establish a reference output current in the second stage. This reference current is replicated through a current mirror structure. The current mirror uses a cascode topology to improve the output impedance. The emitter degeneration resistors are added to scale the current and to prevent a thermal runaway condition. The OTA structure includes multiple output branches connected in parallel, in order to minimize the power dissipation per branch. Within each cascode branch, the transistor next to the rail sets up the mirrored current, and the cascode transistor acts as a current buffer. The power dissipation in each cascode branch is concentrated at the cascode transistors. Therefore, the thermal effects on the mirrored current are reduced. Finally, the $\beta$-helper transistors are included to provide additional base current for the output stage.

The OTA output passes through $N_2$ turns on the core and is measured with a sense resistor. The analog feedback loop in the compensation current subsystem

serves to minimize error within the output stage. The output current measurement can optionally be provided back to the microcontroller through a low-bandwidth 24-bit ADC for calibration purposes. The circuit board that includes the OTA and the microcontroller circuit is shown in Figure 2.13. All circuit schematics of the prototyped board are included in Appendix A.

### 2.4.5 Microcontroller

The prototype uses a Microchip dsPIC33FJ256GP710 microcontroller to implement the control logic. It controls the sampling of the residual current measurement, implements the windowing algorithm used to set the compensation current, and communicates all data to a computer for analysis. The microcontroller also performs calibration at startup and on request [34].

#### 2.4.5.1 Sampling

The ADC is sampled at 8 kHz, a rate chosen to match that used in existing non-intrusive load monitoring systems [16]. At each sample, the microcontroller calculates the total reconstructed current from the compensation command and the residual measurement, and transmits this data to the computer. If necessary, the compensation command is then changed to adjust measurement window.

The sampling interval has a direct influence on the slew rate capability of the system. If the residual current exceeds the window range, the measurement is clamped and the recombined output will be inaccurate. For a given operating point and windowing strategy, a maximum current excursion $i_w$ can be observed within the current window before saturation. Given the sampling interval $\Delta t$ and primary input slew rate $\frac{di}{dt}$, it is necessary that

$$\Delta t \cdot \frac{di}{dt} < i_w. \tag{2.12}$$

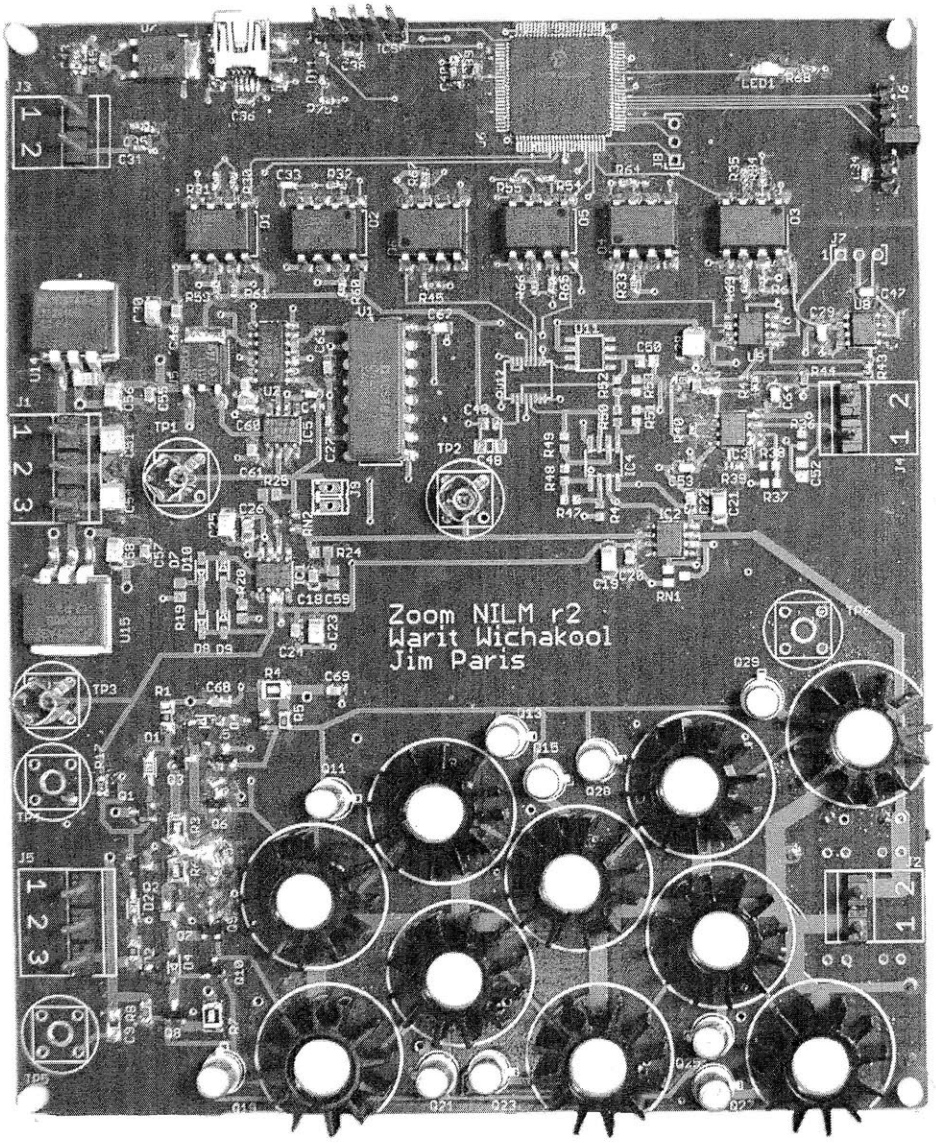


Figure 2.13: Prototype implementation

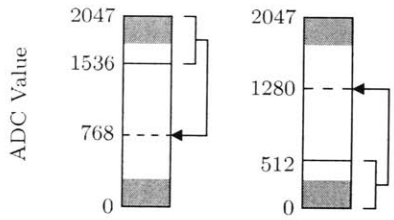


Figure 2.14: Windowing approach in the prototype implementation. For input ADC values greater than 1536, the compensation current is changed such that the target ADC value is 768. For input ADC values less than 512, the target ADC value is 1280. The clamps are active in the shaded regions.

Thus, decreasing $\Delta t$, by increasing the sampling rate, has a corresponding linear effect on the maximum slew rate $\frac{di}{dt}$.

In practice, the limit on $\Delta t$ is set by the response time of the hardware components and the processing speed of the microcontroller. Regardless of the sampling rate, the data reporting rate to the computer can be maintained at 8 kHz for compatibility.

#### 2.4.5.2 Windowing Strategy

Using (2.8), the microcontroller can determine by how much a given change in DAC command will affect the sensor measurement at the ADC input [34]. Assuming that the primary current $i_{\text{actual}}$ remains constant, a pair of DAC and ADC values are related by

$$k_s(v_{\text{DAC},1} + k_r \cdot v_{\text{ADC},1}) = k_s(v_{\text{DAC},2} + k_r \cdot v_{\text{ADC},2}) \tag{2.13}$$

$$v_{\text{DAC},1} - v_{\text{DAC},2} = k_r(v_{\text{ADC},1} - v_{\text{ADC},2}) \tag{2.14}$$

Thus, to cause a change of $\Delta$ADC at the residual measurement, the DAC command should be changed by $k_r\Delta$ADC. The prototype implementation uses this approach to "recenter" the window whenever the ADC value begins to approach the clamp limits. This is depicted in Figure 2.14. For example, when a sample $x$ from the

ADC exceeds a fixed upper limit of 1536, the compensation command is increased by $k_r(x - 768)$ so that the next sample is near 768.

The chosen target ADC values intentionally overshoot the center of the ADC range because it is expected that, in most cases, an increasing current will continue to increase. This provides some extra "headroom" for the common case, which in turn increases the maximum slew rate that the prototype can handle.

#### 2.4.5.3 Communication

All data, including raw DAC and ADC values and calibration constants, are continuously sent to a computer via a full-speed USB link. In some configurations, the microcontroller may read the ADC more frequently than the samples are sent to the computer, and so status flags that indicate error states are also included independently. For example, one flag denotes whether the ADC value was ever observed in the clamped region, which indicates that the returned data for that sample may not be accurate to full resolution.

#### 2.4.5.4 Calibration

In order to perform windowing accurately, the microcontroller needs to know the calibration constant $k_r$ (Section 2.2.3) and the table LOOKUP (Section 2.2.4). The value of $k_r$ can be determined using the relationship in (2.14), if the primary current is constant. In the prototype implementation, the microcontroller assumes constant current and performs calibration at startup, or when triggered by the connected computer. Using an initial estimate $k_r = 1$, the calibration algorithm adaptively adjusts the estimate as it changes $v_{\text{DAC}}$ to seek two specific $v_{\text{ADC}}$ values corresponding to ADC inputs 512 and 1536. Once these DAC commands are found, each $v_{\text{ADC}}$ is oversampled to reduce noise and a final accurate estimate of $k_r$ is computed.

Table LOOKUP is used to map each low-resolution DAC command to its cor-

responding high-resolution stable output voltage. In the current prototype, this extended stability is simulated using an accurate DAC, and so the lookup is hard-coded to match the randomized low-order bits written to the DAC. However, the system supports an additional low-bandwidth 24-bit ADC for measuring the output compensation current. This calibration ADC could be used to measure and fill the LOOKUP entries for each possible DAC output, in the absence of a hard-coded table.

Finally, to convert the final output of the physically-windowed current sensor to amperes, the scaling factor $k_s$ is used. It is not directly needed by the microcontroller logic, and is currently calibrated by the computer in post-processing using known test values from a Keithley 2400 Source-Meter.

## 2.5 Prototype Results

Various aspects of the prototype physically-windowed current sensor system have been tested. Test setups and test results are shown in the following sections.

### 2.5.1 Full system functionality

Basic functionality was tested by constructing a test load consisting of an incandescent light bulb and a personal computer, which together draw power at both the fundamental and third harmonics of the line frequency. Figure 2.15 shows the waveforms as measured by external test equipment. The input current is $i_{\text{actual}}$, the generated compensation current is $i_{\text{comp}}$, and the residual current is $i_{\text{meas}}$.

The reconstructed output of the sensor system for the same test load, based on data reported by the microcontroller, is shown in Figure 2.16. In some cases, the high slew rate associated with the third harmonic content in the load caused the residual current measurement to exceed its window and enter the region where the clamps are active. The recombined data at these samples is known to be potentially inaccurate

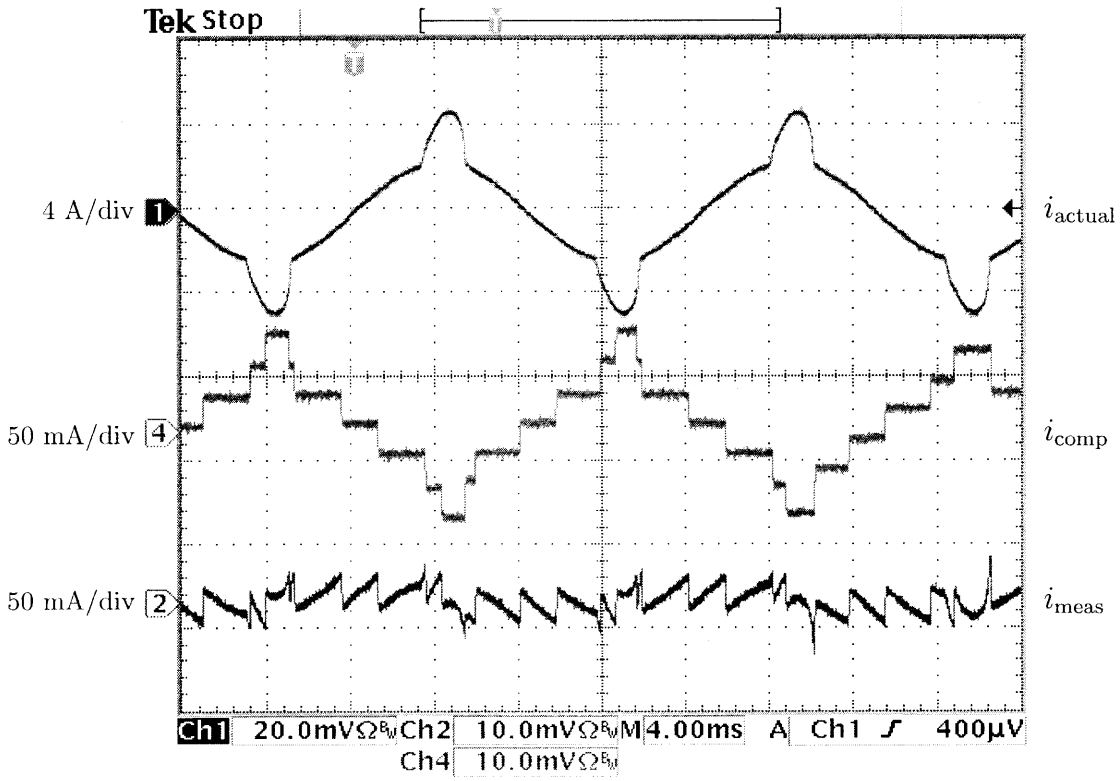


Figure 2.15: Oscilloscope traces showing the measured primary, compensation, and residual measurement currents while the prototype physically windowed current sensor is in a normal operation

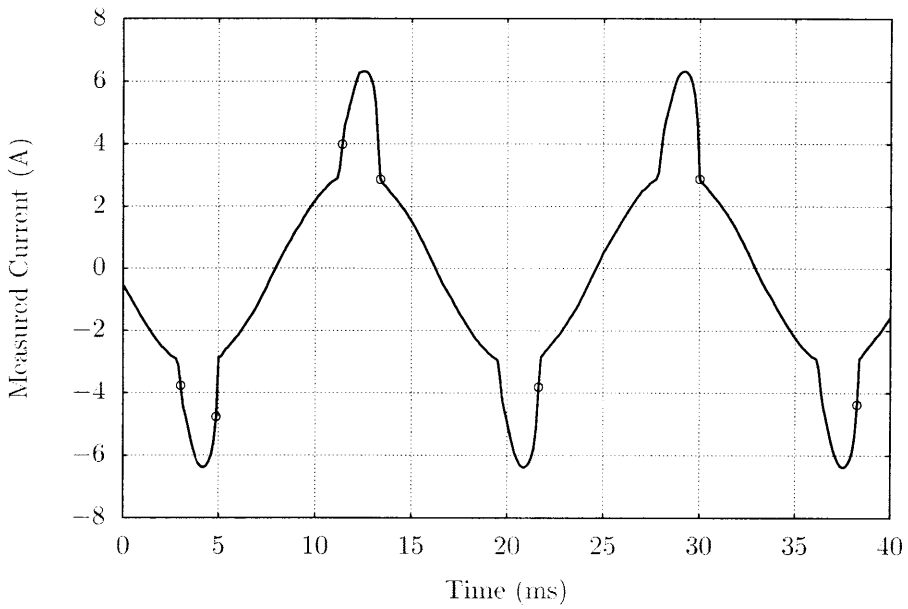


Figure 2.16: Reconstructed current from the sensor. Circled points indicate individual samples that are known to be potentially inaccurate because the residual current was in the clamped region of the sensor window.

because of this. In the figure, these specific samples are circled. Note that they do not occur uniformly on every line cycle, because such excursions from the window depend on the varying relationship between sample time, slew rate, and the current window position.

### 2.5.2 Static resolution tests

The maximum resolution of the sensor system was characterized by analyzing the static performance. For this test, a Keithley 2400 Sourcemeter was used to supply various dc currents. These currents were passed through the sensor $N_1 = 50$ times to create the primary current $i_{\text{actual}}$. Each effective current level was chosen at random from a $\pm 25$ A range. Once the test current stabilized, the reconstructed output from the prototype system was sampled at 8 kHz for approximately 110 ms. Approximately 500 unique test current levels were applied in total. A histogram of the resulting error

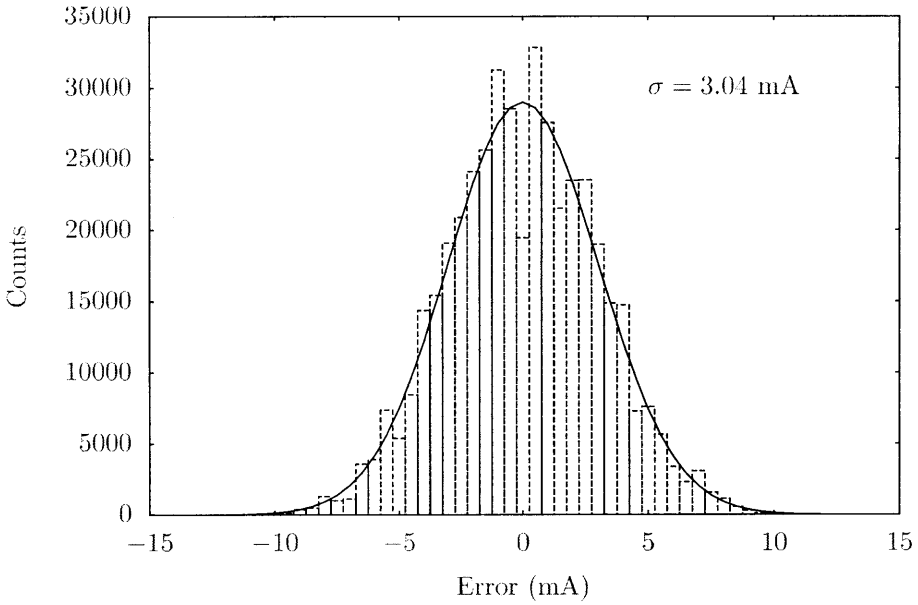


Figure 2.17: Histogram of the measured errors during a test of dc performance. 91% of the samples fall within ±5 mA, which gives an accuracy over the full ±80 A range of approximately one part in $2^{14}$.

between the Keithley reported output and the reconstructed sensor output is shown in Figure 2.17. Typical errors for each sample are less than ±5 mA. Over the full 160 A range of the compensation current driver, this 10 mA range translates into an effective resolution of

$$\log_2(160/0.01) = 13.996 \text{ bits} \tag{2.15}$$

In the prototype system, the DAC command for the current compensation is 10 bits, while the ADC input from the residual measurement is 11 bits. This result of nearly 14 bits demonstrates the concept of using physical windowing to extend the sensor resolution over a larger range.

### 2.5.3 Dynamic resolution tests

The ability to resolve small signals while tracking a large signal was evaluated by creating a test load consisting of an incandescent lamp bulb in parallel with the Keithley 2400 Sourcemeter. For this test, the change in the envelope of the measured lamp ac waveform was examined as various small test currents were injected through the sensor using the Keithley source. The injected current was cycled between 0 mA, 20 mA, and 10 mA. The resulting reconstructed waveform is shown in Figure 2.18. The small change in dc level can be seen in the detail shown in part (c). Like the static resolution test, this shows a resolution of approximately 10 mA.

### 2.5.4 Residual sensor transient response

In order to prevent drift in the output, the residual sensor employs a current clamp that prevents the toroidal core from saturating. The transient response of the residual sensor was tested by applying a large instantaneous current of 20 A through $N_1 = 5$ turns. This results in an effective primary current of 100 A, significantly greater than the typical operating window for the residual. This test simulates the case where a large input transient is seen before the compensation current is applied. The results are shown in Figure 2.19. During the transient, the clamp activates, providing necessary current to keep the core near the zero-flux operating point. When the transient disappears, due to either a change in input or a change of the compensation current, the clamp deactivates and the residual current measurement resumes normal behavior. The offset drift in the residual sensor output $v_{\text{mcas}}$ is less than 5 mV after the transient, demonstrating that hysteresis loss in the core was minimized.

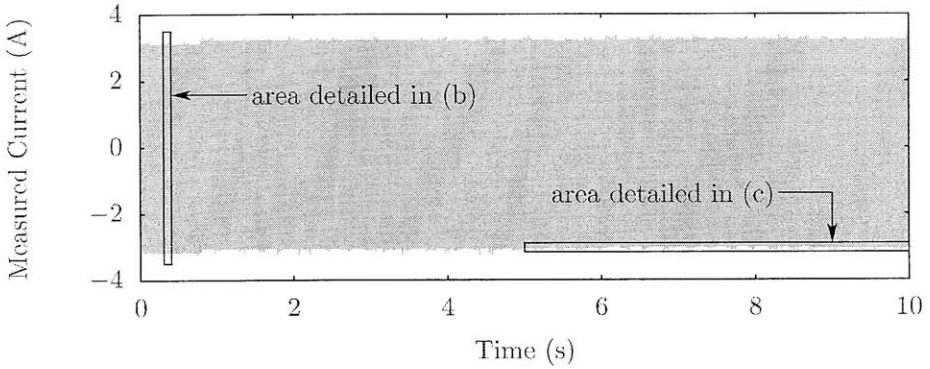


(a) Full reconstructed current

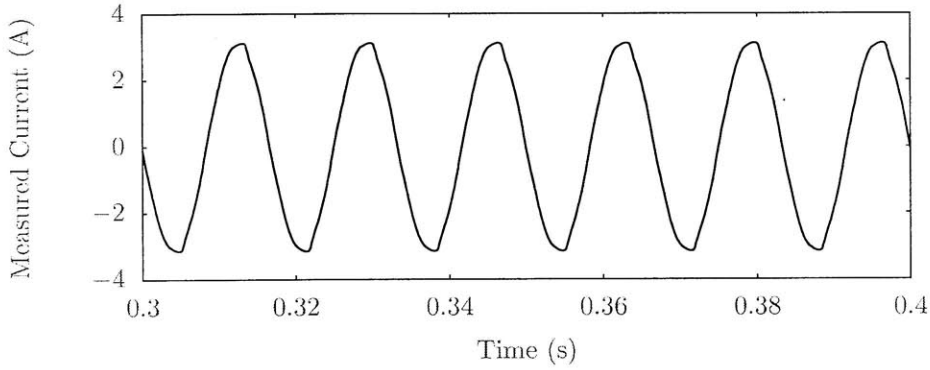


(b) Detail over several line cycles

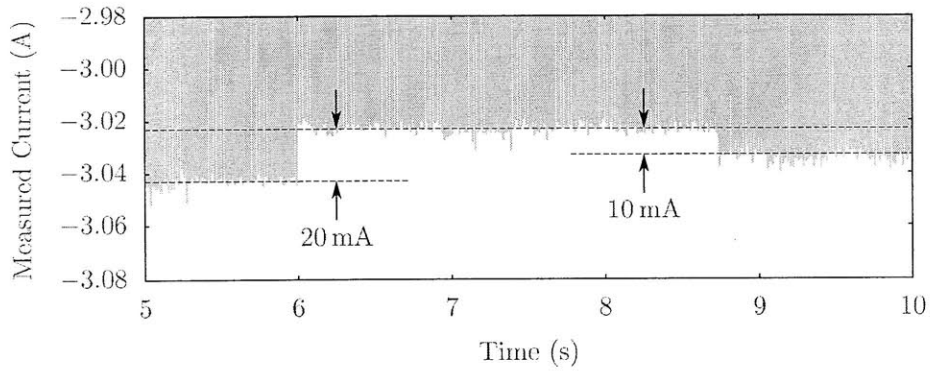


(c) Detail of a small dc change

Figure 2.18: Example of measuring a small dc current on top of a large ac current. The ac current is from a light bulb and the dc offset is added by a Keithley 2400 Sourcemeter, measured in parallel. Steps of 10 mA are resolvable in the reconstructed sensor output.

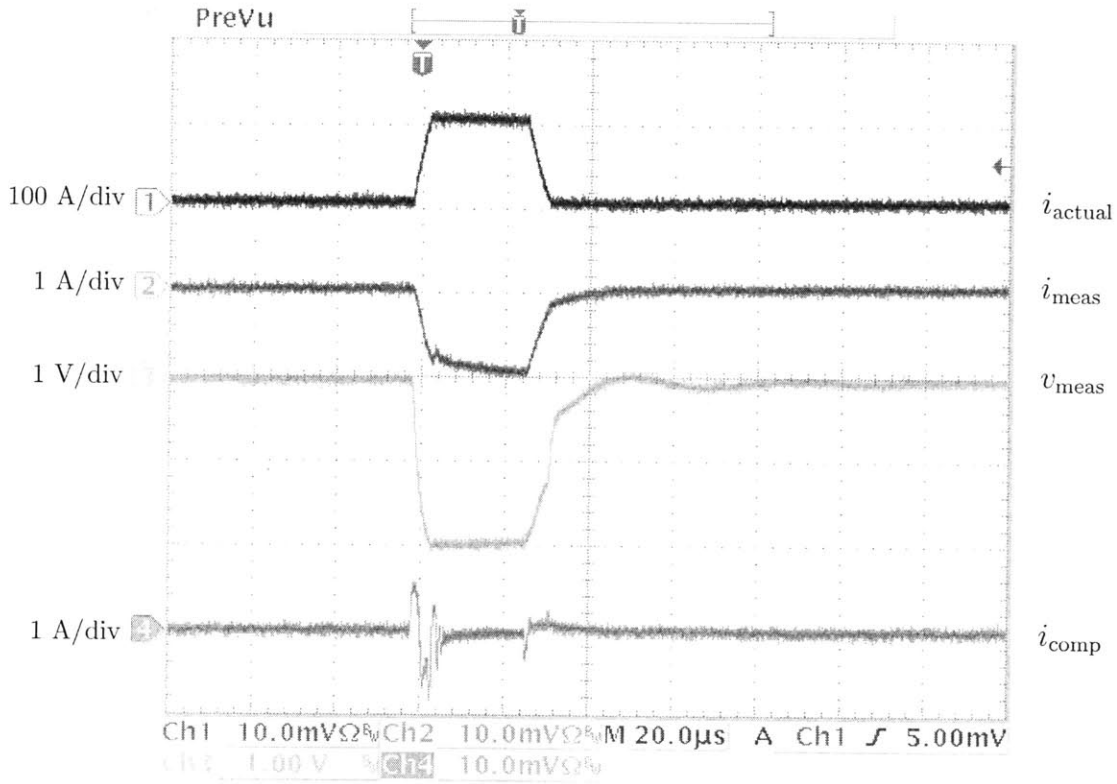


Figure 2.19: System response during a high current transient. A pulse of primary current $i_{\text{actual}}$ =100 A is applied for 25 $\mu$s. The clamp activates, limiting the residual current in the core. After deactivating, the offset measured at the core is less than 5 mV. The compensation current is also shown, demonstrating that it quickly stabilizes back to the commanded value after an induced change.

## 2.6 Summary

The prototype sensor has demonstrated that the physically-windowed approach is able to extend the range of an 11-bit current sensor with a 10-bit compensation command to provide approximately 14-bit resolution in the reconstructed output. The physically-windowed concept separates the bandwidth and dynamic range in the design of the current sensor. The decoupling of the design parameters enables the current sensor to be optimized for the target application, specifically the nonintrusive load monitoring and diagnostic applications.

This technique has many uses in the smart grid and other applications where there is a need to measure fast, small signals on top of slow, large signals. The nonintrusive load monitor suggests many example uses, such as finding the high-frequency principal slot harmonics for motor diagnostics, or examining very small loads in aggregate power metering. The same technique is expected to be applicable to other physical systems, such as pressure monitors and strain gauges, with example uses including water system monitoring and mechanical measurements.

*Chapter 3*

# *Variable Speed Drive Power Estimator*

## 3.1 Introduction

Substantial and successful efforts have been made to develop models that predict the input current harmonics of continuously variable electronic loads such as variable speed drives (VSDs) and rectifier loads given an assumed operating point in real power consumption [35–43]. Specifically, given an assumed or known level of real power consumption and circuit parameters, it is possible to predict the harmonic currents consumed by a variable speed drive. For many applications, it would be convenient and even enabling to have an analytical approach to the inverse problem [9, 12]. That is, a means to model and predict the real power consumption of a drive given an observed or estimated line current harmonic pattern would open the door to new power monitoring and also modeling techniques for constraining motor drive design problems. This paper develops mathematical models that accurately predict real power consumption from measured or estimated input harmonic levels.

These methods can be used, for example, to determine the maximum shaft power available to a drive given specific limits or regulatory requirements on a pattern of input current harmonics. The models developed here can also be used to track and disaggregate the real power consumption of VSDs and rectifier loads given observations of harmonic currents. This type of modeling enables the development of "smart" or nonintrusive electric metering solutions. Nonintrusive "smart" meter-

ing can determine the operating schedule of a collection of electrical loads strictly from measurements made at the electric utility service entry powering a collection of loads [5]. A nonintrusive load monitoring (NILM) system tracks the operating condition and power consumption of multiple loads using line current harmonic signatures or spectral envelopes [5,7,9,12,14]. For a constant power load, the identification is accomplished by searching the aggregate set of current harmonic signatures or spectral envelopes for the appropriate combination of characteristic transient patterns and steady-state power changes [5, 12]. Continuously variable loads like variable speed drives (VSDs) do not have a unique current harmonic signature and can confound the existing nonintrusive power monitoring scheme. The harmonic inverse model presented here can allow the nonintrusive load monitoring system to track and disaggregate the variable power consumption of variable speed drives and rectifiers from tell-tale harmonic signatures.

In general, VSDs are used to optimize energy consumption and controllability in many industrial and commercial facilities. A typical VSD system consists of a rectifier, a dc-bus link, an inverter, and an induction motor. A rectifier front-end of the VSD usually draws current that is rich in harmonic content. These line harmonics can be used to identify and track the VSD load. A VSD power estimator has been developed using correlation functions between the fundamental and higher harmonics of the measured current [12]. Although this curve-fitting approach provides a simple way for extracting the harmonic content of the VSD from the aggregate measurements, the correlation functions used in this black-box approach can change as much as ten percents from the base case [9]. Variation in the input voltage can affect the relative amount of harmonic content consumed by the rectifier [39]. A more accurate model that incorporates system behaviors could provide insights and improvements in estimating power consumption of the VSD using current harmonics.

One analytical technique that provides a closed form solution for the current harmonics drawn by rectifiers uses a switching function approach [35, 37, 41–43]. By

studying the switching function method, the NILM system can approximate linear relationships between higher harmonics uniquely consumed by the VSD and the fundamental harmonic currents consumed by the VSD in the aggregated measurements. The power estimation is performed without knowing the exact operating conditions and circuit parameters of the VSD. This derived relationship allows the system to accurately predict the real power consumption of variable speed drives.

## 3.2 Background

The NILM system monitors multiple loads from a central observation point and extracts information about each load from current and voltage waveforms. The system block diagram is shown in Figure 1.2.

The system computes short-time Fourier series coefficients or spectral envelopes from the measured phase currents and voltages. These coefficients are used to track and disaggregate each load from aggregate measurements [5, 14]. Fourier series coefficients can be computed as follows. Let $v(t) = V_1 \sin(2\pi t/T)$ be a reference voltage and the variable $T$ represents the fundamental period. Given a line current $i(t)$, the in-phase and quadrature components of the $k$th harmonic are denoted by $I_k^{\mathrm{p}}(t)$ and $I_k^{\mathrm{q}}(t)$, respectively. These coefficients can be computed by

$$I_k^{\mathrm{p}}(t) = \frac{2}{T} \int_{t-T}^{t} i(\tau) \sin\left(\frac{2\pi k}{T}\tau\right) d\tau, \tag{3.1}$$

and

$$I_k^{\mathrm{q}}(t) = \frac{2}{T} \int_{t-T}^{t} i(\tau) \cos\left(\frac{2\pi k}{T}\tau\right) d\tau. \tag{3.2}$$

The fundamental real and reactive powers per cycle can be computed by

$$P_1(t) = \frac{1}{2} V_1 I_1^{\mathrm{p}}(t) \tag{3.3}$$

and

$$Q_1(t) = \frac{1}{2} V_1 I_1^{\mathrm{q}}(t), \tag{3.4}$$

respectively for the single-phase load. In the case of three-phase load, the estimated fundamental real and reactive powers of the three-phase load can be computed by

$$P_1(t) = \frac{1}{2} \left( V_1^{\mathrm{a}} I_1^{\mathrm{pa}}(t) + V_1^{\mathrm{b}} I_1^{\mathrm{pb}}(t) + V_1^{\mathrm{c}} I_1^{\mathrm{pc}}(t) \right) \tag{3.5}$$

and

$$Q_1(t) = \frac{1}{2} \left( V_1^{\mathrm{a}} I_1^{\mathrm{qa}}(t) + V_1^{\mathrm{b}} I_1^{\mathrm{qb}}(t) + V_1^{\mathrm{c}} I_1^{\mathrm{qc}}(t) \right) \tag{3.6}$$

respectively. Variables $I_1^{\mathrm{pa}}$ and $I_1^{\mathrm{qa}}$ represent the estimated in-phase and quadrature components of the fundamental current harmonic consumed by the VSD in phase-A. Superscripts a, b, and c indicate the phase of currents and voltages.

When VSDs are included in the group of monitored loads, the time-varying nature of their power consumption can affect the power consumption patterns of other loads. Figure 3.1 shows a snapshot of the current waveform of a 50-Watt light bulb and a VSD over one voltage cycle. Figure 3.2 shows the real power consumption of a 50-Watt light bulb, a VSD, and a three-phase rectifier over a short period. In Figure 3.2, the power signature of the incandescent light bulb has been obscured by the variable power loads. Consequently, the load recognition algorithm may neither match signatures nor disaggregate the individual load power consumption properly.

In order to manage the time-varying characteristic of the VSD power con-

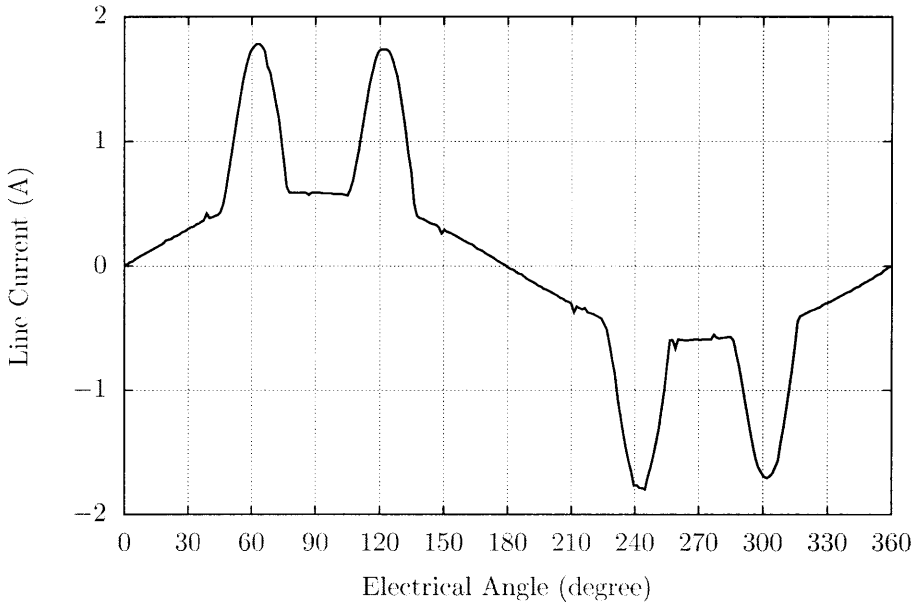


Figure 3.1: A snapshot of the line current consumed by an incandescent light bulb and a VSD over one cycle of the line voltage from the experimental setup

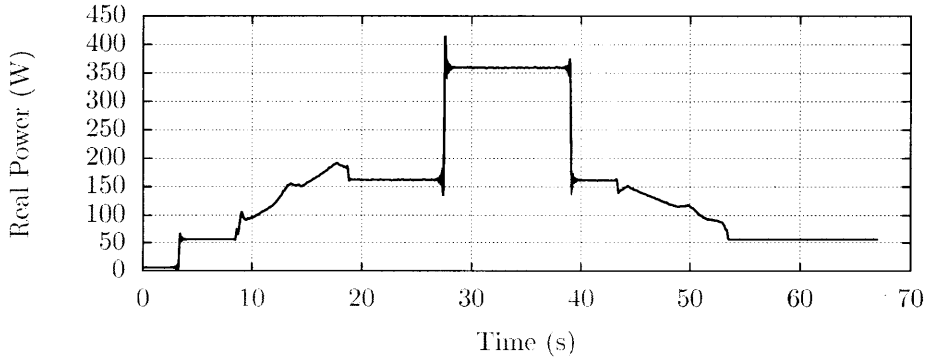


Figure 3.2: Power consumption of three different loads including a VSD, a three-phase rectifier, and an incandescent light bulb from the experimental setup. The light bulb turns on at the time $t = 4$ second, and remains in this state through out this experiment. The VSD starts up at the time $t = 8$ second, and reaches the steady state at the time $t = 18$ second. The fixed-load, three-phase rectifier then turns on at the time $t = 27$ second and turned off at the time $t = 39$ second. The VSD starts to ramp down the power at the time $t = 43$ second and completely stops at the time $t = 53$ second.

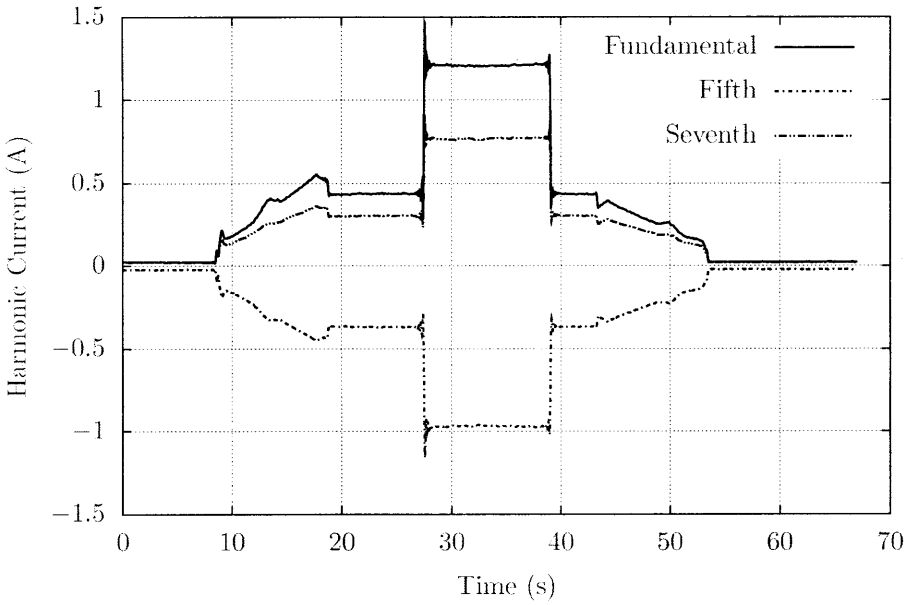


Figure 3.3: Experimental result showing the in-phase components of harmonic currents consumed by the VSD and three-phase rectifier.

sumption, the empirical curve-fitting estimator was developed to exploit the correlation between the fundamental harmonics and higher harmonics [12]. This empirically based estimator derives the estimation function by recording the current harmonics when the VSD is operated by itself and use any tools to generate the curve-fitting parameters. Figure 3.3 shows different current harmonics consumed by the VSD and three-phase rectifier under the experimental setup. Figure 3.3 also demonstrates the correlation between these harmonics. If the one harmonic was plotted against the other harmonic, the graph will clearly show the actual correlation between the two as shown in Figure 3.4. The empirically-based estimator can certainly use this information the identify the fundamental harmonic consumed by the VSD and the three-phase rectifier. This method is a simple and elegant way to cope with any new variable power load such as a VSD. However, the correlation curve may vary over different operating conditions such as voltage variation and distortion causing the estimation errors [12, 17].

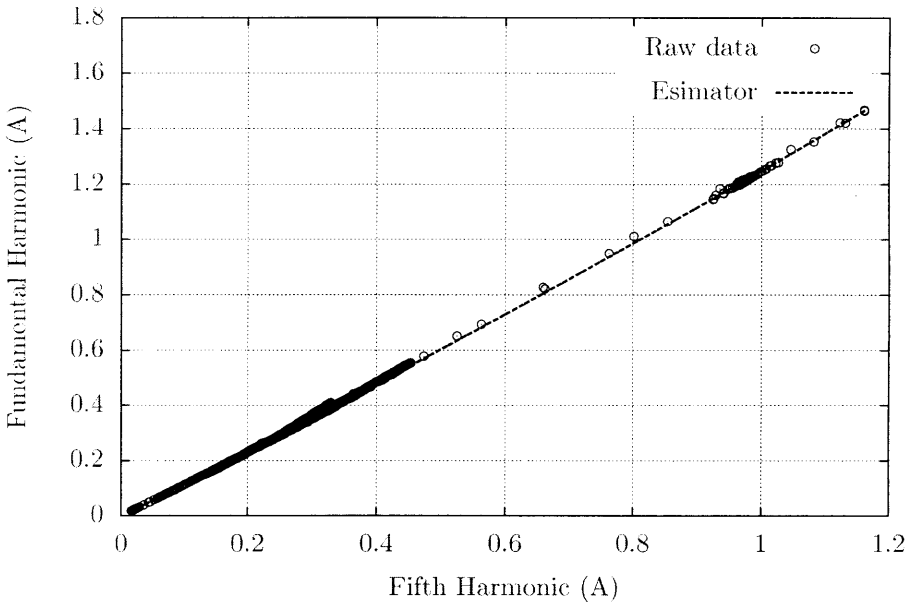


Figure 3.4: Experimental data and the correlation function between the in-phase component of the fundamental and the fifth harmonics used to derive the empirically-based estimator.

To improve the robustness of the estimator against the voltage variation, the VSD power estimator based on a simplified circuit model and the switching function method has been explored. The proposed estimator is shown in Figure 3.5. The algorithm uses the input voltage to approximate a feasible switching function and to create estimating functions for the fundamental current consumed by the VSD from a finite set of higher harmonics uniquely associated with the drive. Finally, the estimator computes the fundamental real and reactive powers consumed by the VSD using (3.5) and (3.6) respectively. Sections below describe the operation of the VSD and present a method for estimating and removing the harmonic currents consumed by the VSD.

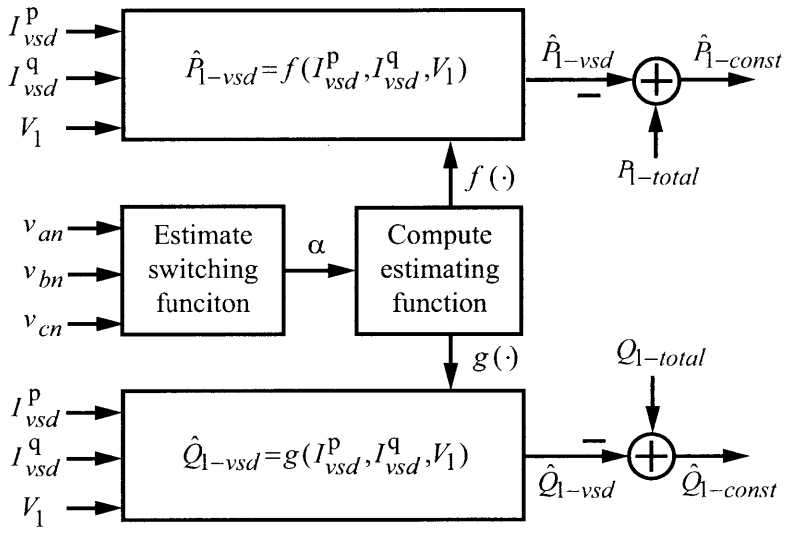


Figure 3.5: Block diagram of the model-based VSD power estimator. The three input voltages are used to estimate the switching functions and the angle $\alpha$. The angle $\alpha$ is then used to compute the estimating functions $f()$ for the real power consumption, and $g()$ for the reactive power consumption.

## 3.3 VSD Model

A simple circuit topology that represents a VSD system with an uncontrolled rectifier is shown in Figure 3.6 [39]. This circuit topology represents a voltage-source-inverter (VSI) system, which is mostly used in low and medium power applications. A dc-bus capacitor is installed to provide an intermediate energy storage and to minimize the voltage ripple during the rectification. An optional dc-bus inductor can be included to reduce the peak current. The inverter is normally operated at a frequency well above line frequency, so any harmonics it produces are generally negligible at the ac side [40]. Simulation results show that the constant current source, $i_{load}$, provides a good model for the inverter-motor combination [39]. As a result, the model shown in Figure 3.6 provides a good representation of the VSD system for simulation and initial verification purposes.

A typical ac-side line current consumed by a VSD with an uncontrolled rectifier exhibits two separate peaks during each half cycle as shown in Figure 3.7. In this case,

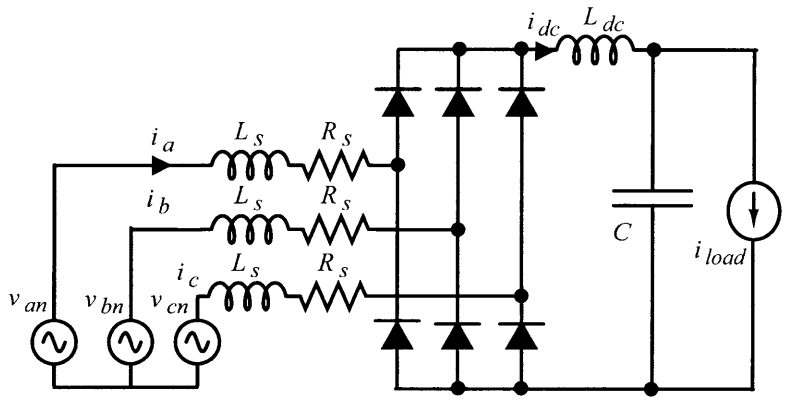


Figure 3.6: A simple circuit model of the VSD equipped with an uncontrolled rectifier used to simulate the VSD current waveforms. The constant current $i_{load}$ represents the electrical behavior of the three-phase inverter and the three-phase induction motor.

the VSD system is said to be operating in a discontinuous conduction mode (DCM) because the line current reaches zero before the next set of diodes have turned on. The current waveform of the VSD and the three-phase rectifier is different from the current consumed by the motors, which primarily consume the fundamental harmonic current, assuming a balanced sinusoidal input voltage. The time-domain signal is easily corrupted by various noise sources, making it an unreliable choice to distinguish between the motor and the VSD when both loads are operating simultaneously. The frequency content of the current is used instead because they are more reliable and less prone to the random noise corruption.

In the case of the VSD operating in the DCM, the measured current mainly consists of the fundamental and a series of odd harmonics, i.e. 5th, 7th, 11th, and 13th according to the frequency analysis. Assuming these higher harmonics are uniquely associated with the VSD, these higher harmonic currents can be used to estimate the fundamental harmonic and the fundamental power consumed by the VSD using the proposed process shown in Figure 3.5.

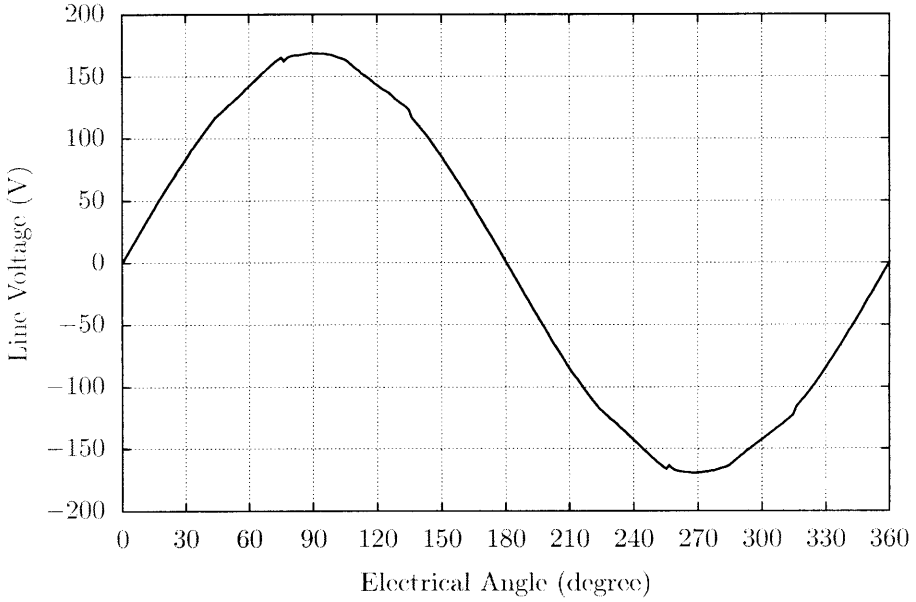


(a) Voltage

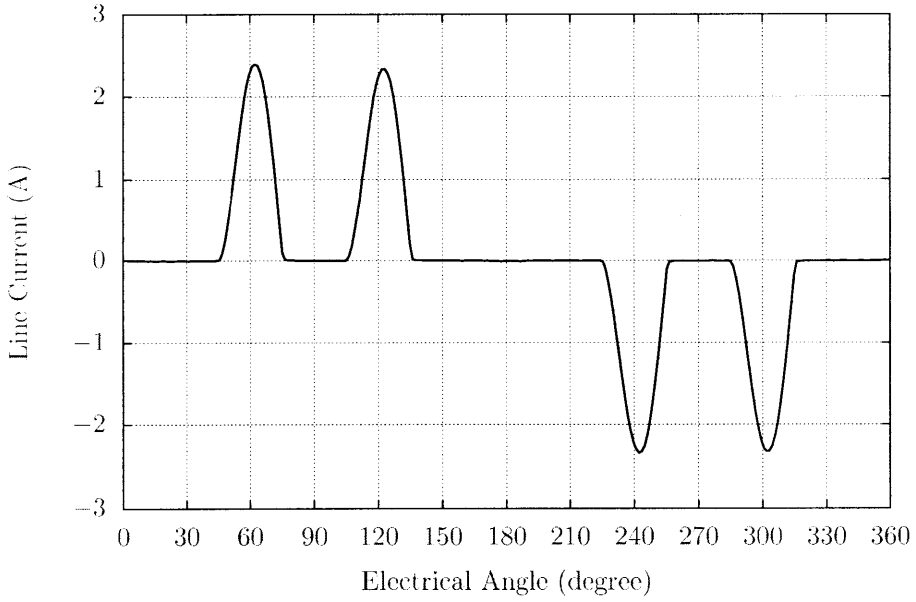


(b) Current

Figure 3.7: Simulated line current and reference input voltage waveforms consumed by the uncontrolled rectifier in the VSD from the experimental result. The line-to-neutral voltage $v_{an}$ is shown in (a), and the line current $i_a$ is shown in (b).

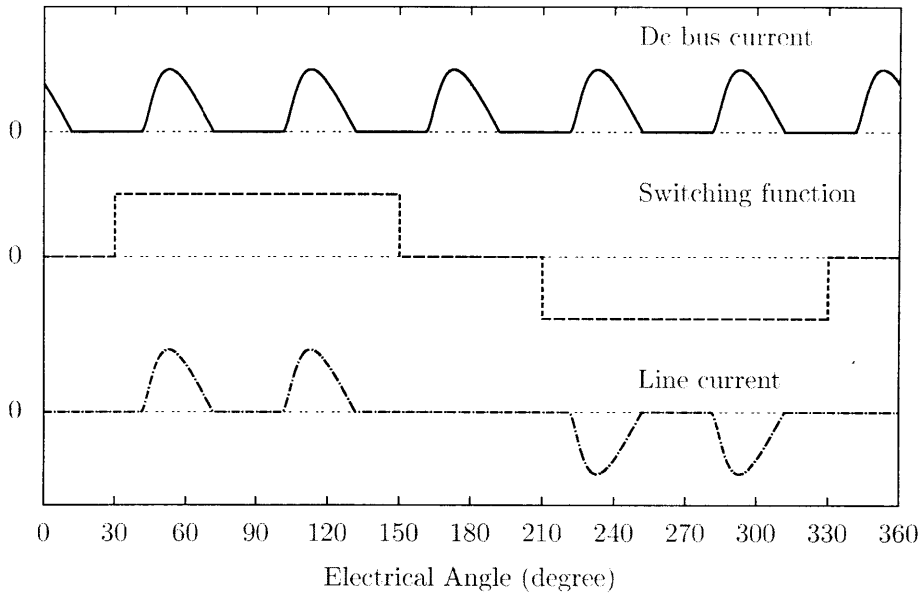


Figure 3.8: Examples of the dc-bus current, the switching function, and the ac-side current when the input voltages are balanced and the VSD system is operating in a steady state from the simulation

## 3.4 Switching Function

This section describes the algorithm to use the switching function to find the functional relationship between higher harmonics and the fundamental harmonics of the VSD with the uncontrolled rectifier. Let the observed line-to-neutral voltage on phase-A, $v_{\mathrm{an}}(\theta) = V_1 \sin\theta$, be a reference voltage, where $\theta \in [0, 2\pi)$ is an electrical angle and $V_1$ is the magnitude of the fundamental. During each voltage cycle, the observed phase-A current, $i_{\mathrm{a}}(\theta)$, is the result of the modulation of the dc-side current, $i_{\mathrm{dc}}(\theta)$, by the corresponding switching function, $s_{\mathrm{a}}(\theta)$. The switching function represents the on/off times of the switches in the rectifier. Examples of current and switching function waveforms are shown in Figure 3.8. Mathematically, the phase-A line current is given by

$$i_{\mathrm{a}}(\theta) = s_{\mathrm{a}}(\theta) i_{\mathrm{dc}}(\theta). \tag{3.7}$$

Each variable in (3.7) can be represented in terms of dc, in-phase, and quadrature components using a Fourier analysis. The line current is the result of the convolution between the switching function and the dc-bus current [35]. The line current is represented as

$$i_a(\theta) = I^0 + \sum_k \left(I_k^{\mathrm{p}} \sin(k\theta) - I_k^{\mathrm{q}} \cos(k\theta)\right), \tag{3.8}$$

where the subscript $k$ represents a harmonic number, the variable $I^0$ is the dc component of the line current, and the variables $I_k^{\mathrm{p}}$ and $I_k^{\mathrm{q}}$ are the magnitudes of the in-phase and quadrature components of the line-side $k$th current harmonic, respectively. An arbitrary switching function can also be represented as

$$s_a(\theta) = S^0 + \sum_n \left(S_n^{\mathrm{p}} \sin(n\theta) - S_n^{\mathrm{q}} \cos(n\theta)\right), \tag{3.9}$$

where the subscript $n$ indicates the harmonic number, the variable $S^0$ is the dc component, and the variables $S_n^{\mathrm{p}}$ and $S_n^{\mathrm{q}}$ represent the magnitudes of the in-phase and quadrature components of the $n$th harmonic of the switching function, respectively. Similarly, the dc-bus current can be represented by another Fourier series as

$$i_{dc}(\theta) = I^{0\mathrm{dc}} + \sum_m \left(I_m^{\mathrm{pdc}} \cos(m\theta) + I_m^{\mathrm{qdc}} \sin(m\theta)\right), \tag{3.10}$$

where the subscript $m$ is the harmonic number, the variable $I^{0\mathrm{dc}}$ is the dc-side component, and the variables $I_m^{\mathrm{pdc}}$ and $I_m^{\mathrm{qdc}}$ represent the magnitudes of the in-phase and quadrature components of the $m$th harmonic of the dc-side current, respectively.

The line current can be rewritten in terms of its Fourier series coefficients by

substituting (3.9) and (3.10) in (3.7),

$$I^0 + \sum_k \left(I_k^{\mathrm{p}} \sin(k\theta) - I_k^{\mathrm{q}} \cos(k\theta)\right) = \left(S^0 + \sum_n \left(S_n^{\mathrm{p}} \sin(n\theta) - S_n^{\mathrm{q}} \cos(n\theta)\right)\right) \times \left(I^{0\mathrm{dc}} + \sum_m \left(I_m^{\mathrm{pdc}} \cos(m\theta) + I_m^{\mathrm{qdc}} \sin(m\theta)\right)\right). \tag{3.11}$$

By expanding and rearranging terms in (3.11), Fourier series coefficients $I^0$, $I_k^{\mathrm{p}}$, and $I_k^{\mathrm{q}}$ are can be described by a weighted sum of the dc-side Fourier series coefficients as

$$I^0 = W^{00} I^{0\mathrm{dc}} + W^{0\mathrm{p}} I^{\mathrm{pdc}} + W^{0\mathrm{q}} I^{\mathrm{qdc}}, \tag{3.12}$$

$$I_k^{\mathrm{p}} = W_k^{\mathrm{p}0} I^{0\mathrm{dc}} + W_k^{\mathrm{pp}} I^{\mathrm{pdc}} + W_k^{\mathrm{pq}} I^{\mathrm{qdc}}, \tag{3.13}$$

and

$$I_k^{\mathrm{q}} = W_k^{\mathrm{q}0} I^{0\mathrm{dc}} + W_k^{\mathrm{qp}} I^{\mathrm{pdc}} + W_k^{\mathrm{qq}} I^{\mathrm{qdc}}. \tag{3.14}$$

The column vector $I^{\mathrm{pdc}}$ represents the in-phase components of the dc-side harmonics

$$I^{\mathrm{pdc}} = \begin{bmatrix} I_1^{\mathrm{pdc}} & I_2^{\mathrm{pdc}} & I_3^{\mathrm{pdc}} & \dots \end{bmatrix}^T, \tag{3.15}$$

and the column vector $I^{\mathrm{qdc}}$ represents the quadrature components of the dc-side harmonics

$$I^{\mathrm{qdc}} = \begin{bmatrix} I_1^{\mathrm{qdc}} & I_2^{\mathrm{qdc}} & I_3^{\mathrm{qdc}} & \dots \end{bmatrix}^T. \tag{3.16}$$

The coefficient $W^{00}$ relates the dc component from the bus current to the dc component of the line current. Row vectors $W^{0\mathrm{p}}$ and $W^{0\mathrm{q}}$ contain the weighting coefficients that relate the in-phase and quadrature components of the dc-side harmonics to the dc component of the line-side current, respectively. The row vector $W_k^{\mathrm{pp}}$ relates the in-

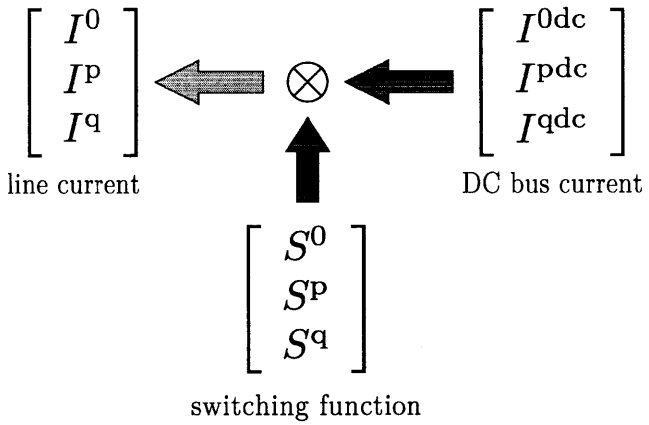


Figure 3.9: The process of computing the line current harmonic as a modulation of the dc-bus current by the switching function

phase components of the dc-side harmonics to the in-phase component of the line-side $k$th harmonic. The row vector $W_k^{pq}$ relates the quadrature components of the dc-side harmonics to the in-phase component of the line-side $k$th harmonic. The row vector $W_k^{qp}$ relates the in-phase components of the dc-side harmonics to the quadrature component of the line-side $k$th harmonic. The row vector $W_k^{qq}$ relates the quadrature components of the dc-side harmonics to the quadrature component of the line-side $k$th harmonic. These weighting coefficients can be computed from switching function coefficients, $S^0$, $S_n^p$, and $S_n^q$. The computation of these coefficients are included in Appendix B.

In other words, the equation (3.11) describes the line-side harmonic as a modulation between the dc-side current and the switching function. The Fourier coefficients of the line-current are the results of the convolution between the Fourier coefficients of the dc-side current and the switching function. The modulation process is shown in Figure 3.9. This process is a forward problem assuming the knowledge of the switching function and the dc-bus current harmonics. If both the switching function and the dc-side harmonics are known, all VSD line-side harmonics can be readily computed using (3.12), (3.13), and (3.14).

However, in the NILM application, the goal is to relate between higher harmonics of the VSD to its fundamental. The deconvolution process can not be used directly to recover the dc-bus current because it may involve the division by zero of the Fourier coefficients. The proposed method would apply certain approximations and linear algebra methods to recover the dc-bus Fourier coefficients in order to predict the fundamental harmonic consumed by the VSD from the observed higher harmonics. The details of the algorithm are described in the next section.

## 3.5 Estimator Derivation

In the load identification problem, the dc-bus current and the switching function are generally not observable in the aggregate measurements. Few approximations must be applied in order to relate higher current harmonics to the fundamental harmonic consumed by the VSD. The derivation of the proposed estimator can be divided into two parts: the estimation of the switching function and the estimation of the dc-side current harmonics. In the work, the following conditions are assumed:

- the rectifier front-end is operated in a discontinuous conduction mode (DCM),
- each diode behaves like an ideal switch, and
- harmonics used in the estimator are uniquely consumed by the VSD.

### 3.5.1 Switching Function Approximation

The actual switching function is defined by switching instants of the diode bridge and is not always observable in the aggregate measurement. In DCM, intersections between line voltages can be used to estimate the switching functions of the line currents because the line currents do not commutate during the switching instants. In order

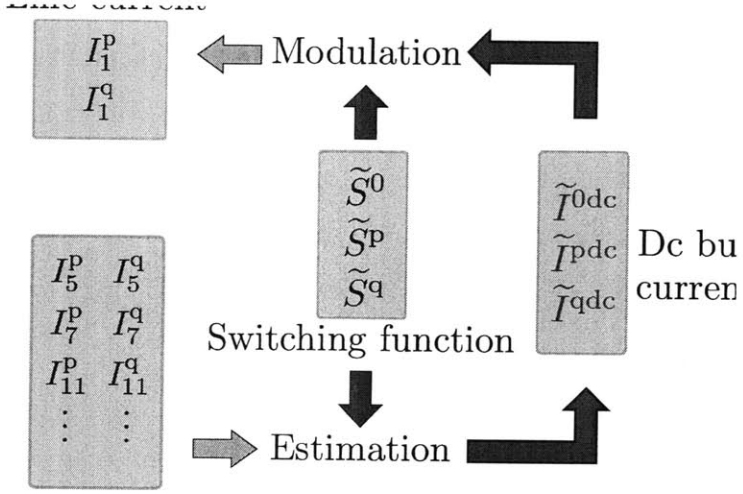


Figure 3.10: Block diagram showing the process of estimating the VSD fundamental harmonic current from a set of higher harmonic currents

to demonstrate the algorithm development, three types of switching functions are discussed below, specifically the ideal, shifted-ideal, and general switching functions.

#### 3.5.1.1 Ideal Switching Function

Under the idealized condition where the three-phase voltages are balanced and the rectifier loads are in steady state, the input voltages are shifted by 120 degrees from one another. The intersections between different line voltages can be clearly seen in Figure 3.11 below. Mathematically, the switching function for phase-A current is described by

$$s_{\mathrm{a}}(\theta) = \begin{cases} 1 & \text{for } \frac{\pi}{6} \leq \theta \leq \frac{5\pi}{6}, \quad (3.17a) \\ -1 & \text{for } \frac{7\pi}{6} \leq \theta \leq \frac{11\pi}{6}, \quad (3.17b) \\ 0 & \text{otherwise.} \quad (3.17c) \end{cases}$$

The switching function in (3.17) can be decomposed into Fourier series coefficients according to (3.9). The Fourier series coefficients of the ideal switching function can

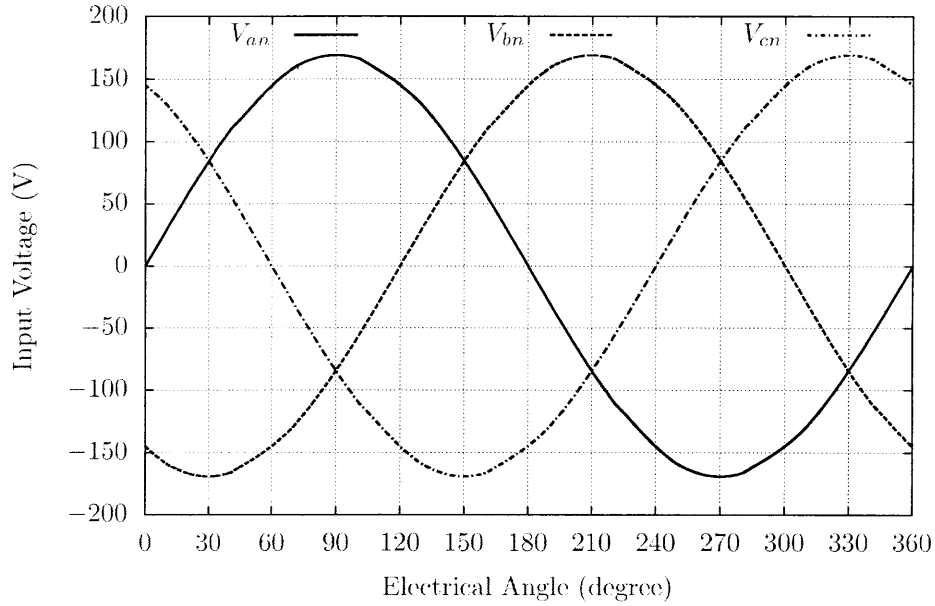


(a)

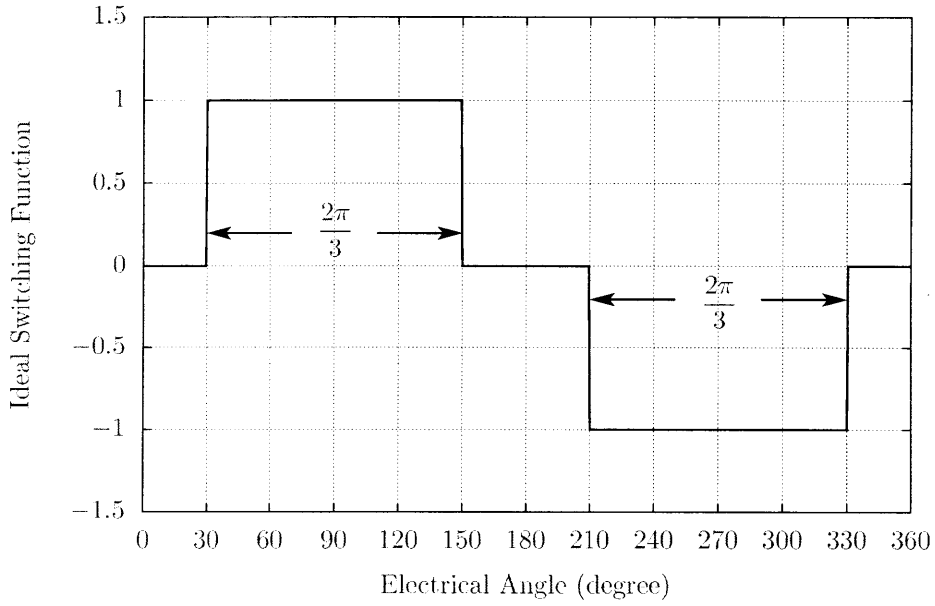


(b)

Figure 3.11: Simulation results showing the ideal switching function for phase-A current and the ideal three-phase voltage when the input voltages are balanced

be expressed as

$$S^0 = 0, \tag{3.18}$$

$$S_n^{\mathrm{p}} = -\frac{4}{n\pi}\sin\frac{n\pi}{2}\sin\frac{n\pi}{3}\cos n\pi, \tag{3.19}$$

and

$$S_n^{\mathrm{q}} = -\frac{4}{n\pi}\sin\frac{n\pi}{2}\sin\frac{n\pi}{3}\sin n\pi = 0. \tag{3.20}$$

The ideal switching function results in many zero coefficients. Therefore, the calculation of the weighting coefficient vectors $W^{00}$, $W^{0\mathrm{p}}$, $W^{0\mathrm{q}}$, $W_k^{\mathrm{p}0}$, $W_k^{\mathrm{pp}}$, $W_k^{\mathrm{pq}}$, $W_k^{\mathrm{q}0}$, $W_k^{\mathrm{qp}}$, and $W_k^{\mathrm{qq}}$ can be simplified significantly.

#### 3.5.1.2 Approximated Switching Function

In the case of the non-ideal situation where the voltage may have shifted or slightly unbalanced, the switching function can be modified to account for the non-ideal situation. The approximated switching function is the shifted ideal switching function that can be expressed as

$$s_{\mathrm{a}}(\theta) = \begin{cases} 1 & \text{for } \alpha \le \theta \le \alpha + \frac{2\pi}{3}, \quad (3.21\mathrm{a}) \\ -1 & \text{for } \alpha + \pi \le \theta \le \alpha + \frac{5\pi}{3}, \quad (3.21\mathrm{b}) \\ 0 & \text{otherwise}, \quad (3.21\mathrm{c}) \end{cases}$$

where the angle $\alpha$ is the minimum angle that allows the shifted ideal switching function to contain all four pulses for phase-A. An example of the approximated switching function is shown in Figure 3.12. Fourier series coefficients $S_n^{\mathrm{p}}$ and $S_n^{\mathrm{q}}$ of the approximate switching function in (3.21) are given by

$$S_n^{\mathrm{p}} = -\frac{4}{n\pi}\sin\frac{n\pi}{2}\sin\frac{n\pi}{3}\cos n(\frac{5\pi}{6} + \alpha), \tag{3.22}$$

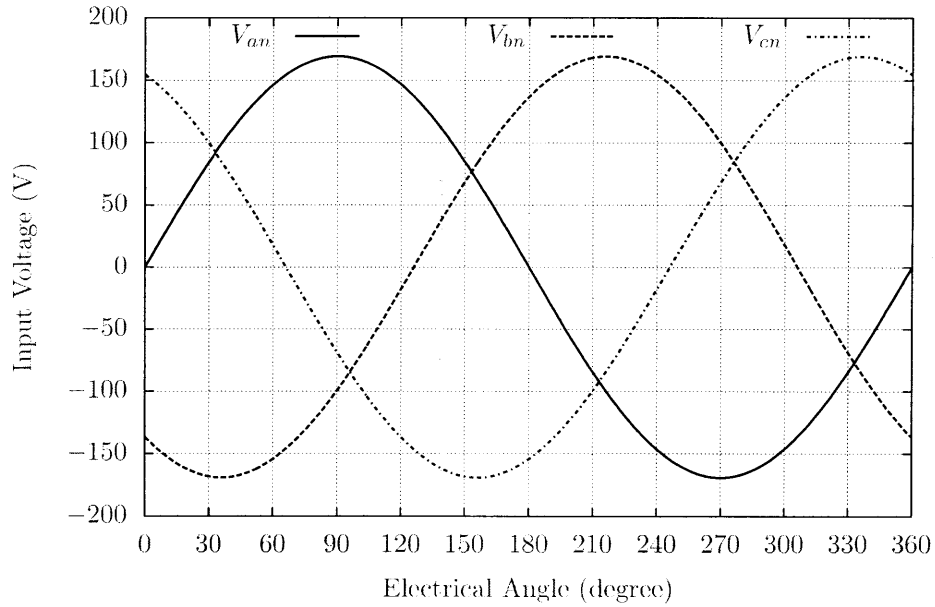


(a)

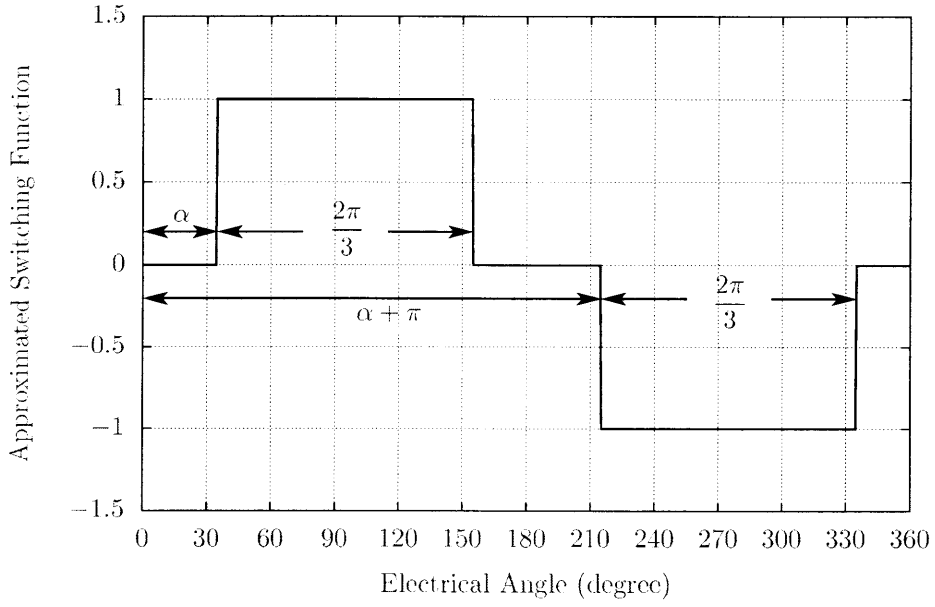


(b)

Figure 3.12: Simulation results showing the non-ideal input voltage and approximated switching function for the phase-A current

and

$$S_n^{\mathrm{q}} = -\frac{4}{n\pi}\sin\frac{n\pi}{2}\sin\frac{n\pi}{3}\sin n(\frac{5\pi}{6}+\alpha). \tag{3.23}$$

The vectors $W_k^{\mathrm{pp}}$, $W_k^{\mathrm{pq}}$, $W_k^{\mathrm{qp}}$, and $W_k^{\mathrm{qq}}$ computed from the approximated switching function contain many zeros, making the simplification possible. For example, the coefficient matrix for the fundamental current harmonic $W_1^{\mathrm{pp}}$ is given by

$$W_1^{\mathrm{pp}} = \left[0, w_{1,2}^{\mathrm{pp}}, 0, w_{1,4}^{\mathrm{pp}}, 0, w_{1,6}^{\mathrm{pp}}, \cdots\right],$$

where the coefficient $w_{k,m}^{\mathrm{pp}}$ is the coefficient of the dc-side harmonic $I_m^{\mathrm{pdc}}$ for the calculation of the ac-side harmonic $I_k^{\mathrm{p}}$. Furthermore, all line-side triplen harmonics only depend on dc-side even harmonics that are not multiple of six. For example, the weighting vector for the third harmonic $W_3^{\mathrm{pp}}$ is given by

$$W_3^{\mathrm{pp}} = \left[0, w_{3,2}^{\mathrm{pp}}, 0, w_{3,4}^{\mathrm{pp}}, 0, \mathbf{0}, 0, w_{3,8}^{\mathrm{pp}}, \cdots\right].$$

This property excludes the contribution of some subsets of the dc-side harmonic from the triplen harmonics. The algorithm can use this property to decouple the triplen harmonic from other harmonic in the calculation. The explanation is included in the next section. Finally, the $k$th ac-side harmonic is primarily caused by the $(k-1)$th and $(k+1)$th dc-side harmonics when the shifted, ideal switching function shown above is used. These properties can be used to further simplify the estimation problem.

### 3.5.2 Dc-side Harmonics Approximation

In the ideal case, the input voltage is balanced and the inverter reaches steady state. The dc-side current consumed by the uncontrolled three-phase rectifier consists of six identical pulses per line cycle. According to the frequency analysis of the dc-

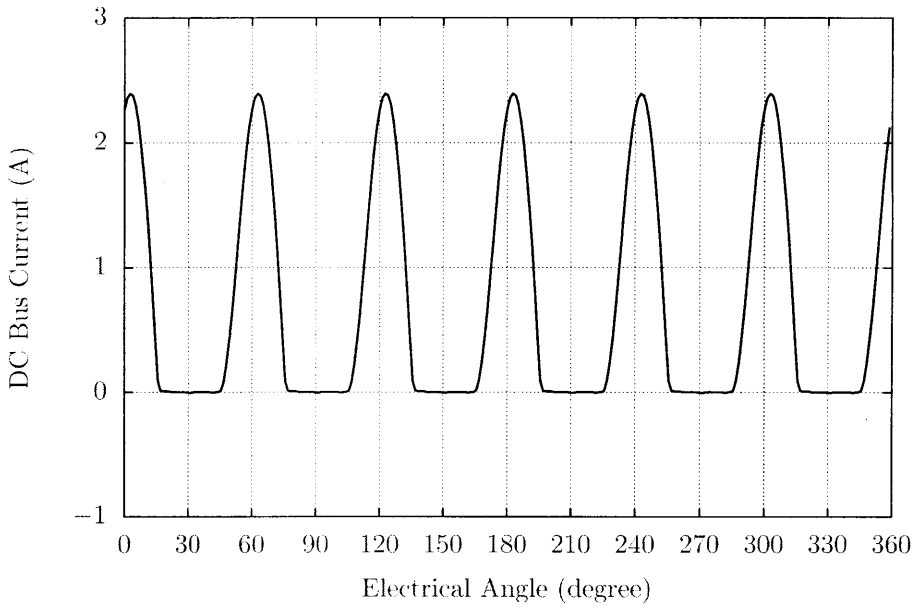


Figure 3.13: Simulated dc-bus current of the VSD three-phase uncontrolled rectifier

side current, the dc-side current contains only the dc component and harmonics that are multiples of six. Figure 3.13 shows an example of dc-bus current and the corresponding dc-bus harmonics normalized by the dc component from simulation. In this case, dc-side harmonics are reduced to $I^{0\mathrm{dc}}$ and the subset of the vectors $I^{\mathrm{pdc}}$ and $I^{\mathrm{qdc}}$. Specifically these vectors include only the harmonic that are multiple of six, $[I_6^{\mathrm{pdc}}, I_{12}^{\mathrm{pdc}}, I_{18}^{\mathrm{pdc}}, \cdots]^T$ and $[I_6^{\mathrm{qdc}}, I_{12}^{\mathrm{qdc}}, I_{18}^{\mathrm{qdc}}, \cdots]^T$ respectively. Figure 3.13 shows the normalized harmonic content of the dc-side current waveform in Figure 3.14.

In general, the rectifier has a dc-bus filter to smooth out the current and suppress higher harmonics. Theoretically, each current pulse in Figure 3.8 can be assumed to be a square pulse. In this case, the magnitude of the dc-side $m$th harmonic would be proportional to $1/m$ according to Fourier series coefficients. Furthermore, the approximated switching function shown in Figure 3.12 also attenuates higher harmonics according to Fourier series coefficients computed in (3.22) and (3.23). As a result, the impacts of the dc-side higher harmonics on the ac-side low harmonics are further reduced. Therefore, many higher harmonics can be ignored. The effect of

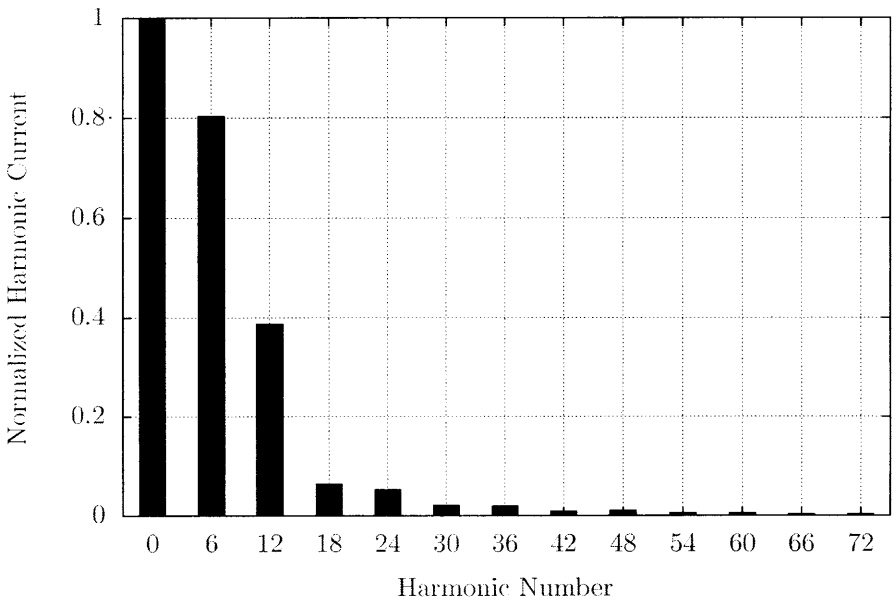


Figure 3.14: Simulated dc-side harmonic current of the three-phase uncontrolled rectifier normalized by the averaged value of the dc-side current

neglected higher harmonics can be computed quantitatively by the comparing the $\mathcal{L}_2$ norm of the unused higher harmonics and the retained harmonics to ensure that the approximation error is reasonably small in any specific application context.

Consequently, the harmonic vectors $I^{\text{pdc}}$ and $I^{\text{qdc}}$ can be divided into two parts: main and residual harmonics. Main harmonics include the first $M$ entries of dc-side harmonic vectors represented by

$$I^{\text{pdcm}} = \overbrace{[I_6^{\text{pdc}}, I_{12}^{\text{pdc}}, I_{18}^{\text{pdc}} ...]}^{\text{M terms}} \tag{3.24}$$

and

$$I^{\text{qdcm}} = \overbrace{[I_6^{\text{qdc}}, I_{12}^{\text{qdc}}, I_{18}^{\text{qdc}}, ...]}^{\text{M terms}}. \tag{3.25}$$

Residual harmonics include all other higher harmonics represented by

$$\Delta I^{\mathrm{pdcm}} = [I^{\mathrm{pdc}}_{6(M+1)}, I^{\mathrm{pdc}}_{6(M+2)}, I^{\mathrm{pdc}}_{6(M+3)}, \cdots] \tag{3.26}$$

and

$$\Delta I^{\mathrm{qdcm}} = [I^{\mathrm{qdc}}_{6(M+1)}, I^{\mathrm{qdc}}_{6(M+2)}, I^{\mathrm{qdc}}_{6(M+3)}, \cdots]. \tag{3.27}$$

In this case, the fundamental harmonic of the line current can be approximated as

$$\left[\begin{array}{c} I^{\mathrm{p}}_1 \\ \hline I^{\mathrm{q}}_1 \end{array}\right] \approx \left[\begin{array}{c|c|c} W^{\mathrm{p0}}_1 & W^{\mathrm{ppm}}_1 & W^{\mathrm{pqm}}_1 \\ \hline W^{\mathrm{q0}}_1 & W^{\mathrm{qpm}}_1 & W^{\mathrm{qqm}}_1 \end{array}\right] \left[\begin{array}{c} I^{\mathrm{0dc}} \\ \hline I^{\mathrm{pdcm}} \\ \hline I^{\mathrm{qdcm}} \end{array}\right], \tag{3.28}$$

where block matrices $W^{\mathrm{ppm}}_1$, $W^{\mathrm{pqm}}_1$, $W^{\mathrm{qpm}}_1$, and $W^{\mathrm{qqm}}_1$ contain $M$ coefficients that correspond to $M$ harmonics used in the vector $I^{\mathrm{pdcm}}$ and $I^{\mathrm{qdcm}}$ for the fundamental ac-side harmonic components $I^{\mathrm{pdc}}_1$ and $I^{\mathrm{qdc}}_1$.

Similarly, higher harmonics of the line current consumed by the VSD can be expressed as

$$\left[\begin{array}{c} I^{\mathrm{p}}_{\mathrm{vsd}} \\ \hline I^{\mathrm{q}}_{\mathrm{vsd}} \end{array}\right] \approx \left[\begin{array}{c|c|c} W^{\mathrm{p0}}_{\mathrm{vsd}} & W^{\mathrm{ppm}}_{\mathrm{vsd}} & W^{\mathrm{pqm}}_{\mathrm{vsd}} \\ \hline W^{\mathrm{q0}}_{\mathrm{vsd}} & W^{\mathrm{qpm}}_{\mathrm{vsd}} & W^{\mathrm{qqm}}_{\mathrm{vsd}} \end{array}\right] \left[\begin{array}{c} I^{\mathrm{0dc}} \\ \hline I^{\mathrm{pdcm}} \\ \hline I^{\mathrm{qdcm}} \end{array}\right]. \tag{3.29}$$

The vector $I^{\mathrm{p}}_{\mathrm{vsd}}$ represents the in-phase components of the harmonic currents uniquely consumed by the VSD, which can be given by

$$I^{\mathrm{p}}_{\mathrm{vsd}} = \overbrace{[I^{\mathrm{p}}_5, I^{\mathrm{p}}_7, I^{\mathrm{p}}_{11}, \cdots]^T}^{\text{M terms}}. \tag{3.30}$$

The vector $I^{q}_{vsd}$ represents the quadrature components of the harmonic currents uniquely consumed by the VSD, which can be given by

$$I^{q}_{vsd} = \overbrace{[I^{q}_{5}, I^{q}_{7}, I^{q}_{11}, \cdots]^{T}}^{\text{M terms}}. \tag{3.31}$$

Matrices $W^{p0}_{vsd}$, $W^{ppm}_{vsd}$, $W^{pqm}_{vsd}$,$W^{q0}_{vsd}$, $W^{qpm}_{vsd}$, and $W^{qqm}_{vsd}$ contain corresponding coefficients for the higher harmonics consumed by the VSD.

Let

$$W^{m}_{1} = \left[\begin{array}{c|c|c} W^{p0} & W^{ppm}_{1} & W^{pqm}_{1} \\ \hline W^{q0} & W^{qpm}_{1} & W^{qqm}_{1} \end{array}\right] \tag{3.32}$$

and

$$W^{m}_{vsd} = \left[\begin{array}{c|c|c} W^{p0}_{vsd} & W^{ppm}_{vsd} & W^{pqm}_{vsd} \\ \hline W^{q0}_{vsd} & W^{qpm}_{vsd} & W^{qqm}_{vsd} \end{array}\right] \tag{3.33}$$

then the estimated fundamental harmonic components consumed by the VSD are given by

$$\left[\begin{array}{c} \widehat{I}^{p}_{vsd1} \\ \hline \widehat{I}^{q}_{vsd1} \end{array}\right] = W^{m}_{1}(W^{m}_{vsd})^{-1} \left[\begin{array}{c} I^{p}_{vsd} \\ \hline I^{q}_{vsd} \end{array}\right], \tag{3.34}$$

Because the matrix $W^{m}_{vsd}$ depends on the shifted angle $\alpha$, which can be singular in some cases. However, the ill-conditioned matrix can be tested off-line and the problem can be mitigated by reducing the dimension of matrix $W^{m}_{vsd}$.

In general, the input voltage may be slightly unbalanced or distorted and the system may never reach steady-state. As a result, each current pulse in the line cycle may be different as shown in Figure 3.15. In this case, additional ac-side harmonics

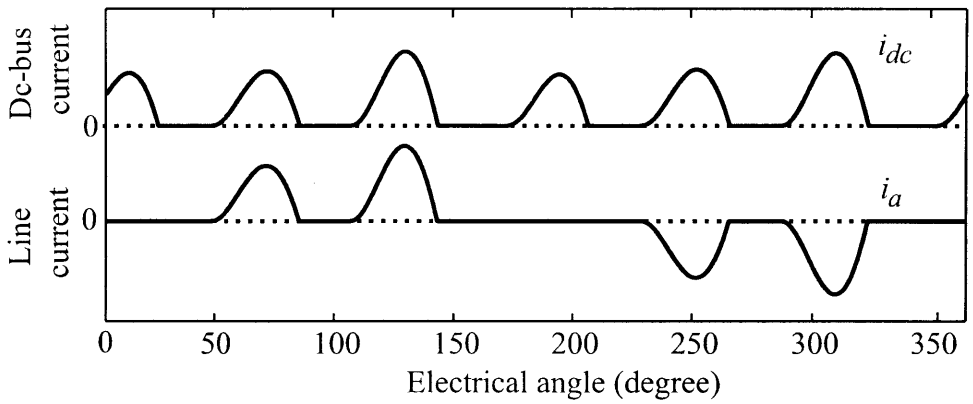


Figure 3.15: Examples of dc-bus and ac-side current waveforms in a general case.

are required to accurately estimate the dc-side harmonics. Using the approximated switching function, triplen harmonics can be used to estimate additional even dc-side harmonics.

Let $I^{\mathrm{pdcx}} = [I_2^{\mathrm{pdc}}, I_4^{\mathrm{pdc}}, I_8^{\mathrm{pdc}}, I_{10}^{\mathrm{pdc}}]^T$ be additional dc-side harmonics to be considered. Other higher-order even harmonics are represented by $\Delta I^{\mathrm{pdcx}} = [I_{14}^{\mathrm{pdc}}, I_{16}^{\mathrm{pdc}}, I_{20}^{\mathrm{pdc}}, \cdots]^T$. Additional ac-side harmonics used in the estimation are included in the vector $I_{\mathrm{x}}^{\mathrm{p}} = [I_3^{\mathrm{p}}, I_9^{\mathrm{p}}]^T$. Similar vectors can be written for the quadrature components, $I^{\mathrm{qdcx}} = [I_2^{\mathrm{qdc}}, I_4^{\mathrm{qdc}}, I_8^{\mathrm{qdc}}, I_{10}^{\mathrm{qdc}}]^T$, $\Delta I^{\mathrm{qdcx}} = [I_{14}^{\mathrm{qdc}}, I_{16}^{\mathrm{qdc}}, I_{20}^{\mathrm{qdc}}, \cdots]^T$, and $I_{\mathrm{x}}^{\mathrm{q}} = [I_3^{\mathrm{q}}, I_9^{\mathrm{q}}]^T$. Additional dc-side harmonics change (3.28) and (3.29) to

$$\begin{bmatrix} I_1^{\mathrm{p}} \\ \hline I_1^{\mathrm{q}} \end{bmatrix} \approx W_1^{\mathrm{m}} \begin{bmatrix} I^{\mathrm{pdcm}} \\ \hline I^{\mathrm{qdcm}} \end{bmatrix} + W_1^{\mathrm{x}} \begin{bmatrix} I^{\mathrm{pdcx}} \\ \hline I^{\mathrm{qdcx}} \end{bmatrix}, \tag{3.35}$$

and

$$\begin{bmatrix} I_{\mathrm{vsd}}^{\mathrm{p}} \\ \hline I_{\mathrm{vsd}}^{\mathrm{q}} \end{bmatrix} \approx W_{\mathrm{vsd}}^{\mathrm{m}} \begin{bmatrix} I^{\mathrm{pdcm}} \\ \hline I^{\mathrm{qdcm}} \end{bmatrix} + W_{\mathrm{vsd}}^{\mathrm{x}} \begin{bmatrix} I^{\mathrm{pdcx}} \\ \hline I^{\mathrm{qdcx}} \end{bmatrix}. \tag{3.36}$$

A similar equation can be written for the triplen harmonics as

$$\left[\frac{I_{\mathrm{x}}^{\mathrm{p}}}{I_{\mathrm{x}}^{\mathrm{q}}}\right] \approx W_{\mathrm{x}}^{\mathrm{x}} \left[\frac{I^{\mathrm{pdcx}}}{I^{\mathrm{qdcx}}}\right]. \tag{3.37}$$

Matrices $W_1^{\mathrm{x}}$, $W_{\mathrm{vsd}}^{\mathrm{x}}$, and $W_{\mathrm{x}}^{\mathrm{x}}$ contain corresponding coefficients for the selected triplen harmonics. The estimation error in the augmented system using the estimator derived in the balanced case is given by

$$\begin{aligned}\left[\frac{e_1^{\mathrm{p}}}{e_1^{\mathrm{q}}}\right] = &\left(\Delta W_1^{\mathrm{m}} - W_1^{\mathrm{m}}(W_{\mathrm{vsd}}^{\mathrm{m}})^{-1}\Delta W_{\mathrm{vsd}}^{\mathrm{m}}\right)\left[\frac{\Delta I^{\mathrm{pdcm}}}{\Delta I^{\mathrm{qdcm}}}\right] \\ &+ \left(W_1^{\mathrm{x}} - W_1^{\mathrm{m}}(W_{\mathrm{vsd}}^{\mathrm{m}})^{-1}W_{\mathrm{vsd}}^{\mathrm{x}}\right)\left[\frac{I^{\mathrm{pdcx}}}{I^{\mathrm{qdcx}}}\right] \\ &+ \left(\Delta W_1^{\mathrm{x}} - W_1^{\mathrm{m}}(W_{\mathrm{vsd}}^{\mathrm{m}})^{-1}\Delta W_{\mathrm{vsd}}^{\mathrm{x}}\right)\left[\frac{\Delta I^{\mathrm{pdcx}}}{\Delta I^{\mathrm{qdcx}}}\right].\end{aligned} \tag{3.38}$$

Additional harmonics can be used to minimize the second error term, specifically $(W_1^{\mathrm{x}} - W_1^{\mathrm{m}}(W_{\mathrm{vsd}}^{\mathrm{m}})^{-1}W_{\mathrm{vsd}}^{\mathrm{x}})\ [I^{\mathrm{pdcx}},\ I^{\mathrm{qdcx}}]^T$. The error correction factor is given as

$$T_1^x = \left((W_{\mathrm{x}}^{\mathrm{x}}(W_{\mathrm{x}}^{\mathrm{x}})^T)^{-1}(W_{\mathrm{x}}^{\mathrm{x}}(W_1^{\mathrm{x}} - W_1^{\mathrm{m}}(W_{\mathrm{vsd}}^{\mathrm{m}})^{-1}W_{\mathrm{vsd}}^{\mathrm{x}})^T)\right)^T. \tag{3.39}$$

The final estimating function is given by

$$\left[\frac{\widehat{I}_{\mathrm{vsd1}}^{\mathrm{p}}}{\widehat{I}_{\mathrm{vsd1}}^{\mathrm{q}}}\right] = W_1^{\mathrm{m}}(W_{\mathrm{vsd}}^{\mathrm{m}})^{-1}\left[\frac{I_{\mathrm{vsd}}^{\mathrm{p}}}{I_{\mathrm{vsd}}^{\mathrm{q}}}\right] + T_1^x\left[\frac{I_{\mathrm{x}}^{\mathrm{p}}}{I_{\mathrm{x}}^{\mathrm{q}}}\right]. \tag{3.40}$$

Equation (3.40) provides a closed-form solution for estimating the fundamental har-

monic current consumed by a three-phase rectifier from higher harmonic currents. The estimator is linear and simple to compute. In addition, the algorithm does not require any prior knowledge of system parameters. The algorithm can be modified to use other sets of harmonics by changing the coefficient matrices.

### 3.5.3 Estimator Coefficients

Assuming the ideal switching function shown in Figure 3.11, the coefficients of the VSD estimator based on the equation (3.40) are given by

$$\begin{bmatrix} \widehat{I}^{\mathrm{p}}_{\mathrm{vsd1}} \\ \hline \widehat{I}^{\mathrm{q}}_{\mathrm{vsd1}} \end{bmatrix} = \left[\begin{array}{ccc|ccc} -3.269 & -2.879 & -0.716 & 0.000 & 0.000 & 0.000 \\ \hline 0.000 & 0.000 & 0.000 & 0.189 & -0.093 & 0.061 \end{array}\right] \begin{bmatrix} I^{\mathrm{p}}_5 \\ I^{\mathrm{p}}_7 \\ I^{\mathrm{p}}_{11} \\ \hline I^{\mathrm{q}}_5 \\ I^{\mathrm{q}}_7 \\ I^{\mathrm{q}}_{11} \end{bmatrix}$$
$$+ \left[\begin{array}{cc|cc} -2.632 & -1.817 & 0.000 & 0.000 \\ \hline 0.000 & 0.000 & -0.850 & -0.152 \end{array}\right] \begin{bmatrix} I^{\mathrm{p}}_3 \\ I^{\mathrm{p}}_9 \\ \hline I^{\mathrm{q}}_3 \\ I^{\mathrm{q}}_9 \end{bmatrix}. \tag{3.41}$$

Because of the ideal switching function is used to compute the coefficients, the in-phase and quadratures components are decoupled from each other. Furthermore, the triplen harmonics are decoupled from the other harmonics as well. In this case, the triplen harmonics can be used if the system becomes unbalanced and the VSD actually consumes the triplen harmonics. On the contrary, the balanced three phase system should contain no triplen harmonic and the coefficients for the triplen harmonics can be ignored.

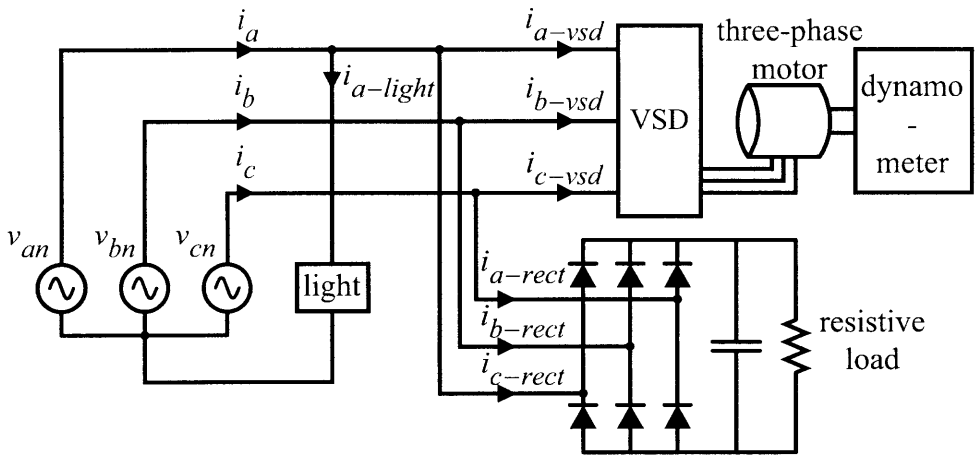


Figure 3.16: Experimental setup

## 3.6 Results and Discussion

This section demonstrates the ability of the model-based VSD power estimator to resolve the power consumption of VSD and rectifier loads from other constant power loads. The experimental setup consisted of a controllable three-phase voltage source and three electronic loads: a VSD system connected to a dynamometer, a 200-W three-phase rectifier load, and a 50-W light bulb connected between phase-A and neutral. The experimental setup is shown in Figure 3.16.

In the following experiments, the model-based estimator used three in-phase and three quadrature components of ac-side harmonics, specifically, $I^{\mathrm{p}}_{\mathrm{vsd}} = [I^{\mathrm{p}}_5, I^{\mathrm{p}}_7, I^{\mathrm{p}}_{11}]^T$ and $I^{\mathrm{q}}_{\mathrm{vsd}} = [I^{\mathrm{q}}_5, I^{\mathrm{q}}_7, I^{\mathrm{q}}_{11}]^T$.In addition, the third and ninth harmonics were used for the error correction factor, $I^{\mathrm{p}}_{\mathrm{x}} = [I^{\mathrm{p}}_3, I^{\mathrm{p}}_9]^T$ and $I^{\mathrm{p}}_{\mathrm{x}} = [I^{\mathrm{q}}_3, I^{\mathrm{q}}_9]^T$. The real power consumed by the VSD and the rectifier was calculated together using (3.5). The light bulb fundamental real power was calculated by

$$P_{\mathrm{light}} = V^{\mathrm{a}}_1 (I^{\mathrm{p}}_1 - \widehat{I}^{\mathrm{p}}_{\mathrm{vsd1}}) \tag{3.42}$$

where $V^{\mathrm{a}}_1$ was the amplitude of the fundamental line-to-neutral voltage and $\widehat{I}^{\mathrm{p}}_{\mathrm{vsd1}}$ represents the estimated fundamental current harmonic consumed by the VSD in

phase-A. The coefficients were recomputed every thirty line cycles to correct for any change in the input voltage.

### 3.6.1 Balanced Input Voltage Cases

First, the model-based VSD power estimator was tested under a balanced input voltage case. This input voltage was used to generate the correlation function for the empirically-based estimator. The goal of this test is to demonstrate the ability of the model-based estimator to extract the power consumed by both the VSD and the rectifier from the 50-W light bulb during a sequence of load operations. Experimental results are shown in Figure 3.17. Clearly that the model-based estimator can resolve the power consumption of the VSD and the rectifier successfully when the input voltage is balanced. Small errors can be noticed during the light bulb start-up transient because the sharp transient contains higher current harmonics that are used as input variables to the VSD estimator. A more complex method may be applied to minimize the estimation error during transient events caused by other loads. On the other hand, the estimated light bulb power using the empirically-based estimator is shown in Figure 3.18. The experimental result shown in Figure 3.18 confirms that the empirically-based estimator could produce an estimation error during the rectifier load operation.

### 3.6.2 Distorted input voltage cases

To measure the performance of the proposed estimator under input voltage variation, different levels of input voltage distortion were imposed during the experiments to compare performance between the empirically-based and the model-based estimators. In these tests, the VSD was running with constant load and the input voltage was distorted by different amounts of fifth or seventh harmonic in all three phases. The performance is measured by the percentage error of the estimated VSD real power

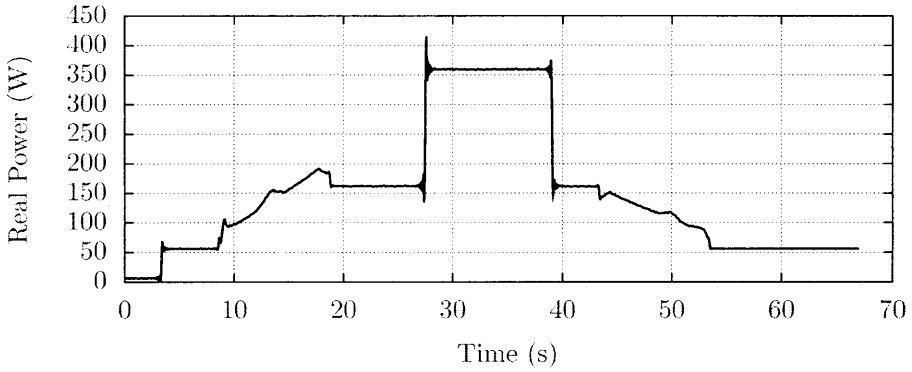


(a) Total power of VSD, rectifier, and light bulb

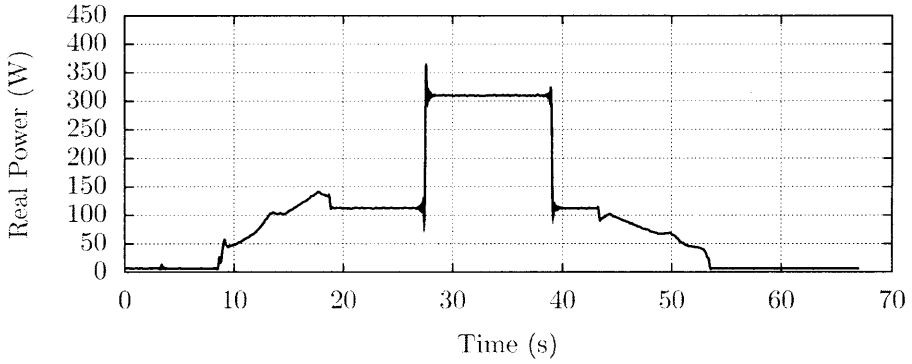


(b) Extracted real power consumption of VSD and rectifier

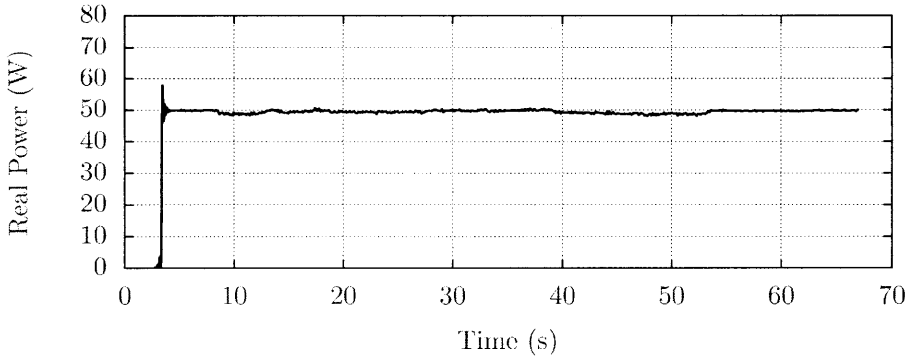


(c) Extracted real power consumption of the incandescent light bulb

Figure 3.17: Experimental results of the VSD power estimator resolving the power consumption of VSD and rectifier from the 50-W incandescent light bulb under balanced input voltages. The aggregated measurement of the real power consumption of VSD, rectifier, and light bulb in (a). The extracted real power consumption of the VSD and three-phase rectifier is shown in (b). Finally, the extracted real power consumption of the incandescent light bulb is shown in (c).

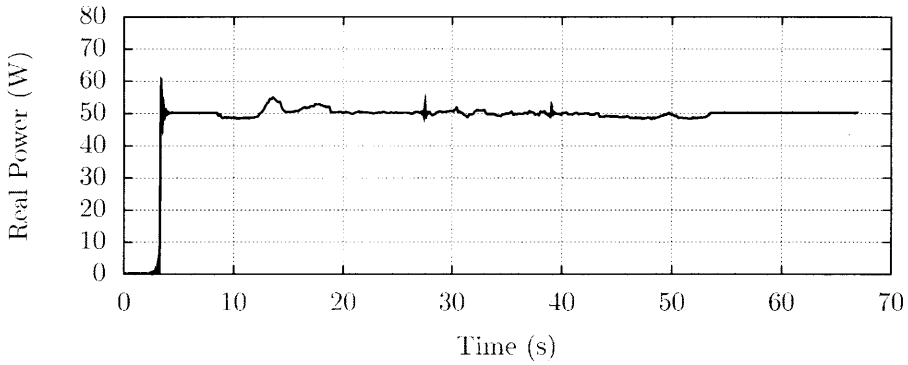


Figure 3.18: Experimental result showing the estimated power of the 50-W light bulb after the empirically-based estimator has removed power of the VSD and the rectifier under the balanced input voltages

consumption, specifically

$$\text{estimation error}\,(\%) = \frac{|P_{vsd} - \widehat{P}_{vsd}|}{P_{vsd}} \times 100. \tag{3.43}$$

Experimental results are shown in Figure 3.19 and 3.20. These experimental results demonstrate that the model-based algorithm is robust against input voltage distortion across a wide load range. This improvement confirms that the approximation made during the derivation is valid for small voltage distortions that are likely to occur in the field.

Moreover, if the more accurate result is required, the algorithm can be adapted to use more line-side harmonics in the input vectors $I^{\mathrm{p}}_{\mathrm{vsd}}$ and $I^{\mathrm{q}}_{\mathrm{vsd}}$. For example, $I^{\mathrm{p}}_{\mathrm{vsd}}$ can contain four harmonics such as $I^{\mathrm{p}}_{\mathrm{vsd}} = [I^{\mathrm{p}}_5, I^{\mathrm{p}}_7, I^{\mathrm{p}}_{11}, I^{\mathrm{p}}_{13}]^T$. Similarly, the quadrature component can be $I^{\mathrm{q}}_{\mathrm{vsd}} = [I^{\mathrm{q}}_5, I^{\mathrm{q}}_7, I^{\mathrm{q}}_{11}, I^{\mathrm{q}}_{13}]^T$. In this case, the estimator errors in the case of voltage distortion are shown in Figure 3.21.

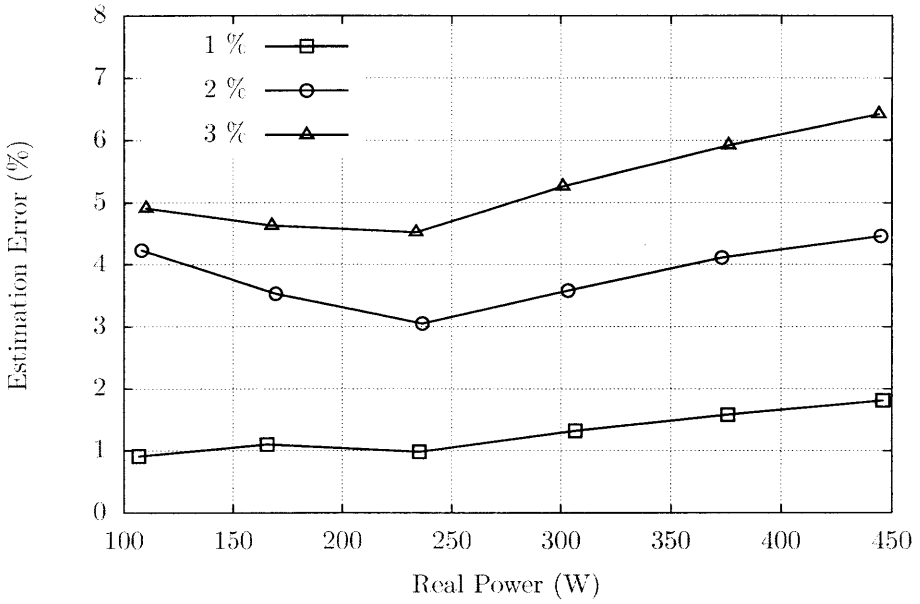


(a) Empirically-based estimator

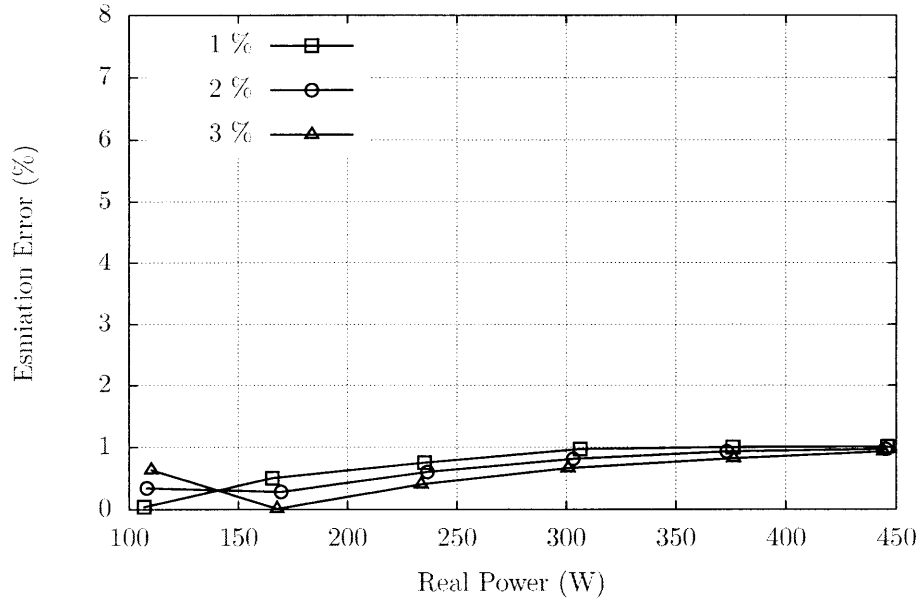


(b) Model-based estimator

Figure 3.19: Experimental results showing the estimation errors in the VSD real power prediction using when the input voltages are distorted with different levels of fifth harmonic. The estimation errors using the empirically-based estimator are shown in (a). The estimation errors using the model-based estimator are shown in (b).

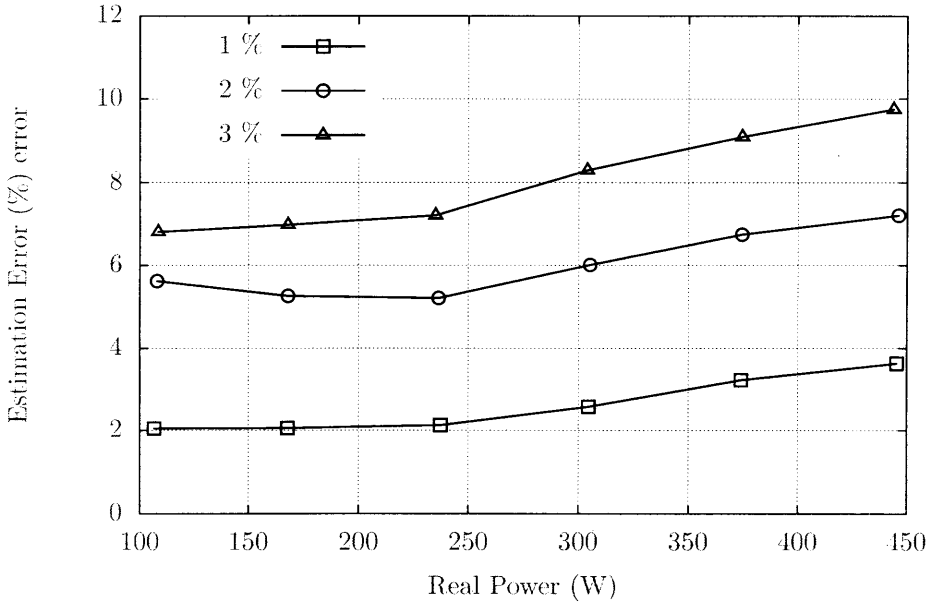


(a) Empirically-based estimator

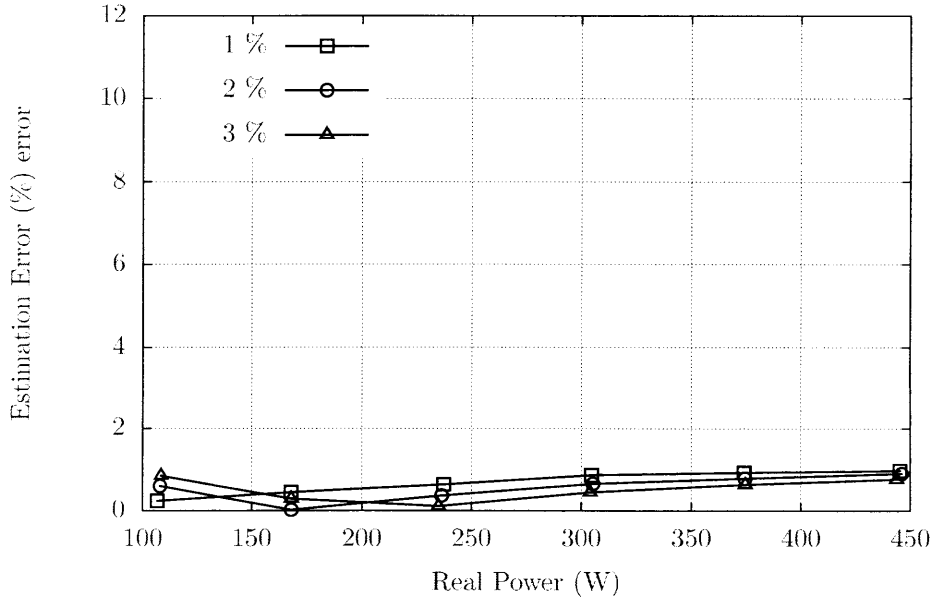


(b) Model-based estimator

Figure 3.20: Experimental results showing the estimation errors in the VSD real power prediction using when the input voltages are distorted with different levels of seventh harmonic. The estimation errors using the empirically-based estimator are shown in (a). The estimation errors using the model-based estimator are shown in (b).

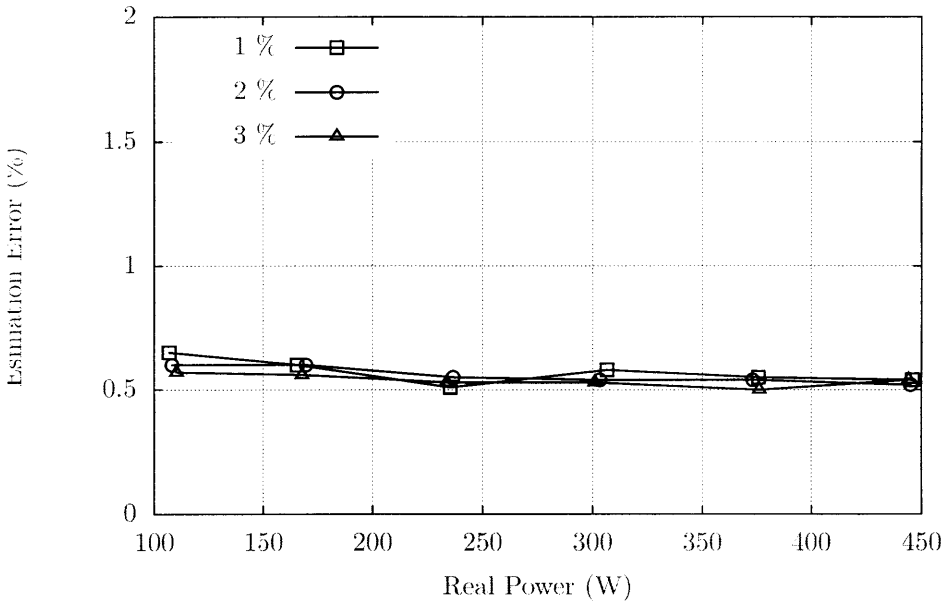


(a) Fifth harmonic voltage distortion

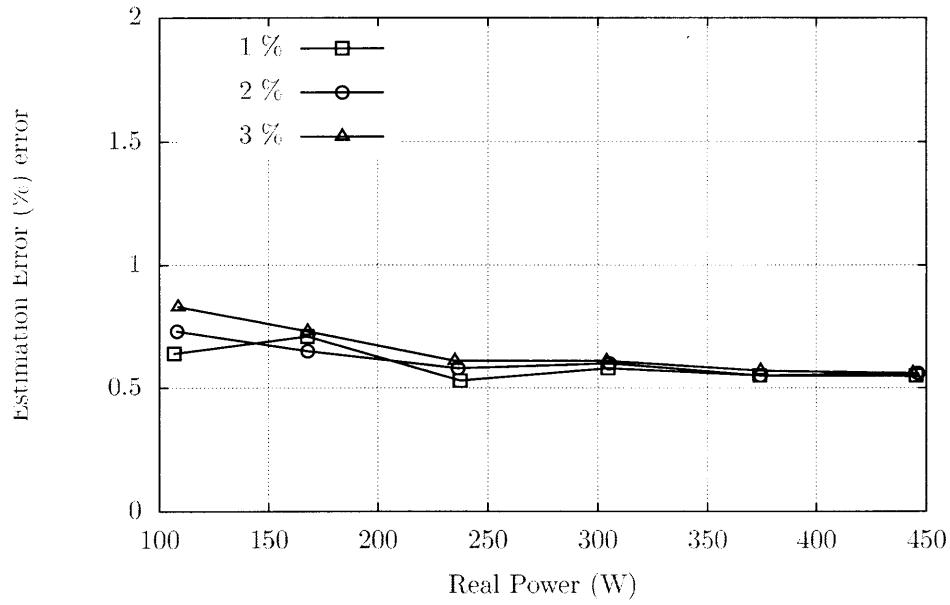


(b) Seventh harmonic voltage distortion

Figure 3.21: Experimental results showing the estimation errors in the VSD real power prediction using the model-based estimator with four input harmonics. The estimation errors when the input voltages are distorted with different levels of the fifth harmonic voltage are shown in (a). The estimation errors when the input voltages are distorted with different levels of the seven harmonic voltage are shown in (b).

## 3.7 Summary

By using the switching function to as a basis to derive the functional relationship between higher harmonics and the fundamental harmonic of the three-phase rectifier of the VSD, the estimator can be generated prior to the installation of the NILM system. The method has shown promising results to disaggregate this VSD non-linear load from the linear load. The algorithm allows a user to trade between the estimation accuracy and the computational complexity. Furthermore, this method could be adapted for other non-linear load that can be described by the switching function.

*Chapter 4*

# *Waveform-Based Estimator*

## 4.1 Introduction

This chapter introduces a new method for estimating the real and reactive power consumed by a continuously variable load such as a variable speed drive (VSD) operating in a collection of electrical loads. This method estimates the power consumption of the variable load given only aggregate measurements of current. The proposed method exploits structural features of the non-sinusoidal current waveform consumed by many variable power loads. This method is distinct in requiring no internal circuit model or description of the variable load to derive the estimator.

The application of power electronics enables many loads to operate over a wide variable power range. Examples of variable power loads are variable speed drives (VSDs), computers, and light dimmers. These continuously variable power loads do not have a unique power consumption pattern. Therefore, these loads cannot necessarily be tracked for energy consumption strictly by examining turn-on and turn-off transients. These loads, e.g. a VSD, may consume harmonic currents such as the fifth and seventh harmonics. At a particular site, these harmonics may be uniquely associated with the VSD and can be used to estimate the fundamental current harmonic and the power consumption of the VSD accurately using a data-driven model [12]. This estimator monitors the operation of the VSD and generates the correlation function between the harmonic current and the power consumption. However, the correlation function is sensitive to changes in the environment such as input voltage harmonics [17]. As a result, an alternative estimator was developed by

modeling and analyzing the behavior of the internal circuit of the VSD, specifically the uncontrolled three-phase rectifier [17]. The model-based estimator solves the issue of the input voltage distortions, enhancing the robustness of the estimator. However, other loads may be too complex to model and analyze, and the internal circuit diagram may not be available. Therefore, the application of the model-based estimator may not be possible.

Although these variable power loads consume different harmonic currents, there are common characteristics in the current among these loads. These variable power loads are not linear time invariant (LTI) because their currents are modulated by the power electronic operation. Their currents are non-sinusoidal. However, the current waveforms of these variable power loads consist of structural features that can be identified in both the time and frequency domains. For example, the VSD and computer waveforms have known regions of zero current. Furthermore, the sampled current signal is also band-limited and periodic. These observable characteristics of the current waveforms can be used to write linear constraints according to the Fourier analysis and synthesis equations. These constraints can be manipulated using a standard Gaussian elimination method to achieve a functional relationship between the fundamental current harmonic and higher harmonics uniquely associated with the load. The estimator can be computed without fully analyzing the underlying circuit of the load. In addition, the actual computation can be done using a cyclotomic field representation to minimize numerical error. The "closed" property of the cyclotomic field allows an accurate arithmetic computation [19, 44–46].

This chapter describes a systematic process to derive a waveform-based estimator. The first section gives an overview of the NILM system. The section also explains the implication of the Fourier analysis and synthesis equations on the functional relationship between different current harmonics. The estimator derivation is explained as a four-step process in the next section. In addition, the chapter also describes the use of a cyclotomic field representation in the algorithm implementation

for computational accuracy. Finally, experimental results are included to demonstrate the extraction of the power consumptions of continuously variable power loads such as VSDs, computers, and light dimmers from a fixed power load using the proposed waveform-based estimator.

## 4.2 Background

As mentioned in the previous chapter, a VSD represents one of a class of loads that draws a distorted current waveform containing high harmonic content. Other common appliances also draw non-sinusoidal current waveforms as well. These appliances can be designed to deliver different power levels depending on a specific control algorithm and external settings. Variable loads adjust the amount of power consumed, potentially continuously. These continuously variable power loads present the same monitoring issues as the VSD does. Specifically, the continuously varying loads do not have a unique power consumption "signature" for the NILM system to identify. Furthermore, these variable power loads corrupt the power "signatures" of other loads in the aggregate measurements.

Current waveforms and Fourier coefficients of these loads are shown in Figures 4.1, 4.2, and 4.3. The simulated VSD current waveforms are shown in Figures 4.1a and 4.1b for comparison. These simulated waveforms depict the VSD current waveforms over one line voltage cycle. The normalized harmonic currents of the VSD current waveforms are shown in Figures 4.1c and 4.1d. These examples of normalized harmonic currents show the harmonic distribution of the VSD current. Current waveforms of a computer power supply operating at two power levels are shown in Figures 4.2a and 4.2b. The normalized harmonic currents of the computer current waveforms are shown in Figures 4.2c and 4.2d. Finally, current waveforms of the light dimmer at two brightness settings are shown in Figures 4.3a and 4.3b. The corresponding normalized harmonic currents of the light dimmer current wave-

forms are shown in Figures 4.3c and 4.3d. The light dimmer used in this experiment has fixed number of brightness levels. However, different manufacturers may allow continuous dimming operation. As a result, these waveforms can vary continuously making the identification and tracking tasks more challenging.

In the NILM applications, multiple loads are monitored together in the aggregate current measurements, i.e.

$$i_{\text{measured}}(t) = \sum_{j=1}^{L} i_j(t), \tag{4.1}$$

where the variable $i_j(t)$ represents the current consumed by the $j$th load. The NILM system can detect and track a collection of loads that consume a finite number of power levels [5]. Given a variable power load, the NILM system is interested in using information about the current harmonics of the new load to distinguish this new load from other known loads. Specifically, the system is expected to extract the fundamental current of each load for identification and monitoring purposes. Mathematically, the desired estimator can be described as

$$\widehat{I_1} = f\left(I_{m_1}, I_{m_2}, I_{m_3}, \dots\right), \tag{4.2}$$

where the variable $\widehat{I_1}$ represents the estimated fundamental harmonic current consumed by the load. The variables $I_{m_1}$, $I_{m_2}$, and $I_{m_3}$ represent the input harmonics, which are higher harmonics uniquely consumed by the load. The estimating function $f(\,)$ maps between higher harmonics to the fundamental harmonic. The function $f(\,)$ can take many input harmonics depending on the derivation method. The ideal estimating function should use the fewest number of inputs to compute the fundamental harmonic current, which can benefit the load disaggregation and diagnostics. A lower number of input harmonics used in the estimating function allows the NILM to use other harmonics for other purposes and possibly save the computational cost in the

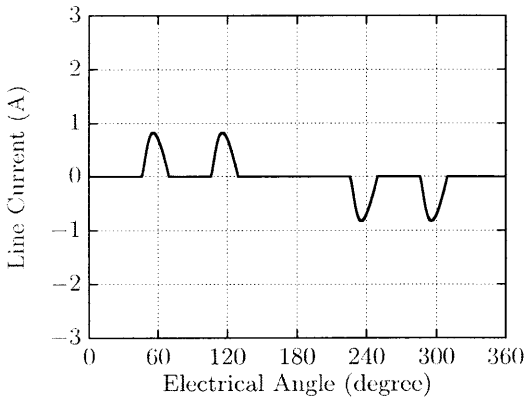


(a) Line current in a light load condition

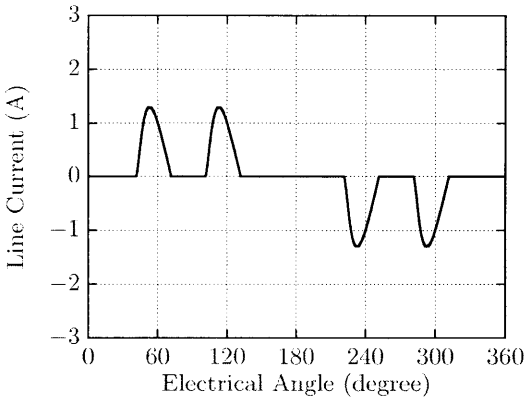


(b) Line current in a heavier load condition

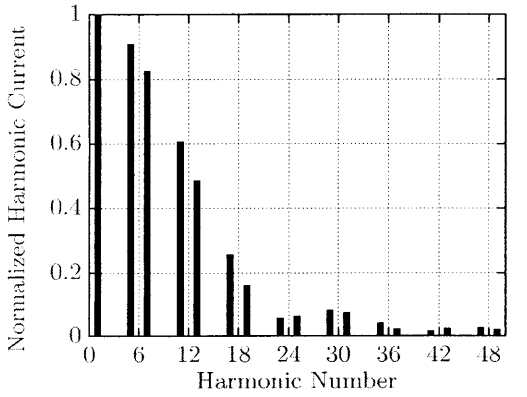


(c) Normalized harmonic currents in a light load condition

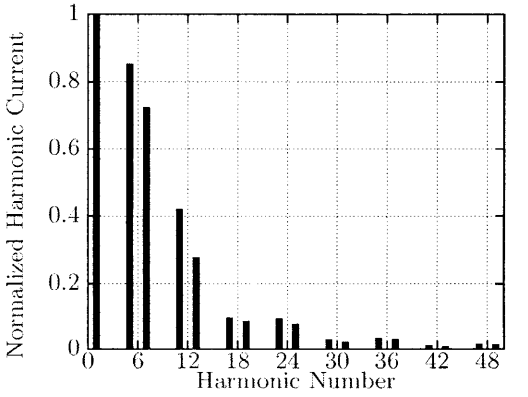


(d) Normalized harmonic currents in a heavier load condition

Figure 4.1: Simulated current waveforms and normalized harmonic currents of a variable speed drive. The line current of the VSD operating in a light load region is shown in (a). The line current of the VSD operating in a heavier load region is shown in (b). The corresponding normalized harmonic currents of the VSD operating in a light load region are shown in (c). The corresponding normalized harmonic currents of the VSD operating in a heavier load region are shown in (d).

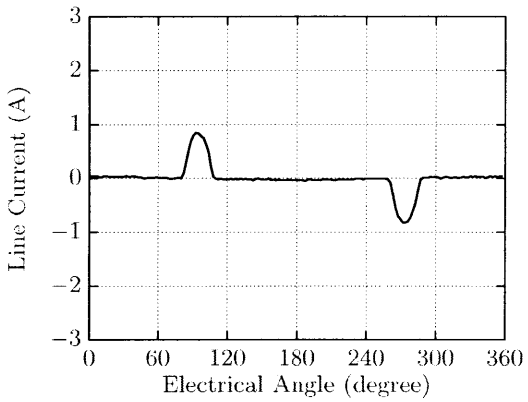


(a) Line current in a low power condition

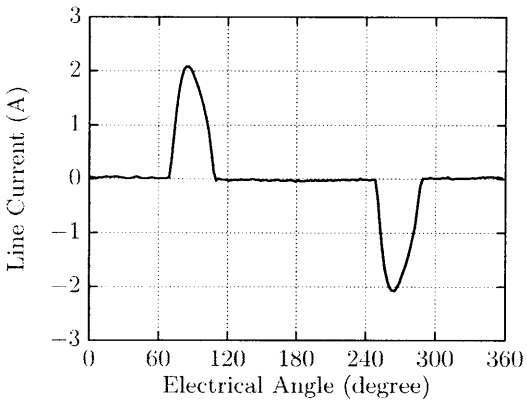


(b) Line current in a higher power condition

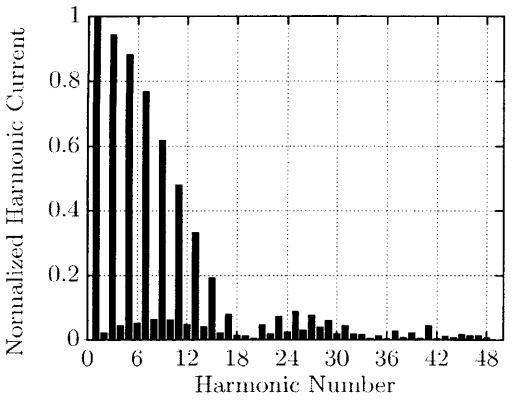


(c) Normalized harmonic currents in a low power condition

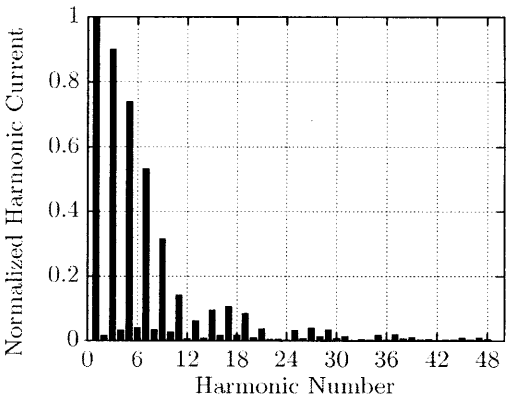


(d) Normalized harmonic currents in a higher power condition

Figure 4.2: Experimental current waveforms and normalized harmonic currents of a computer. The line current of the computer operating with a low power condition is shown in (a). The line current of the computer operating with a higher power condition is shown in (b). The corresponding normalized harmonic currents of the computer operating in a low power condition are shown in (c). The corresponding normalized harmonic currents of the computer operating in a higher power condition are shown in (d).

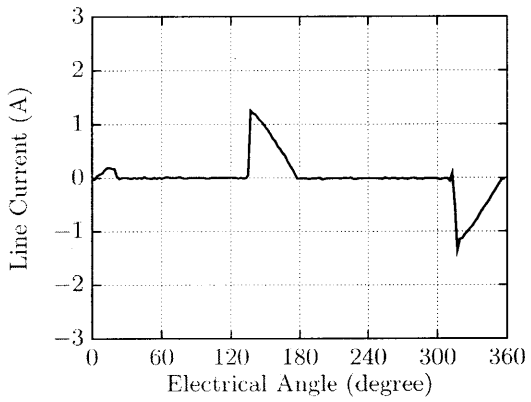


(a) Line current in a low brightness condition

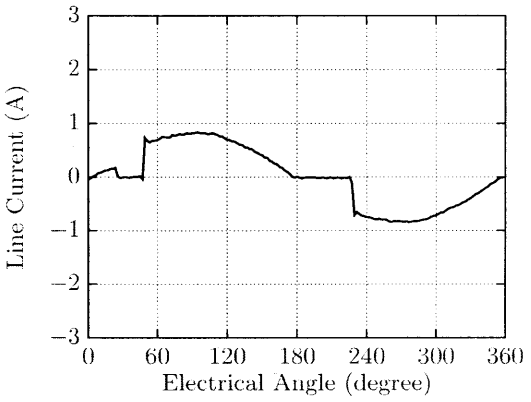


(b) Line current in a high brightness condition

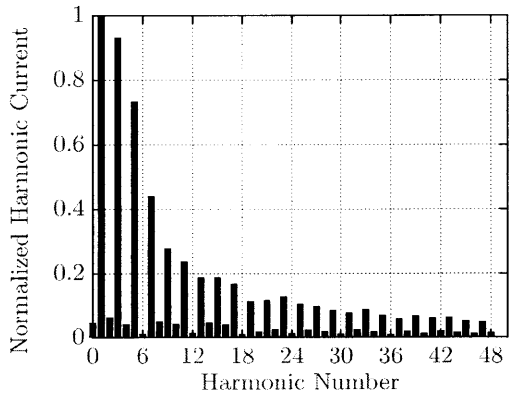


(c) Normalized harmonic currents in a low brightness condition

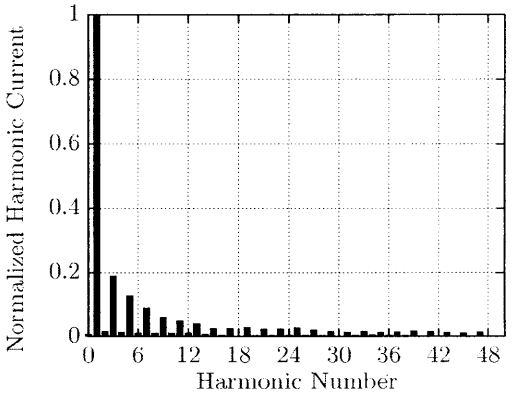


(d) Normalized harmonic currents in a high brightness condition

Figure 4.3: Experimental current waveforms and normalized harmonic currents of an incandescent light dimmer. The line current of the light dimmer operating in a low brightness setting is shown in (a). The line current of the light dimmer operating in a high brightness setting is shown in (b). The normalized harmonic currents of the light dimmer operating in a low brightness setting are shown in (c). The normalized harmonic currents of the light dimmer operating in a high brightness setting are shown in (d).

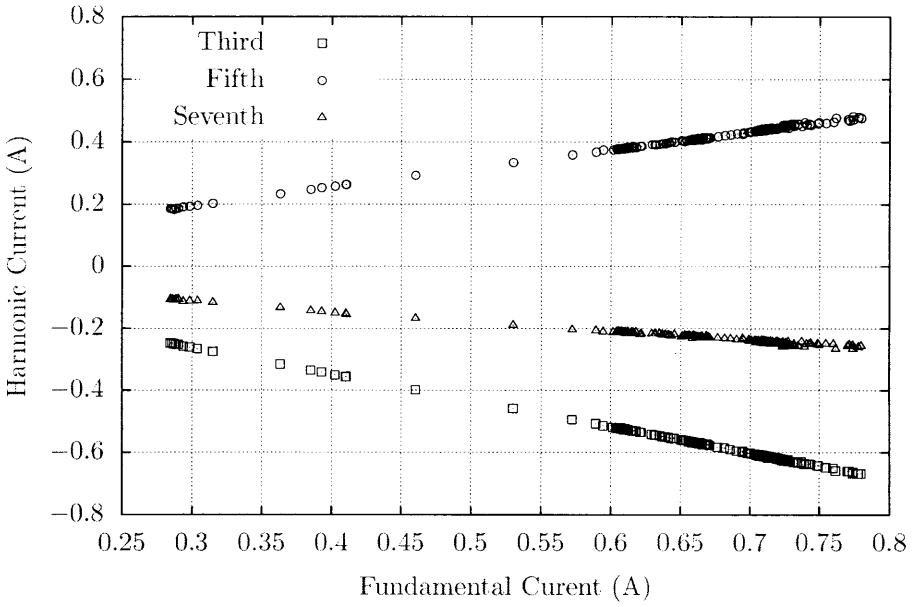


Figure 4.4: Scatter plots between the fundamental current and harmonic currents of the measured computer current

real-time estimation.

A direct inspection of the waveforms of variable power loads in Figure 4.1 permits identification of the variable power load when the load is running by itself. However, it is more difficult to identify and extract these loads in the aggregate measurements. Some variable power loads consume a spectrum of harmonic currents that can be used to track each load using simple correlation functions. Figure 4.4 shows scatter plots between the fundamental and higher harmonics of the computer measured in the experiments. The scatter plot depicts a strong correlation function between the fundamental and the higher harmonic. Therefore, the NILM may use a curve-fitting method to compute the estimating function as described in [12].

On the other hand, the light dimmer consumes both real and reactive power. It also draws higher harmonic currents as well. Figure 4.5 depicts the real and reactive power consumed by the light dimmer over a full operating range. Figure 4.6 shows the scatter plots between the fundamental harmonic and higher harmonic currents.

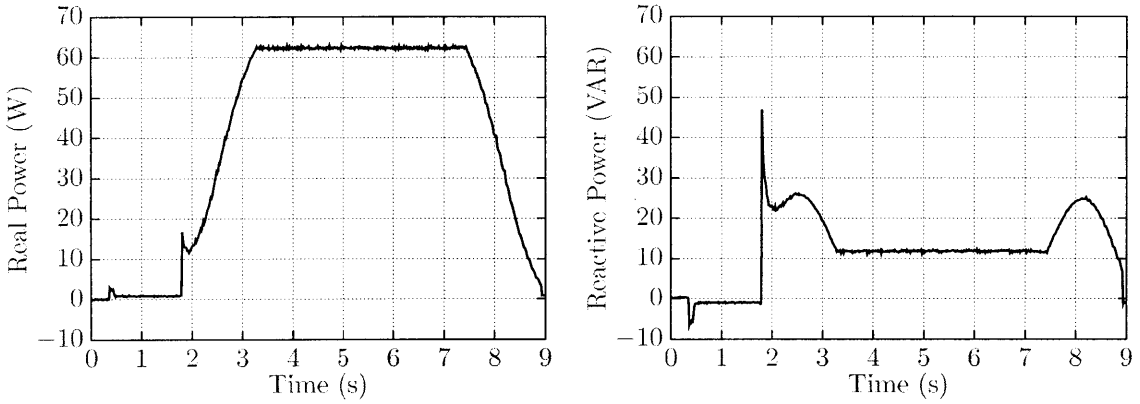


(a) Real power (b) Reactive power

Figure 4.5: Real and reactive power consumed by the light dimmer from the experimental results

The scatter plots in Figure 4.6 suggest that there is no obvious one-to-one function between the fundamental and any particular harmonic current.

Furthermore, the aggregate current measurements of multiple variable loads can vary significantly, making the identification task even more difficult. Figure 4.7 depicts the measured current waveforms of multiple variable power loads. If a new load has finite number of settings, the recognition by pattern matching could be done for all conceivable settings allowed by combinations of all loads. The task can be a tedious but viable solution. However, the task becomes less attractive when the power consumption varies in a continuous fashion such as VSDs, computers and light dimmers. In these cases, a finite set of solutions may not be possible. The estimator for multiple variable loads presents another challenging task. The extraction of variable power loads has been a long standing problem of load recognition, which is yet to be addressed successfully. Currently, there is no systematic way to derive the power estimator for variable power loads. This chapter focuses only extracting one class of variable power loads from a group of discrete power loads. However, the concept can be applied to extracting the power consumption of multiple variable loads together as a group from the power consumption of the discrete power loads.

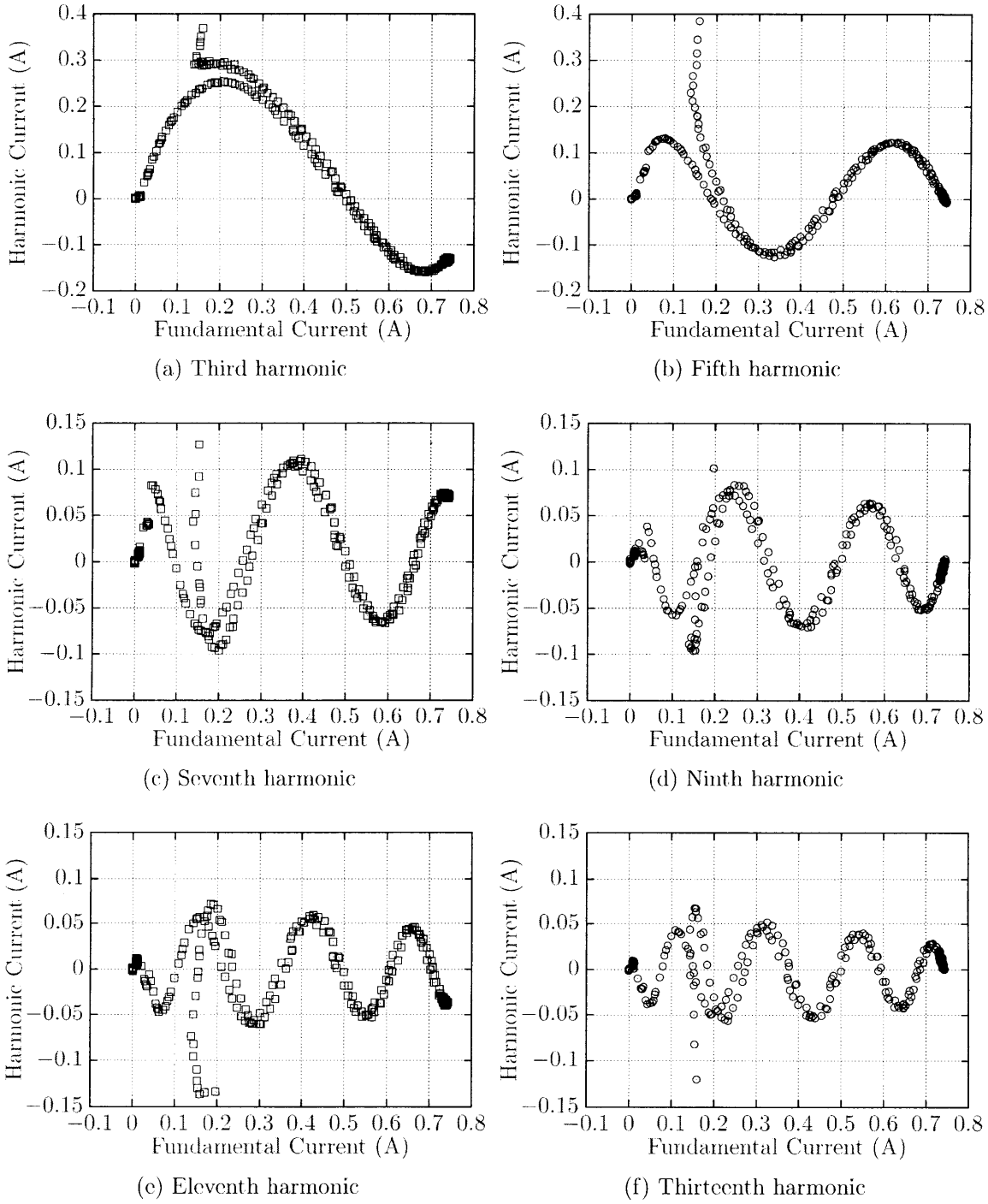


(a) Third harmonic

(b) Fifth harmonic

(c) Seventh harmonic

(d) Ninth harmonic

(e) Eleventh harmonic

(f) Thirteenth harmonic

Figure 4.6: Correlation functions between the fundamental harmonic and higher harmonics of the light dimmer across the entire operating range.

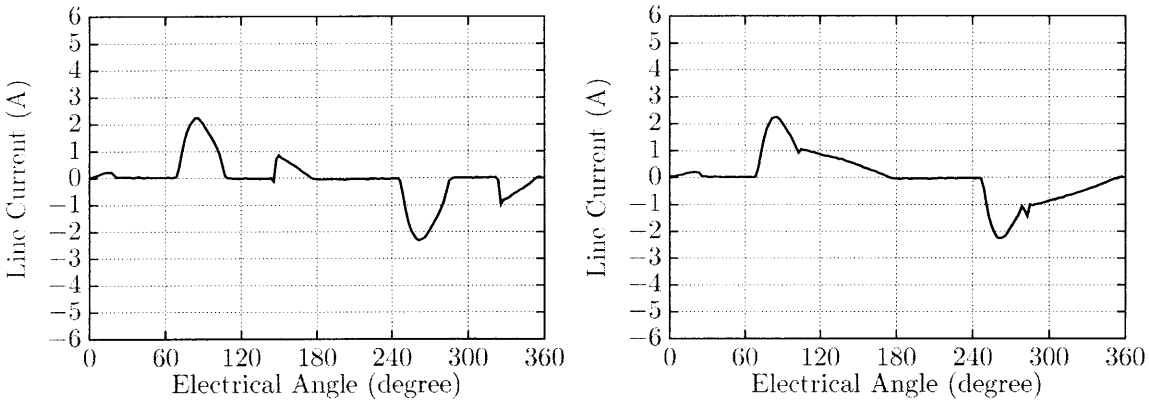


(a) Computer and light dimmer I

(b) Computer and light dimmer II

(c) Light, computer, and light dimmer I

(d) Light, computer, and light dimmer II

(e) Light, computer, and light dimmer III

(f) Light, computer, and light dimmer IV

Figure 4.7: Current waveforms of multiple variable power loads

A variable power load such as a VSD can be tracked by using a functional relationship between the fundamental current harmonic and the higher current harmonics uniquely associated with the VSD [12, 17]. The empirical-based estimator cannot account for the input voltage variation [17]. On the other hand, the model-based estimator is derived by analyzing the internal circuit and the behavior of the load, which may not be available [17]. The application of the model-based estimator may not be possible for other variable power loads. Instead of fully analyzing the internal circuit diagrams for each new load, it can be noticed that some variable power loads share a few common features that can be identified and recognized such as presence of zero-current regions and waveform symmetry. Current waveforms and discrete Fourier transform (DFT) coefficients of the current waveform for a VSD, a computer, and a light dimmer are shown in Figures. 4.1, 4.2, and 4.3 respectively. The next sections explain the concept of the waveform-based estimator, which exploits the structural features of the non-sinusoidal current waveform to derive the estimating function (4.2).

## 4.3 Waveform-Based Estimator

Different variable power loads use different circuit topologies and control methods. Instead of fully analyzing the internal circuits in detail, which may not be possible, the current waveforms contain unique information about the load. This information is embedded in the structural features of the current waveform that can be exploited by the proposed waveform-based estimator. This section focuses on deriving the estimator by only analyzing the structural features of the waveform. The current waveforms of these variable power loads shown in Figures 4.1, 4.2, and 4.3 share a few common properties that can be observed and analyzed. Those properties include five waveform constraints:

- periodicity,

- presence of zero-current regions,
- waveform symmetry and harmonic constraints,
- approximately band-limited signal, and
- real-valued signal.

These five structural features can be used to distinguish these variable power loads from other loads in aggregate current measurements available to the NILM.

These five waveform constraints can be translated to mathematical forms using the Fourier analysis and synthesis equations [47]. Given a band-limited and periodic signal, the sampled waveform can be described by a weighted sum of discrete Fourier transform (DFT) coefficients $I_k$ as

$$i[n] = \sum_{k=0}^{N-1} I_k e^{j\frac{2\pi}{N}(kn)}, \tag{4.3}$$

where the variable $n$ is the time index, ranging from 0 to $N-1$. The number $N$ represents a number of samples per signal period. The DFT coefficients $I_k$ are calculated by the Fourier analysis equation,

$$I_k = \frac{1}{N} \sum_{n=0}^{N-1} i[n] e^{-j\frac{2\pi}{N}(kn)}. \tag{4.4}$$

where the subscript $k$ represents the harmonic, ranging from 0 to $N-1$. The scaling factor $\frac{1}{N}$ normalizes the coefficients by the data length. The relationship in (4.3) illustrates the form of the functional relationship among different harmonics and the time-domain current waveform. If all $N$ samples of the current waveform are known, the Fourier synthesis equation (4.3) provides all constraints between different current harmonics $I_k$ and the time-domain signal $i[n]$. However, only a limited number of equations can be used to constraints the functional relationship between different

current harmonics. The proposed estimator uses the available number of constraints to obtain the estimator for the variable power load. The next section explains the systematic procedure to translate the five waveform features into the mathematical constraints, that can be manipulated into the desired estimator.

## 4.4 Estimator Derivation

The goal is to compute a functional relationship between the fundamental harmonic, $I_1$ and higher harmonics as described in (4.2). In the previous section, the Fourier synthesis equation (4.3) has suggested the form of the estimating function. Specifically, this proposed method is looking for the estimating function in a linear form as

$$\widehat{I_1} = \sum_{m=1}^{2K} (c_m I_m), \tag{4.5}$$

where $\widehat{I_1}$ is the estimated fundamental harmonic, and the coefficient $c_m$ represents a coefficient, which can be complex. The variable $I_m$ represents a selected higher harmonic or a chosen input harmonic uniquely associated with the variable power load. The number $2K$ represents the number of input harmonics used in the estimator. The variable $K$ indicates the number of input harmonic pairs. The selection of the input harmonics is described in the next sections. Ultimately, the method seeks an estimator that predicts the fundamental harmonic, $\widehat{I_1}$, given observations of higher harmonics that are uniquely or largely associated with a variable power load at a target site.

The estimator can be developed iteratively with a four-step process:

1. identify signal constraints,

2. setup a Fourier matrix equation,

3. solve for the estimator, and

4. evaluate estimation error.

The first step describes how to translate the five waveform features to linear constraints described in the Fourier synthesis equation (4.3). The first step also explains the selection of the input harmonics used in the estimator. The second step establishes a Fourier matrix equation from the listed constraints. The next step demonstrates how to reduce the matrix equation into the candidate estimator equation. Finally, the derived estimator is evaluated and tested against accuracy requirements in the fourth step. The procedure can be iterated to further improve the estimation error or reduce the number of input harmonics.

### 4.4.1 Signal Constraints

Given an input current signal, the observations in the list of five waveform constraints can be expressed mathematically using the Fourier synthesis equation (4.3). First, the current signal is assumed to be periodic with a period of $T$. In the ac system, the period is a reciprocal of line voltage frequency. The periodic signal is sampled and analyzed using the discrete Fourier transform to obtain the DFT coefficients or current harmonics $I_k$ according to the Fourier analysis equation (4.4). The signal is assumed to be sampled at the rate $F_s$ such that the sampled signal consists of $N$ points per period. Given, $N$ samples per period, there are $N$ DFT coefficients from the Fourier analysis equation (4.4).

Second, the current waveform consists of known regions of zero-current because of the circuit operation. Examples of the input voltage and the current waveform of the VSD operated in a discontinuous conduction mode (DCM) are shown in Figure 4.8. In the case of a VSD, the consumed current has known zero-current regions shown in Figure 4.8, which can be expressed mathematically based on electrical angle

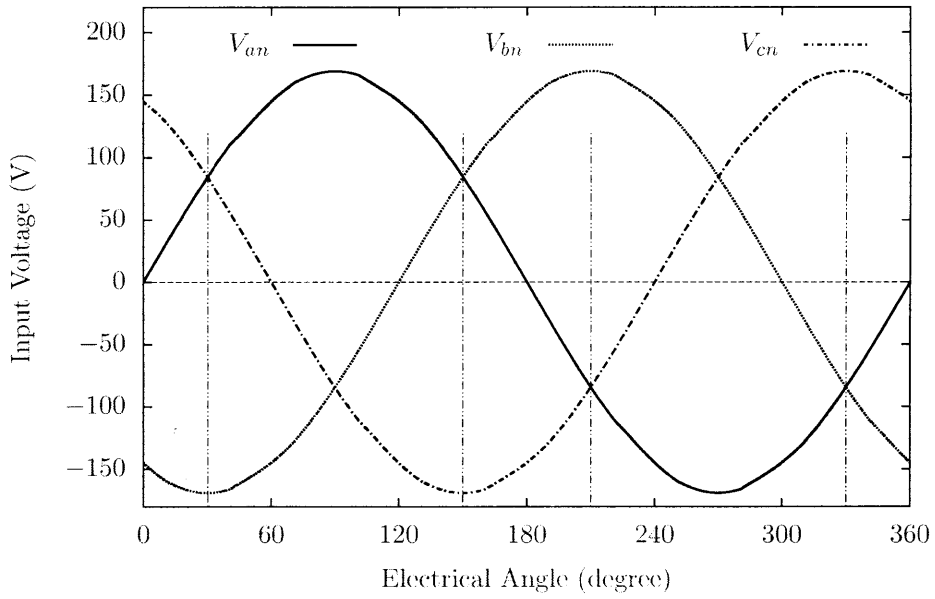


(a) Line voltages

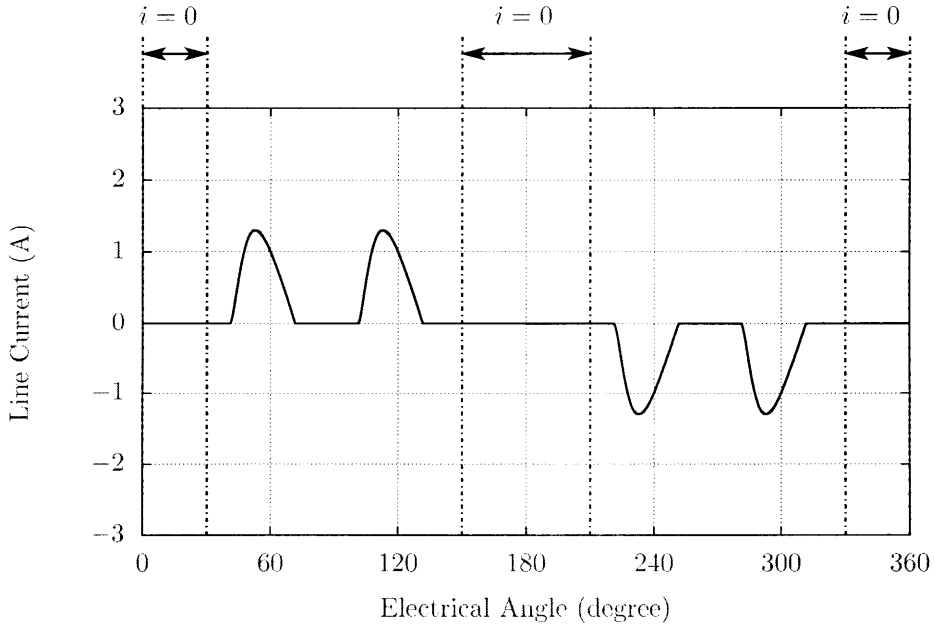


(b) Phase-A current

Figure 4.8: Current waveform and regions of zero-current of the VSD operated in the discontinuous conduction mode (DCM)

in radian as,

$$i[n] = 0 \quad \text{for } \frac{2\pi n}{N} \in \left[0, \frac{\pi}{6}\right] \cup \left[\frac{5\pi}{6}, \frac{7\pi}{6}\right] \cup \left[\frac{11\pi}{6}, 2\pi\right). \tag{4.6}$$

The constraint (4.6) holds under the assumption that there is no overlapping current between any two phases. The current must resides with in the window not included in (4.6). This assumption holds true for a voltage-source-inverter because the inverter usually does not include a large inductor to maintain a bus current like the current-source-inverter type. In the case of the VSD operating in DCM, the line current returns to zero before the intersections between two line voltages occur, as shown in Figure 4.8a. As a result, the assumption of the zero-current is acceptable for the VSD that uses the voltage-source-inverter.

For a periodic signal $i[n]$ sampled with the rate of $N$ point per period, the first region of zero-current specified in (4.6) $0 \leq \frac{2\pi n}{N} \leq \frac{\pi}{6}$ can be expressed mathematically using the Fourier synthesis equation (4.3) as,

$$\begin{aligned}
I_0 + I_1 \quad &+ I_2 \quad &&+ \cdots + I_{N-1} &&= i[0] \\
I_0 + I_1 e^{j\frac{2\pi}{N}} \quad &+ I_2 e^{j\frac{2\pi}{N}(2)} \quad &&+ \cdots + I_{N-1} e^{j\frac{2\pi}{N}(N-1)} &&= i[1] \\
I_0 + I_1 e^{j\frac{2\pi}{N}(2)} \quad &+ I_2 e^{j\frac{2\pi}{N}(2)(2)} \quad &&+ \cdots + I_{N-1} e^{j\frac{2\pi}{N}(N-1)(2)} &&= i[2] \\
&&&\vdots &&= \vdots \\
I_0 + I_1 e^{j\frac{2\pi}{N}(N_1)} \quad &+ I_2 e^{j\frac{2\pi}{N}(N_1)(2)} \quad &&+ \cdots + I_{N-1} e^{j\frac{2\pi}{N}(N-1)(N_1)} &&= i[N_1],
\end{aligned} \tag{4.7}$$

where $\frac{2\pi N_1}{N} = \frac{\pi}{6}$. Similarly, other zero-current regions can be translated and added to the system of equations (4.7).

Third, the load current waveform exhibits a specific symmetry. Examples load currents shown in Figures 4.1, 4.2, and 4.3, are approximately odd-symmetric. There are two ways to express this constraint. One method is to express in the time domain

as

$$i[n] = -i\left[n + \frac{N}{2}\right], \text{ for } 0 \leq n < \frac{N}{2}. \tag{4.8}$$

The number $\frac{N}{2}$ indicates the midpoint of the waveform. Alternatively, the constraint can be formulated in the frequency domain as zero even harmonics, specifically

$$I_{k_{\text{even}}} = 0, \tag{4.9}$$

where the subscript $k_{\text{even}}$ represents an even number, including zero. In the case of a VSD, the three-phase input voltage is assumed to be balanced and the VSD does not consume any triplen harmonics. This constraint can be represented as

$$I_{k_{\text{triplen}}} = 0, \tag{4.10}$$

The triplen harmonics are the harmonics with odd multiples of three such as 3rd, 9th, and 15th.

Fourth, the current signal is processed through the anti-aliasing filter and the analog-to-digital converter (ADC) in order to be converted into a digital form properly. The sampling frequency $F_s$ must be above the Nyquist frequency. The anti-aliasing filter confines the bandwidth of the signal, making the signal approximately band-limited. The band-limited property is depicted by the histograms of DFT coefficients in Figures 4.1, 4.2, and 4.3. The histograms indicate that most energy of the current waveform is contained in the low frequency region. The amplitude of higher harmonics are small and can be neglected. Mathematically, the band-limited constraint can be expressed as

$$I_{k_{\text{highfreq}}} \approx 0 \tag{4.11}$$

for some $k_{\text{highfreq}} > K_0$, where the parameter $K_0$ is a user-specified boundary. This constraint is an approximation of the frequency content of the current waveform. The

user can decide which frequency range is neglected.

Fifth, the current waveform is real. This real waveform property dictates the characteristics of the DFT coefficients, $I_k$. Given a real signal, the magnitude of the DFT coefficients $I_k$ is even, and the phase the DFT coefficients $I_k$ is odd [47]. In other words, most DFT coefficients are complex conjugate pairs. For example, the fifth harmonic $I_5$ forms a complex conjugate pair with $I_{N-5}$, where $I_{N-5} = I_5^*$. The complex conjugate pair property is used in the selection of the input harmonics.

The estimating function shown in (4.5) specifies a subset of DFT coefficients as input harmonics. In this paper, the estimator is derived iteratively as a function of input harmonics, the algorithm must be initialized to a reasonable number of harmonics, i.e. ten, with the goal to reduce this number as low as possible. The iterative process will reduce the number of input harmonics when possible.

The selection of the input harmonics depends on two factors: the availability of the harmonics in observations and the estimation error. In the field, the NILM must observe a collection of harmonics that are uniquely associated with the variable load. With the exception of the fundamental harmonic, other harmonics can be selected as input harmonics in the proposed method. The input harmonics should at least correlate with the fundamental harmonic. Therefore, any zero harmonic is discarded as an unfeasible option. Among available harmonics, harmonics with larger magnitude should be selected to improve signal-to-noise ratio, implying that they are less likely to be corrupted by a random noise source. One selection scheme is to select the input harmonics according to their magnitudes in a descending order. According to the histogram of the harmonic currents shown in Figure 4.1, the fifth, seventh and eleventh harmonics are the three largest harmonics among higher harmonics, listed in descending order. Therefore, these three harmonics can be selected as the candidates.

The real input signal implies the complex conjugate property of the DFT coefficients. The magnitude of the complex conjugate pair is the same as the harmonic itself. In the actual implementation, not all DFT coefficients have to be computed in

real time. Only the input harmonics are necessary in the estimation. The complex conjugate pair requires no additional computation at all. As a result, the complex conjugate pairs of the candidate input harmonics can be used with negligible memory and little computational cost. The number of input harmonic pairs used in the estimator is denoted by the symbol $K$. In the case of VSD, a possible input harmonic vector for the first iteration can be written as

$$I_{\text{input}} = [\, I_5, I_{N-5}, I_7, I_{N-7}, I_{11}, I_{N-11} \,]^T. \tag{4.12}$$

In this case, the estimator will uses three input harmonic pairs, $K = 3$, or six harmonics. The input harmonic vector $I_{\text{input}}$ is arranged according to the magnitude size in descending order. After the evaluation process, which is described in the next sub-sections, the smallest harmonic and its complex conjugate can be removed in the next iteration, leaving only two input harmonics pairs, $K = 2$. The process can be iterated by keeps reducing the number of input harmonic pairs $K$ until the estimation error just satisfies the accuracy requirement.

Finally, the system of equations is constructed by collecting constraints in (4.7), (4.9), (4.10), and (4.11). A subset of equations could be linearly dependent and must be eliminated. The system of linearly independent equations must have full row rank. Furthermore, the frequency constraints (4.9). (4.10), and (4.11) are more attractive because they reduce a number of DFT coefficients used in the computation, saving program memory and computational cost.

In this section, all five waveform constraints have been translated into mathematical equations. In addition, the selection of the input harmonics have been discussed. In the next step, the constraints equations must be rearranged to a matrix format that can be manipulated conveniently.

### 4.4.2 Matrix Equation

Once all linearly independent constraints have been identified, equations (4.7), (4.9), (4.10), and (4.11) can be re-written in a matrix form. The matrix equation can be expressed in the form of

$$A\mathbf{I}_{\mathrm{DFT}} = \mathbf{b} = \mathbf{0}, \tag{4.13}$$

where the matrix $A$ contains complex exponential values. The Fourier series coefficients vector, $\mathbf{I}_{\mathrm{DFT}}$, contains harmonics $I_k$. The vector $\mathbf{b}$ represents a constant zero vector.

To solve for the estimator, the matrix $A$ is constructed to have the dimension of $R$ rows by $R + 2K$ columns. The number of rows $R$ reflects all usable constraints describing the waveform, while the number of columns $R + 2K$ reflects $R$ constraints and the number of input harmonics $2K$, described in the last section. The $\mathbf{I}_{\mathrm{DFT}}$ can be partitioned into sub-blocks

$$\mathbf{I}_{\mathrm{DFT}} = [\, I_{\mathrm{goal}} \,|\, I_{\mathrm{others}} \,|\, I_{\mathrm{input}} \,]^T, \tag{4.14}$$

where the variable $I_{\mathrm{goal}}$ is the estimated harmonic, specifically the fundamental harmonic, $I_1$. The vector $I_{\mathrm{input}}$ consists of the input harmonic pairs as shown in (4.12). The vector $I_{\mathrm{others}}$ is comprised of other non-zero harmonics. The columns of matrix $A$ have to be rearranged in the similar order

$$A = [\, A_{\mathrm{goal}} \,|\, A_{\mathrm{others}} \,|\, A_{\mathrm{input}} \,], \tag{4.15}$$

where the matrix $A_{\mathrm{goal}}$ is a column vector of size $R$-by-1, containing coefficients associated with the goal harmonic, specifically the fundamental harmonic $I_1$ in this case. The matrix $A_{\mathrm{input}}$ contains all coefficients corresponding to the input harmonics in

$I_{\text{input}}$ and has a dimension of $R$-by-$2K$.

After the matrix $A$ and the DFT coefficient vector $\mathbf{I}_{\text{DFT}}$ are rearranged into a desired format. The goal is to manipulate the matrix $A$ to produce a row relating $I_{\text{goal}}$, i.e. $I_1$, to a small subset of input harmonics $I_{\text{input}}$ with all other harmonics in this row having zero coefficients.

### 4.4.3 Reduced Row Echelon Form

Once the system of equations has been set up in the matrix format, the next step is to compute the functional relationship between different harmonics. The algorithm uses a Gaussian elimination method to reduce the matrix $A$ into a reduced row echelon form (RREF), $A_{\text{RREF}}$. The RREF matrix $A_{\text{RREF}}$ can be broken into block matrices as

$$A_{\text{RREF}} = \left[\begin{array}{c|c|c} 1 & \mathbf{0} & C_{\text{goal}} \\ \hline \mathbf{0} & \mathbf{I} & C_{\text{others}} \end{array}\right]. \tag{4.16}$$

The most important part is the first row of the $A_{\text{RREF}}$ matrix. The row vector $C_{\text{goal}}$ contains the coefficients for the input harmonic vector $I_{\text{input}}$. Substitute the RREF matrix, $A_{\text{RREF}}$, in the matrix equation (4.13) and expand the multiplication result of the first row, the result can be expressed as

$$I_{\text{goal}} + \mathbf{0}I_{\text{others}} + C_{\text{goal}}I_{\text{input}} = 0. \tag{4.17}$$

By rearranging the terms, the equation (4.17) actually expresses a functional relationship between the estimated harmonic $I_{\text{goal}}$ and the input harmonics $I_{\text{input}}$ as

$$I_{\text{goal}} = -C_{\text{goal}}I_{\text{input}}. \tag{4.18}$$

The derived estimator is a linear estimator with complex coefficients. Equation (4.18) describes how to estimate the estimated harmonic $I_{\text{goal}}$ from a input harmonics $I_{\text{input}}$.

Specifically, the fundamental harmonic can be chosen as the target harmonic, i.e. $I_1 = I_{\text{goal}}$.

This section has shown the manipulation of the matrix equation (4.13) to obtain the estimator for the fundamental harmonic from the selected input harmonics $I_{\text{input}}$ as shown in (4.18). This candidate estimator must be verified that it can compute the fundamental harmonic with a reasonable error.

### 4.4.4 Estimator Evaluation

The last sections describe the procedure to set up constraints and compute the estimator for a given parameter. In this section, the estimator is evaluated and the adjustment for the subsequent iteration is described. The evaluation of the estimator is done by using the actual current to estimate the fundamental harmonic and compute the estimation error. The estimation error is measured in percentage,

$$\text{estimation error}\,(\%) = |I_1 - \widehat{I_1}|/|I_1| \times 100, \tag{4.19}$$

where the variable $I_1$ is the measured fundamental harmonic, and the variable $\widehat{I_1}$ is the estimated fundamental harmonic computed by the estimator.

Because the estimator in (4.18) is computed for a specific number of samples $N$ and a specific set of input harmonics, $I_{\text{input}}$, the estimator may not work well for other sampling rates. The band-limited signal sampled at the sampling frequency above the Nyquist rate should contain all information within the waveform. If the estimator predicts the fundamental harmonic accurately for a given sampling rate, estimators derived for higher sampling rates should predict accurately as well because more constraints can be listed in the system of equations. The band-limited property should improve the accuracy of the estimator as the sampling frequency becomes higher. The approximation of zero higher harmonic in (4.11) should become more accurate with increasing sample rate, but not necessary monotonically. As a result,

the estimation error should be consistently accurate across a range different sampling frequencies or samples per cycle $N_{\text{samp}}$.

Figure 4.9 depicts examples of the estimator evaluation for the VSD for the test currents shown in Figures 4.1a and 4.1b. In the first iteration, the estimators were derived using three harmonic pairs $K = 3$ as listed in (4.12) and different sample numbers $N_{\text{samp}}$. The estimation errors for $K = 3$ cases are shown in Figures 4.9a and 4.9b. The estimation errors are below 0.4 percent, indicating that the fundamental harmonic of the VSD can be estimated accurately using three harmonic pairs $K = 3$ indicated in (4.12).

In the next iteration, the input harmonics are reduced to two harmonic pairs the fifth, seventh, and their complex conjugates, $K = 2$. The procedures are iterated to obtain the estimator for $K = 2$ and different sample points $N_{\text{samp}}$. The estimation errors are shown in Figures 4.9c and 4.9d. The errors are below 2.5 percent across a wide range of sample points $N_{\text{samp}}$. As a result, the VSD estimator can use only two harmonic pairs $K = 2$ to estimate the fundamental harmonic with a reasonable error.

To examine if the number of input harmonics $I_{\text{input}}$ can be further reduced, the final iteration was done with $K = 1$, using only the fifth harmonic and its complex conjugate. The estimation errors are shown as a function of sample points $N_{\text{samp}}$ in Figures 4.9e and 4.9f. The result demonstrates the estimation error above 10 percent for many sample points. This result implies that the estimators will not perform consistently across different sample rates. Therefore, the VSD estimator derived using the proposed procedures should use at least two harmonic pairs $K = 2$ to accurately predict the fundamental harmonic.

This section has demonstrated the iterative procedures to derive the estimators based on the five waveform features by using the VSD load as an example. The input harmonics $I_{\text{input}}$ are chosen according to their availability and magnitude. The estimator is computed using a simple Gaussian elimination algorithm. Then the performance of the estimator is tested for consistency by measuring the estimation

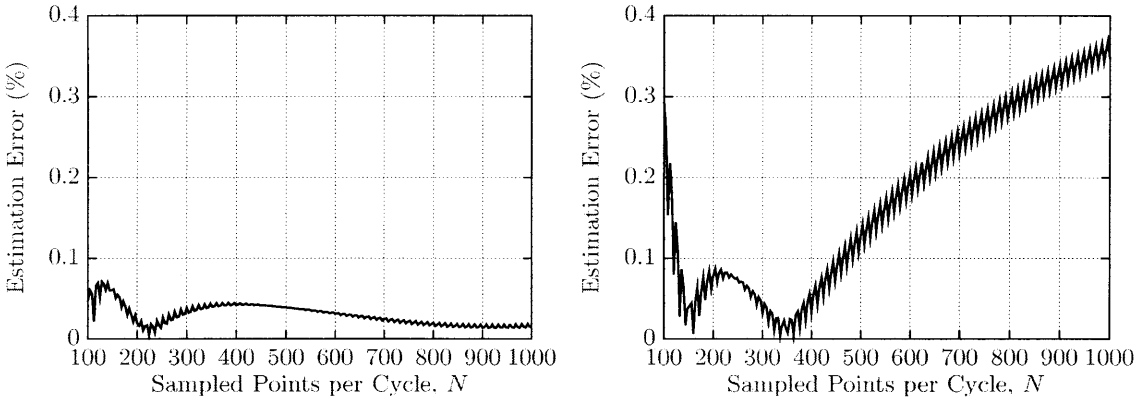


(a) Test current #1, $K = 3$




(b) Test current #2, $K = 3$

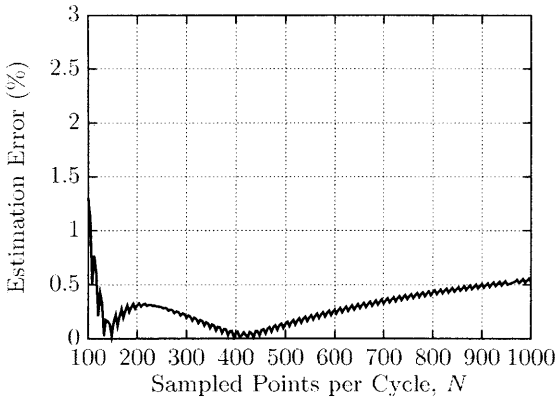


(c) Test current #1, $K = 2$

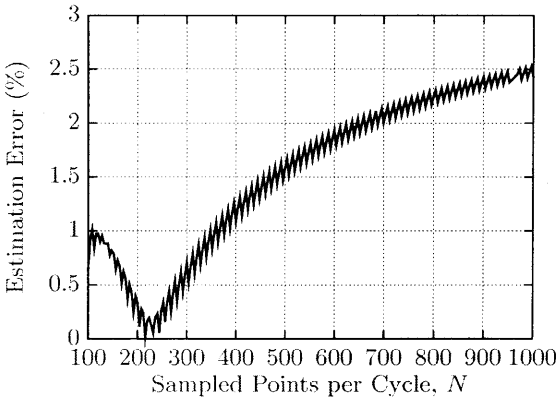


(d) Test current #2, $K = 2$

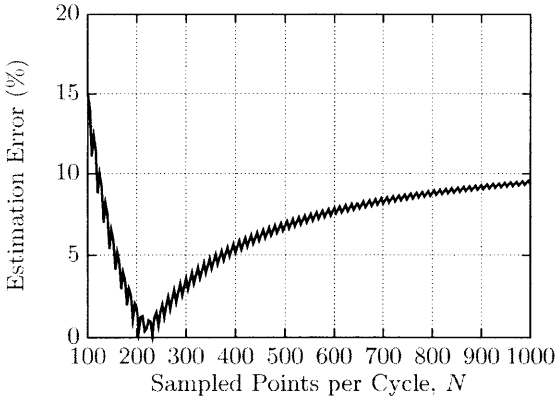


(e) Test current #1, $K = 1$

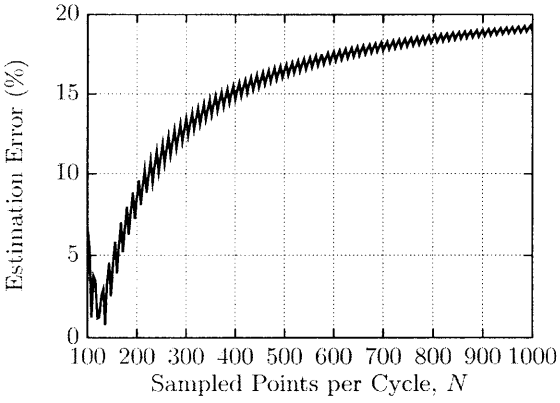


(f) Test current #2, $K = 1$

Figure 4.9: Estimation error as a function of sampling points $N_{\text{samp}}$ and input harmonic pairs $K$

error against two sets of VSD currents. The procedures are repeated with the reduced number of input harmonics by removing the harmonic with the smallest magnitude. The iteration is terminated when the estimation error exceeds the requirement. The best candidate is the estimator that satisfies the error requirement with the smallest number of input harmonics. The proposed method provides a guideline for getting the estimator in a linear form. The method gives the flexibility for the user to select the input harmonics $I_{\text{input}}$ and the method to verify the feasibility of such estimator.

Because the estimator is computed for different sample points $N_{\text{samp}}$, the computational error from the floating point arithmetic can mask the potential of the algorithm as the sample points $N_{\text{samp}}$ increases. To avoid the floating-point error problem, the proposed method uses a symbolic representation called a *cyclotomic field* to represent some coefficients in the matrix $A$. A brief discussion of the cyclotomic field is described in the later section.

### 4.4.5 Numerical Instability

The initial implementation of the waveform-based estimator was done in a floating-point arithmetic using programs written in MATLAB. Figure 4.10 shows the estimation errors from the estimators for $K = 2$ and $K = 1$ cases. As shown in Figure 4.10, the estimation errors decrease as the sampled number $N_{\text{samp}}$ increases, for small values of $N_{\text{samp}}$. However, the errors grow without bound when $N_{\text{samp}}$ is greater than 250, approximately. This error behavior indicates a numerical stability issue as the number $N_{\text{samp}}$ grows larger. Truncation error accumulates and causes to be inaccurate. Although the actual algorithm has a potential to solve the estimator with one harmonic, the numerical stability could prevent the full potential of the algorithm from being realized. In order to eliminate the numerical stability problem, a cyclotomic field representation is used in the computation, which is described in the next section.

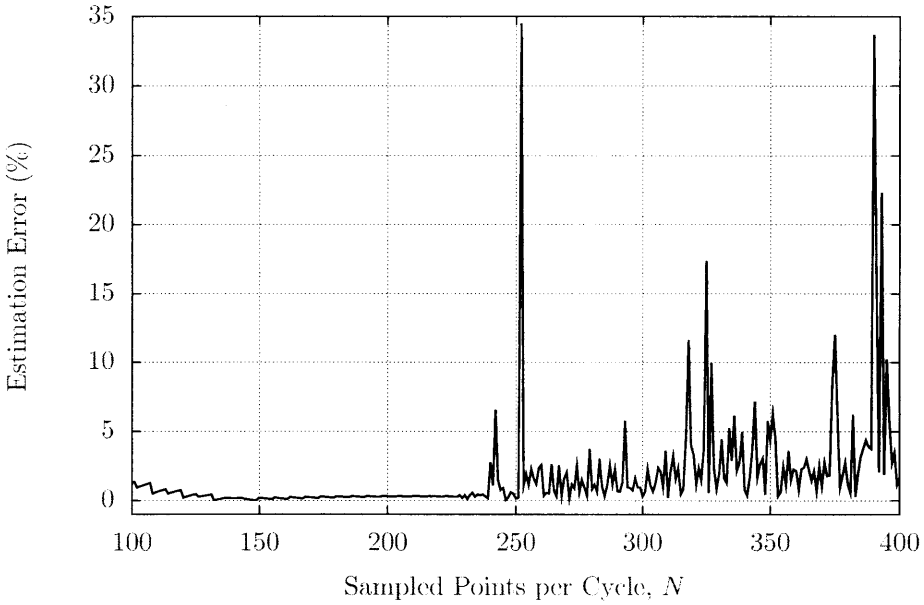


(a) $K = 2$

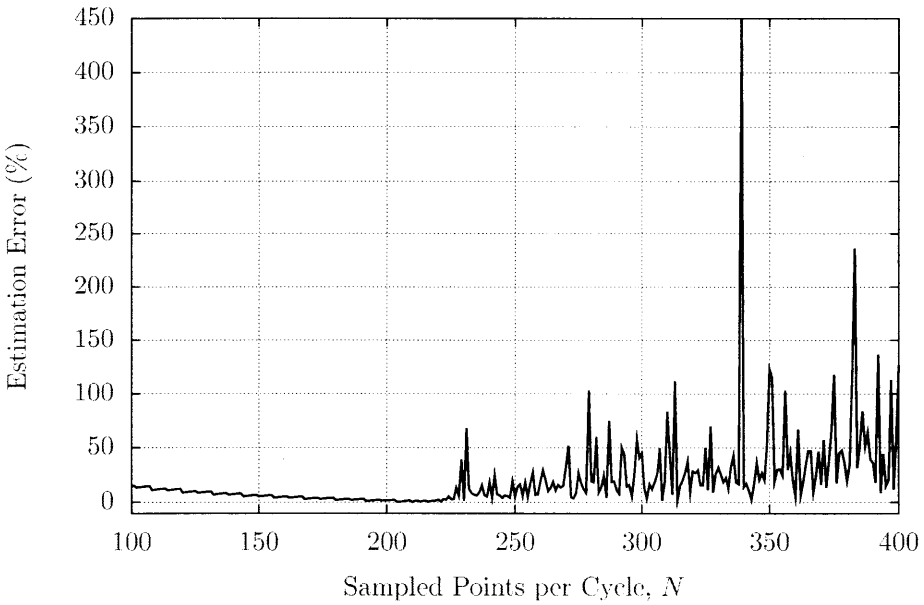


(b) $K = 1$

Figure 4.10: Estimation errors of the proposed estimator using floating-point arithmetic

## 4.5 Cyclotomic Field Representation

As shown in the previous section, the accuracy and potential of the RREF algorithm to solve this estimation problem are compromised by the error from the floating-point arithmetic. The solution is to convert the representation of coefficients to elements of a cyclotomic field, which allows the RREF algorithm to be calculated more accurately [19]. This section summarizes the cyclotomic field representation and some useful properties described in [19, 44–46].

### 4.5.1 Roots of Unity

Recall that the coefficients in the matrix $A$ in (4.13) are in the forms of $q_k e^{j\frac{2\pi k}{N}}$ for an integer $k \in [0, N-1]$ and a rational number $q_k$. Instead of fully representing these coefficients using a floating point representation, the proposed algorithm focuses on the rational number $q_k$ part while keeping the complex exponential part as a symbolic representation. The Gaussian elimination method involves only arithmetic operations such as addition, subtraction, multiplication, and division. These arithmetic operations of two matrix coefficients produce another coefficient with different complex numbers and complex exponents. At the end of each row operation, each coefficient of matrix $A$, $a_{m,n}$ can be described by a polynomial $p(\zeta_N)$ as

$$a_{m,n} = p(\zeta_N) = \sum_{k=0}^{N-1} c_k \zeta_N^k, \tag{4.20}$$

where the variable $\zeta_N$ is the complex exponential $e^{j\frac{2\pi}{N}}$. The complex exponential part has a property that

$$\zeta_N^{(k+N)} = \zeta_N^k. \tag{4.21}$$

The exponent power is always an integer modulo $N$. As a result, the polynomial would never grow more than $N$ terms with the highest power being $N-1$, specifi-

cally $e^{j\frac{2\pi(N-1)}{N}}$. This polynomial representation can be demonstrated by the following examples. Lets assume that two coefficients in the matrix $A$ are

$$a_{1,1} = e^{\frac{2\pi(11)}{12}} + 2e^{\frac{2\pi}{12}} + 3 \text{ and } a_{2,1} = 3e^{\frac{2\pi(5)}{12}}. \tag{4.22}$$

The multiplication between these two coefficients is given by

$$\begin{aligned}(a_{1,1}) \cdot (a_{2,1}) &= (e^{\frac{2\pi(11)}{12}} + 2e^{\frac{2\pi}{12}} + 3)(3e^{\frac{2\pi(5)}{12}}) \\ &= 3e^{\frac{2\pi(16)}{12}} + 6e^{\frac{2\pi(6)}{12}} + 9e^{\frac{2\pi(5)}{12}} \\ &= 6e^{\frac{2\pi(6)}{12}} + 9e^{\frac{2\pi(5)}{12}} + 3e^{\frac{2\pi(4)}{12}}. \end{aligned} \tag{4.23}$$

The division between these two coefficients is given by

$$\begin{aligned}(a_{1,1}) \,/\, (a_{2,1}) &= (a_{1,1}) \cdot (a_{2,1})^{(-1)} \\ &= (e^{\frac{2\pi(11)}{12}} + 2e^{\frac{2\pi}{12}} + 3)(\frac{1}{3}e^{\frac{2\pi(7)}{12}}) \\ &= \frac{1}{3}e^{\frac{2\pi(18)}{12}} + \frac{2}{3}e^{\frac{2\pi(8)}{12}} + e^{\frac{2\pi(7)}{12}} \\ &= \frac{2}{3}e^{\frac{2\pi(8)}{12}} + e^{\frac{2\pi(7)}{12}} + \frac{1}{3}e^{\frac{2\pi(6)}{12}}. \end{aligned} \tag{4.24}$$

These results can be represented in the polynomial format as

$$(a_{1,1}) \cdot (a_{2,1}) = 6\zeta_N^6 + 9\zeta_N^5 + 3\zeta_N^4, \text{ and} \tag{4.25}$$

$$(a_{1,1}) \,/\, (a_{2,1}) = \frac{2}{3}\zeta_N^8 + \zeta_N^7 + \frac{1}{3}\zeta_N^6, \tag{4.26}$$

where $N = 12$. These examples show that the operations always result in a polynomial of degree $N - 1$.

Furthermore, the complex exponential $e^{\frac{2\pi}{N}}$ is a *primitive root of unity*, which can be used a basis to generate others complex exponentials in the polynomial $p(\zeta_N)$. Complex exponentials and four possible primitive roots of unity in the case of $N = 12$

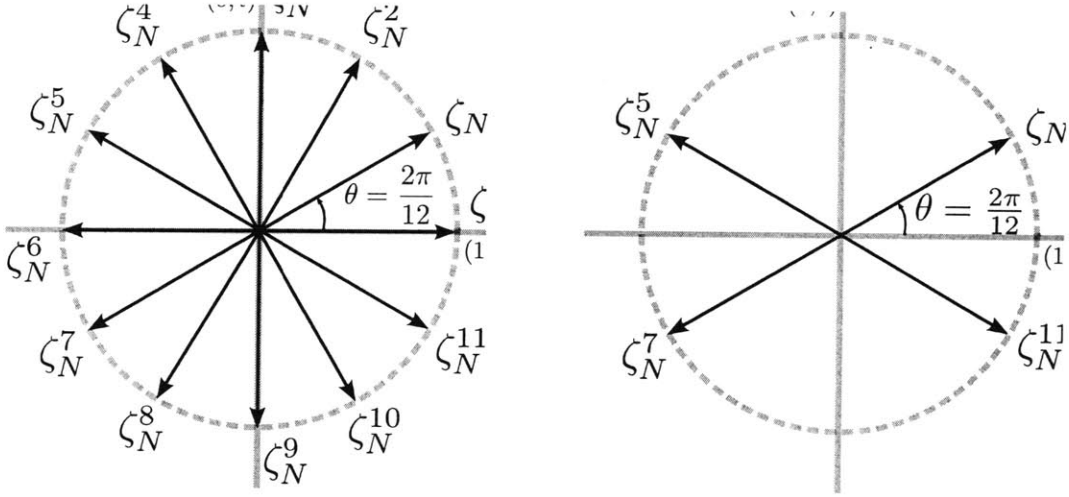


(a) Possible vectors $\zeta_N^k$

(b) Primitive roots of unity

Figure 4.11: Vectorial representations of the complex exponential $\zeta_N^k$ and the primitive roots of unity for $N = 12$

are shown in Figure 4.11. Any arithmetic computation of the coefficients in the matrix $A$ can be represented as a weighted sum of unit vectors. Therefore, it is advantageous to handle the complex exponentials symbolically in computation. The actual program only have to keep track of the coefficients of the complex exponentials in the polynomial $p(\zeta_N)$.

The coefficients of the complex exponentials in the matrix $A$ in (4.13) are initialized as rational numbers, $\mathbb{Q}$. The symbol $\mathbb{Q}$ represents a set of rational numbers. The set of rational numbers $\mathbb{Q}$ is also a field. The most important property of a field is that a field is closed under arithmetic operations. This property implies that every result of the arithmetic operation between two elements in the field remains in the field. Mathematically, given two rational numbers $q_1$ and $q_2$ as members of a set rational numbers $\mathbb{Q}$,

$$q_1 + q_2 \in \mathbb{Q} \text{ and } q_1 q_2 \in \mathbb{Q}. \tag{4.27}$$

The proposed estimator uses the Gaussian elimination method to perform row operations on the matrix $A$. The Gaussian elimination involves all four arithmetic operations: addition, subtraction, multiplication, and division. Because the coefficients of matrix $A$ belong to a set of rational number which is closed under arithmetic operations, all coefficients of the complex exponentials of the reduced row echelon form matrix $A_{\text{RREF}}$ must belong to the set of rational number as well. As a result, the Gaussian elimination method can be done exactly using the combination of a set of rational numbers $\mathbb{Q}$ together with a set of complex exponentials generated by the primitive root of unity $\zeta_N$ [19]. Mathematically, the combination of the set of rational numbers and the primitive root of unity creates the cyclotomic field $\mathbb{Q}[\zeta_N]$ by adjoining them together [19]. Using the cyclotomic field representation, the proposed algorithm can avoid the numerical instability of the floating-point error during the Gaussian elimination process. The floating-point error only occurs during the substitution of the complex exponentials to obtain the final estimator coefficients.

In addition, the right hand side of the system of the equation (4.13) is a zero vector. The operation can be done using only integer values because the denominator can be normalized without affecting the constraint at all. This thesis uses the rational numbers representation in the calculation. The computation is implemented in Pari/GP mathematical language, which provides a necessary platform to operate elements of the cyclotomic field [48].

## 4.6 Experimental Results

In this work, the algorithm is tested against three representative loads: a VSD, a computer, and a light dimmer. The VSD uses an uncontrolled three-phase rectifier, while the computer uses a full-wave rectifier. Finally, the light dimmer uses a TRIAC to control the brightness of an incandescent light bulb. The results show examples of the extraction of the fundamental harmonic current of the variable power loads from

the fixed power load. The results are shown in the real and reactive power, which can be computed as,

$$P = \frac{1}{2}\mathcal{R}\mathrm{e}(V_1\widehat{I}_1^*) \text{ and } Q = \frac{1}{2}\mathcal{I}\mathrm{m}(V_1\widehat{I}_1^*), \tag{4.28}$$

respectively for the single phase. The real and reactive powers are computed using the fundamental component only. For the three-phase loads such as VSDs and three-phase rectifiers, the real and reactive powers are computed using the fundamental components of each phase,

$$P = \frac{1}{2}\mathcal{R}\mathrm{e}(V_{1a}\widehat{I}_{1a}^* + V_{1b}\widehat{I}_{1b}^* + V_{1c}\widehat{I}_{1c}^*) \text{ and } Q = \frac{1}{2}\mathcal{I}\mathrm{m}(V_{1a}\widehat{I}_{1a}^* + V_{1b}\widehat{I}_{1b}^* + V_{1c}\widehat{I}_{1c}^*) \tag{4.29}$$

respectively.

### 4.6.1 Variable Speed Drive

This test uses a VSD, a three-phase rectifier driving a load, and a 50-Watt incandescent light bulb to demonstrate the ability of the waveform-based estimator in the field usage. The VSD and the three-phase rectifier are connected to the three-phase power supply. The light bulb is only connected to the phase-A line voltage. The experimental setup is shown in Figure 4.12. The VSD estimator used in this experiment is given by

$$\begin{aligned}\widehat{I}_{1-\mathrm{vsd}} = &(1.358 - 0.102j)I_5 + (-0.903 - 0.102j)I_5^* \\ &+ (0.731 - 0.082j)I_7 + (-0.547 - 0.082j)I_7^*.\end{aligned} \tag{4.30}$$

The computation of these coefficients uses the program written in the Appendix C.

There are multiple events occurring in this experiment. At the time $t = 4$ seconds, the incandescent light bulb turned on. The light bulb remained turned on

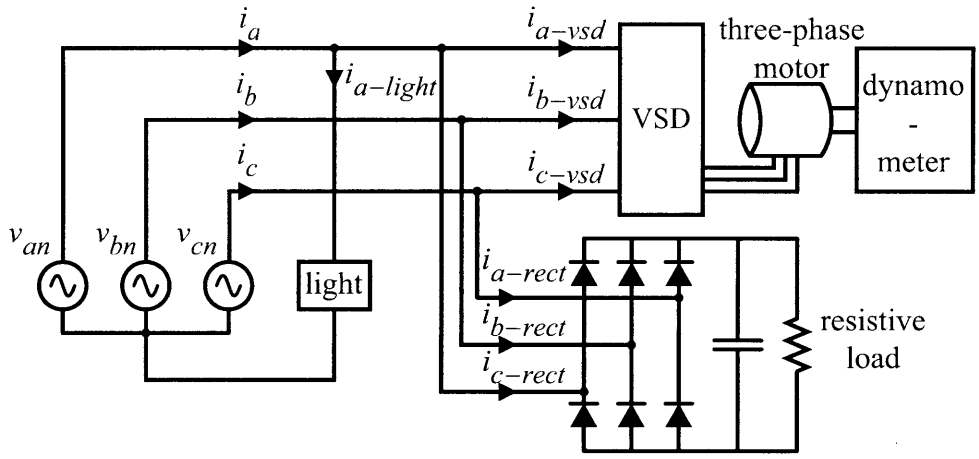


Figure 4.12: Experimental setup for testing the VSD estimator

through out this experiment. The VSD started ramping up at the time $t = 8$ seconds and reached the steady state at the time $t = 18$ seconds. The fixed-load three-phase rectifier turned on at the time $t = 27$ seconds and turned off at the time $t = 39$ seconds. Then the VSD started to ramp down the power at the time $t = 43$ seconds and completely stopped at the time $t = 53$ seconds. Figure 4.13 shows the real power consumption of the total power, the estimated three-phase rectifier, and the estimated incandescent light using the waveform-based estimator. The estimator used two harmonic pairs $K = 2$, specifically the fifth and seventh harmonics to compute the fundamental harmonic consumed by the VSD and three-phase rectifier. The incandescent light bulb consumed approximately 50 W as expected. The result illustrates the capability of the proposed algorithm for the VSD and the three-phase rectifier. The estimation errors can be seen at the turn-on transient regions. These errors are expected because the sharp transient consists of a spectrum of harmonics. As a result, the input harmonics are corrupted leading to the estimation error. Nevertheless, the estimator gives accurate results under the steady-state condition.

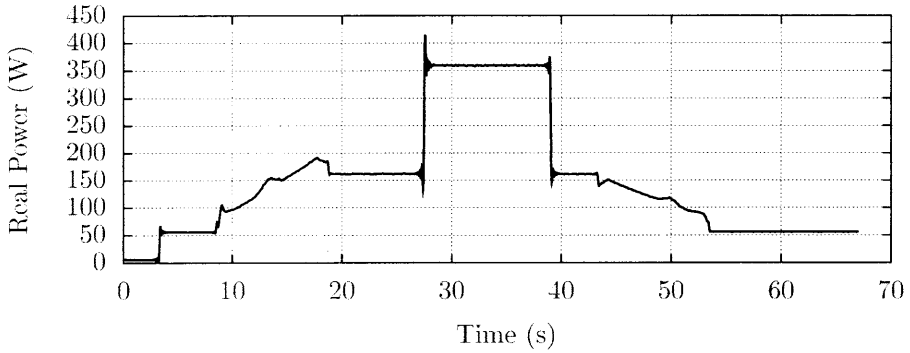


(a) Aggregate real power consumption of the VSD and the incandescent light

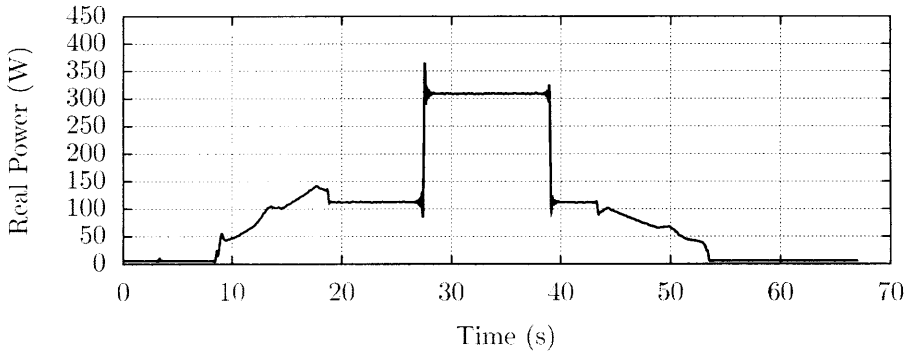


(b) Estimated real power consumption of the VSD

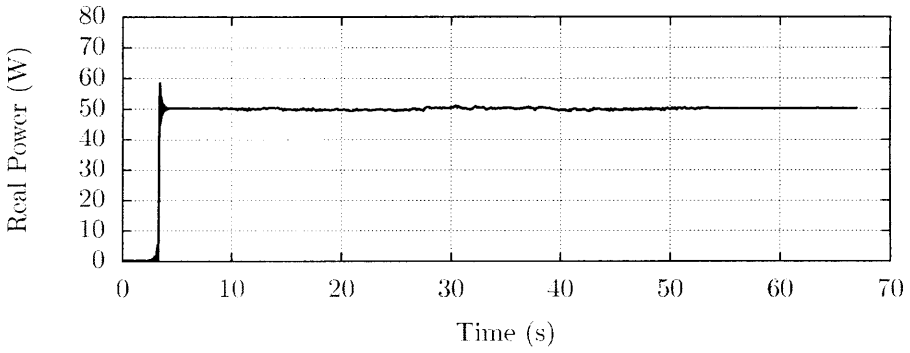


(c) Estimated real power consumption of the incandescent light

Figure 4.13: Demonstration the waveform-based estimator extracting the real power consumption of the VSD from the incandescent light. The real power consumption of both the incandescent light and the VSD is shown in (a). The estimated real power consumed by the VSD is shown in (b). The estimated real power consumed by the incandescent light bulb is shown in (c).

### 4.6.2 Computer

In the single phase environment, a computer is used to represent a typical load that use a full-wave rectifier in the power supply. In this experiment, a computer and a 100-Watt incandescent light bulb are monitored together. The reference voltage and regions of zero-current used to compute the estimator are shown in Figure 4.14. Specifically, the computer's is expected to consume the current during the window specified as a function of electrical angle specified in radian,

$$i[n] = 0 \text{ for } \frac{2\pi n}{N} \in \left[0, \frac{\pi}{3}\right] \cup \left[\frac{2\pi}{3}, \frac{4\pi}{3}\right] \cup \left[\frac{5\pi}{3}, 2\pi\right). \tag{4.31}$$

In the case of the computer, the waveform-based estimator uses three harmonic pairs, the third, fifth, seventh, and their complex conjugates to estimate the fundamental harmonic of the computer. The coefficients used in this experiment were computed using the program in the Appendix C. The computer estimator is given by

$$\begin{aligned} \widehat{I}_{1-\text{comp}} = &(-0.744 - 1.214j)I_3 + (-0.324 - 0.636j)I_3^* \\ &+ (0.458 - 0.898j)I_5 + (-0.673 - 0.530j)I_5^* \\ &+ (0.326 - 0.026j)I_7 + (-0.145 + 0.200j)I_7^*. \end{aligned} \tag{4.32}$$

The experimental setup for this test is shown in Figure 4.15.

In this experiment, the sequence of events can be described as follows. First, the light turned on at the time $t = 2$ seconds and turned off at the time $t = 32$ seconds. The computer turned on at the time $t = 12$ seconds and remained on for approximately 3 seconds. The computer turned off at the time $t = 15$ seconds. The computer turned on again at the time $t = 22$ seconds and remained active for 9 seconds. The computer turned off at the time $t = 31$ seconds. After the light had turned off at the time $t = 32$ seconds, the computer turned on first at the time = 42 seconds. At the time $t = 46$ seconds, the light turned on for 4 seconds, before turning

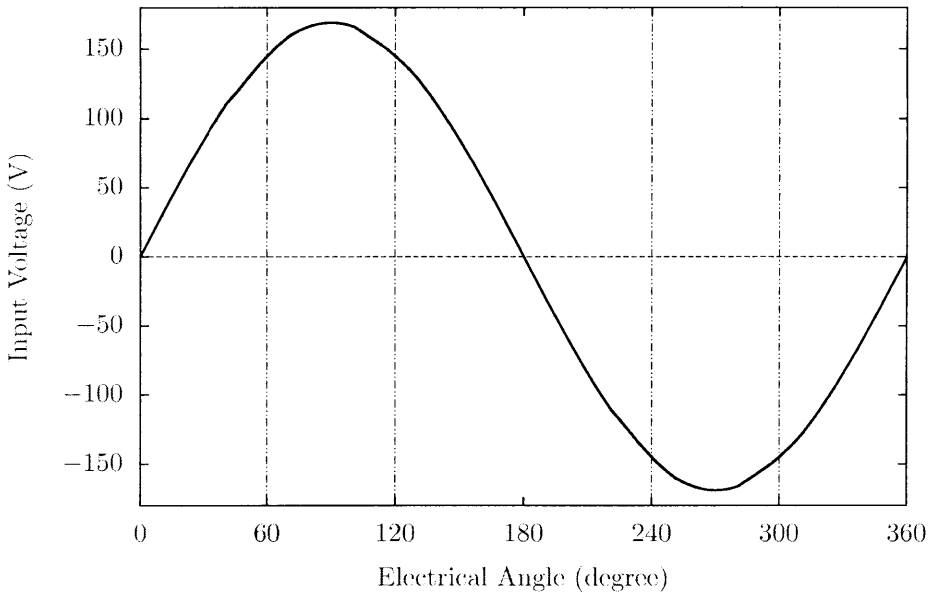


(a) Reference voltage

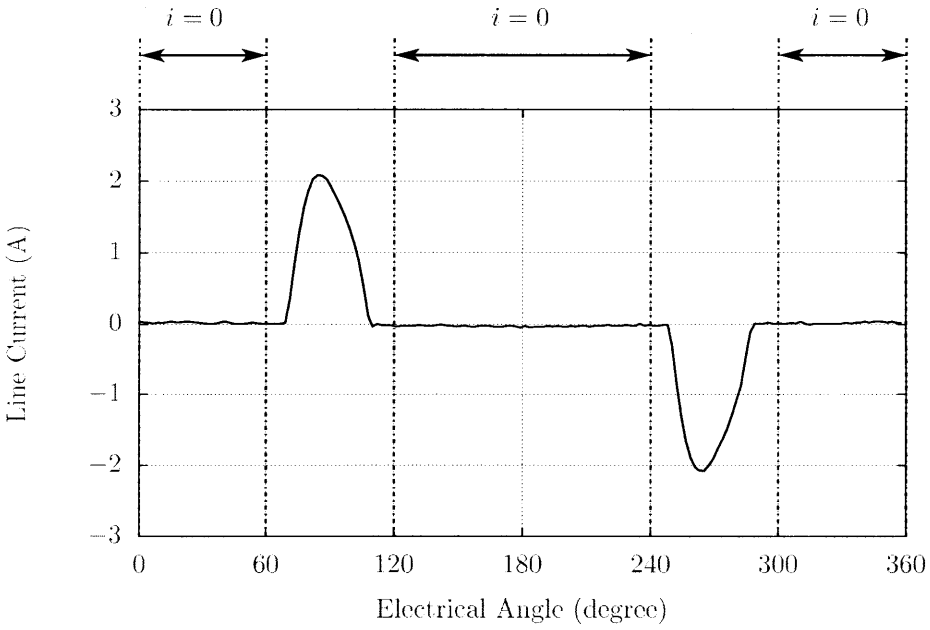


(b) Regions of zero-current

Figure 4.14: Reference voltage and approximated regions of zero-current for the computer

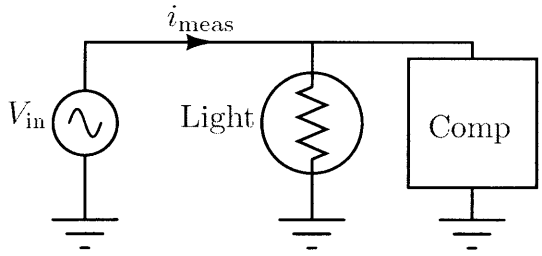


Figure 4.15: Experimental setup for resolving the power consumption of the computer from the incandescent light bulb

off at the time $t = 50$ seconds. The computer was finally turned off at the time $t = 53$ seconds. The experimental result is shown in Figure 4.16. The results show that the estimator can extract the fundamental harmonic, which is used to compute the power consumption of the computer accurately using only three harmonic pairs $K = 3$. The errors during the turn-on transients are expected because the 100-W incandescent light bulb consumes a spectrum of current harmonics, including the third, fifth, and seven harmonics during the transients. As a result, these harmonics are not uniquely associated with the computer, causing the estimation error.

### 4.6.3 Light Dimmer

In the this experiment, the estimator was derived to extract the power consumption of the TRIAC-based light dimmer. The dimmer adjusts the brightness and power consumption by varying the firing angle of the TRIAC to chop off the sinusoidal input voltage feeding the incandescent light bulb. Sharp transients of the current waveform results in many harmonic currents as shown in the histogram in Figure 4.3. In the case of the dimmer, the ideal current waveform is used to derived the estimator. An example of the ideal waveform is shown in Figure 4.17. The ideal waveform does not have the initial current pulse at the beginning of the line cycle. This approximation allows the five waveform features to be recognized more easily. Because the firing angle of the TRIAC varies continuously, multiple dimmer estimators have been computed

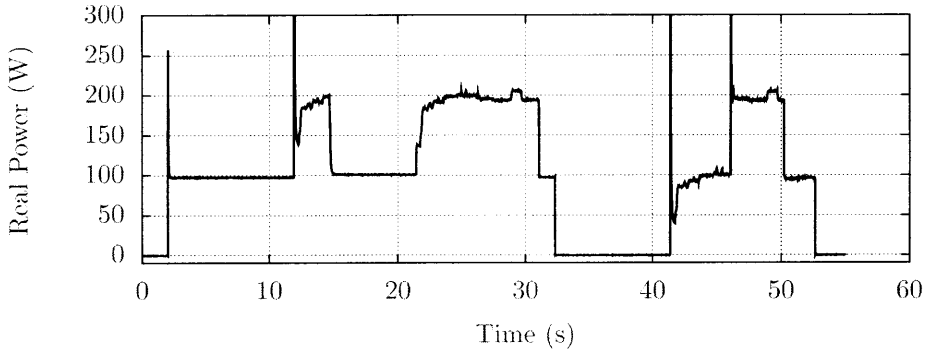


(a) Aggregate real power consumption of the computer and the incandescent light

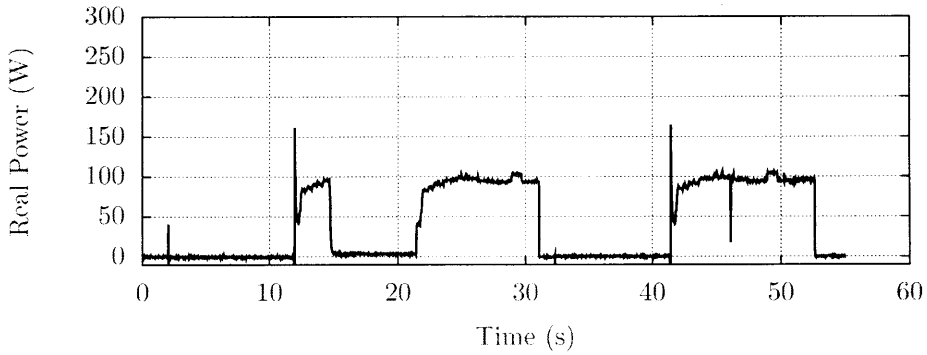


(b) Estimated real power consumption of the computer

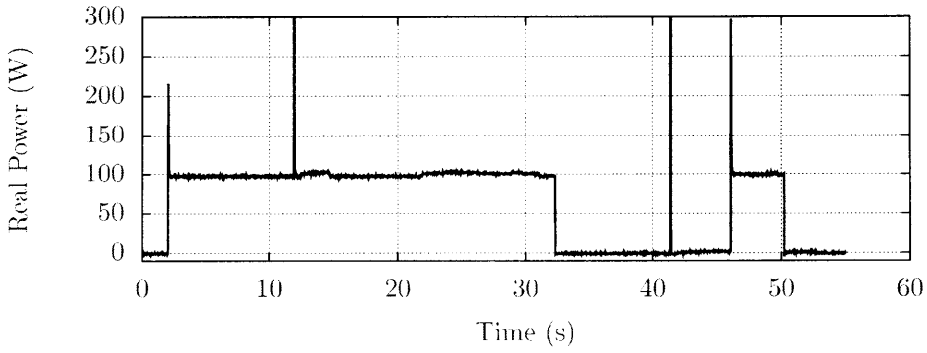


(c) Estimated real power consumption of the incandescent light

Figure 4.16: Demonstration of the waveform-based estimator extracting the real power consumption of the computer from the incandescent light. The aggregate real power consumption of the computer and the incandescent light is shown in (a). The estimated real power consumption of the computer is shown in (b). The estimated real power consumption of the incandescent light is shown in (c).

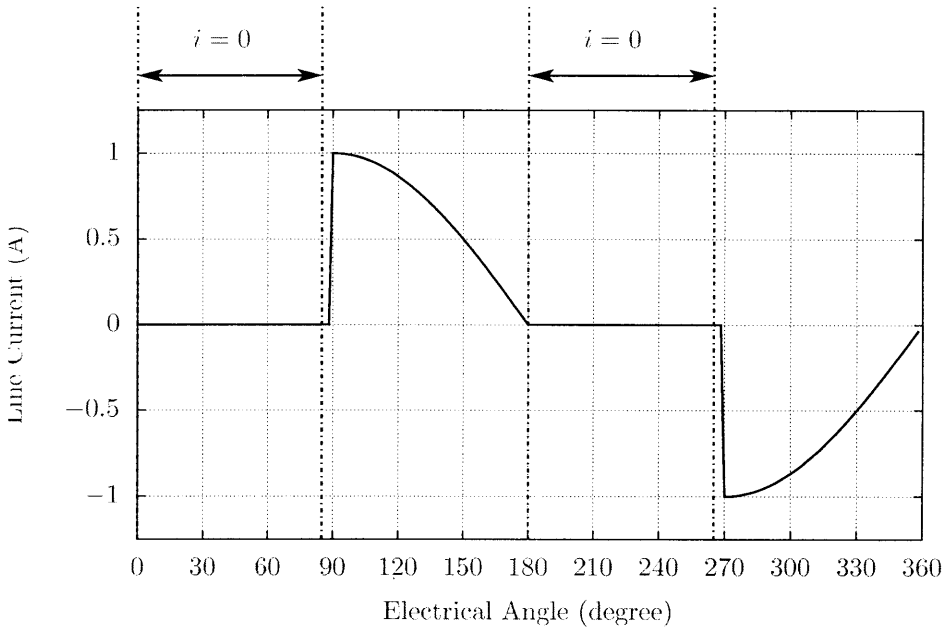


Figure 4.17: Example of the current waveform and approximated zero-current regions of the TRIAC-based light dimmer

for different firing angles.

The estimator for the light dimmer uses four harmonic pairs, the third, fifth, seventh, ninth and their complex conjugates, $K = 4$, to estimate the fundamental harmonic. The coefficients of the light dimmer estimator are computed using the code shown in the Appendix C. The dimmer estimator is separated into three cases depending on the higher harmonics. In the first case, if the imaginary part of the third harmonic is negative, $\mathcal{I}\mathrm{m}(I_3) < 0$, then

$$\begin{aligned}\widehat{I}_{1-\mathrm{dimmerA}} = &(-1.420j)I_3 + (-0.793)I_3^* \\ &+ (1.075)I_5 + (0.865j)I_5^* \\ &+ (0.458j)I_7 + (0.459)I_7^* \\ &+ (-0.095)I_9 + (-0.108j)I_9^*.\end{aligned} \tag{4.33}$$

This estimator assumes the dimmer current satisfies the following constraint,

$$i[n] = 0 \text{ for } \frac{2\pi n}{N} \in \left[0, \frac{\pi}{2}\right] \cup \left[\pi, \frac{3\pi}{2}\right]. \tag{4.34}$$

However, if the imaginary part of the third harmonic is positive and the imaginary part of the seven harmonic is also positive, i.e. $\mathcal{I}\mathrm{m}(I_3) > 0$ and $\mathcal{I}\mathrm{m}(I_7) > 0$, the dimmer estimator is given by

$$\begin{aligned}\widehat{I}_{1-\text{dimmerB}} = &(-0.819 - 1.226j)I_3 + (-0.354 - 0.854j)I_3^* \\ &+ (0.479 - 1.157j)I_5 + (-1.202 - 0.239j)I_5^* \\ &+ (0.651 - 0.129j)I_7 + (-0.613 + 0.613j)I_7^* \\ &+ (0.126 + 0.126j)I_9 + (0.059 + 0.296j)I_9^*.\end{aligned} \tag{4.35}$$

The second estimator assumes the dimmer current satisfies the following constraint,

$$i[n] = 0 \text{ for } \frac{2\pi n}{N} \in \left[0, \frac{2\pi(55)}{360}\right] \cup \left[\pi, \frac{2\pi(235)}{360}\right]. \tag{4.36}$$

Otherwise, the dimmer estimator is given by

$$\begin{aligned}\widehat{I}_{1-\text{dimmerC}} = &(-1.291 - 1.060j)I_3 + (0.164 - 0.823j)I_3^* \\ &+ (-0.332 - 1.670j)I_5 + (-0.539 - 1.009j)I_5^* \\ &+ (0.546 - 1.022j)I_7 + (-0.812 - 0.336j)I_7^* \\ &+ (0.404 - 0.167j)I_9 + (-0.339 + 0.103j)I_9^*.\end{aligned} \tag{4.37}$$

The last estimator assumes the dimmer current satisfies the following constraint,

$$i[n] = 0 \text{ for } \frac{2\pi n}{N} \in \left[0, \frac{2\pi(40)}{360}\right] \cup \left[\pi, \frac{2\pi(220)}{360}\right]. \tag{4.38}$$

The test setup for the light dimmer experiment is shown in Figure 4.18.

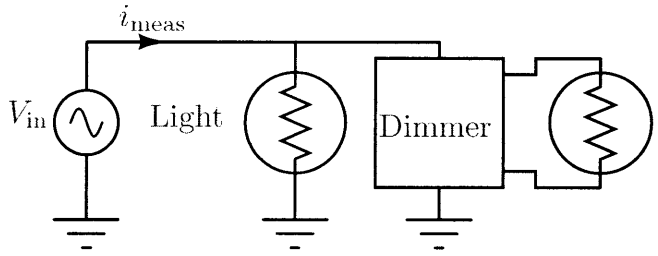


Figure 4.18: Experimental setup for resolving the power consumption of the light dimmer

Experimental results are demonstrated in Figs. 4.19 and 4.20. Three estimators are used to track the power consumption of the light dimmer. The experimental results demonstrate that the estimator can track the real and reactive power consumption of the light dimmer reasonably well. The incandescent light consumes mostly the real power as expected. The reactive power is mostly consumed by the light dimmer.

The experimental results have demonstrated the ability of the waveform-based estimator to resolve and track the real and reactive power of the variable power loads. The four-step procedure is described in details how to derive the estimator from the five waveform features. The iterative process systematically reduces the number of input harmonics used for estimation to the smallest number when possible. The cyclotomic field representation allows the computation to be done without the floating-point arithmetic error. The estimator computation is done off-line and the results are the coefficients for different input harmonics. The actual estimation only involves only few multiplications and additions. As a result, the estimator can compute the estimated harmonic and power consumption in real time.

## 4.7 Summary

This chapter has demonstrated a powerful method to create a harmonic estimator for continuously variable power loads such as VSDs, computers, and light dimmers. The

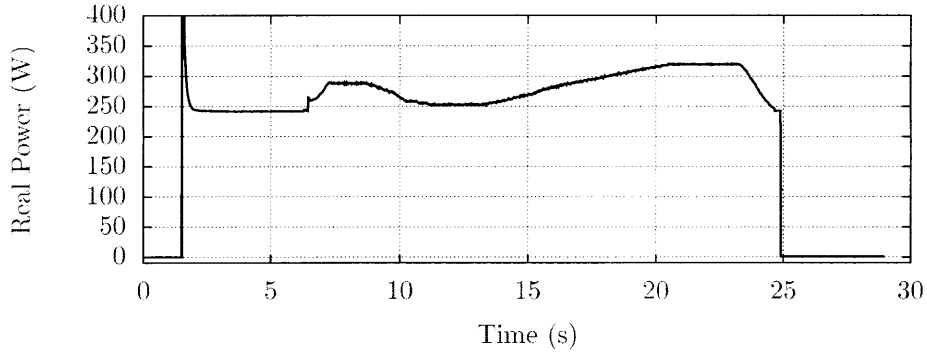


(a) Aggregate real power consumption of the light dimmer and the incandescent light

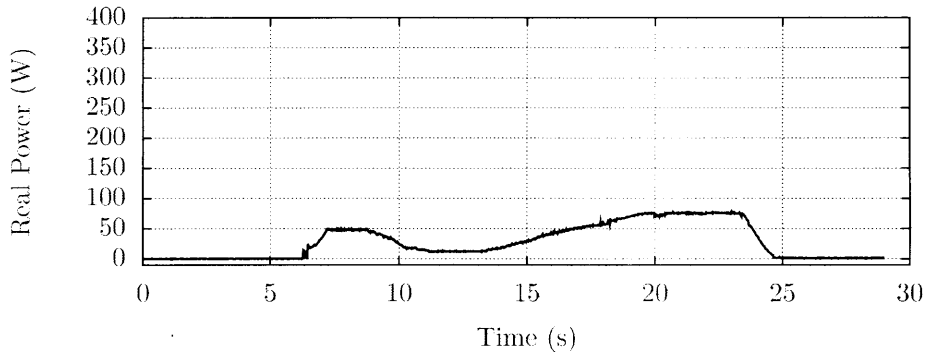


(b) Estimated real power consumption of the light dimmer

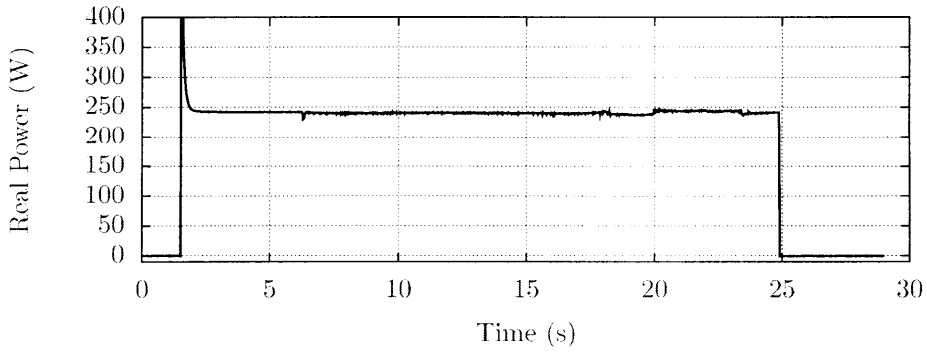


(c) Estimated real power consumption of the incandescent light

Figure 4.19: Demonstration the waveform-based estimator extracting the real power consumption of the light dimmer from the incandescent light. The real power consumption of both the incandescent light and the light dimmer is shown in (a). The estimated real power consumed by the light dimmer is shown in (b). The estimated real power consumed by the incandescent light bulb is shown in (c).

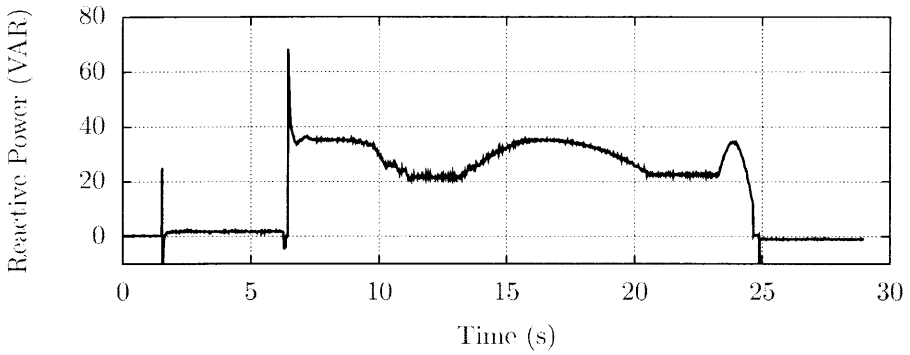


(a) Aggregate reactive power consumption of the light dimmer and the incandescent light

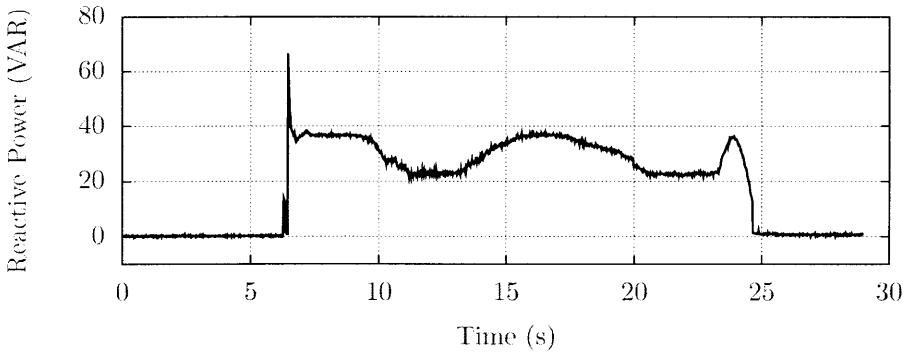


(b) Estimated reactive power consumption of the light dimmer

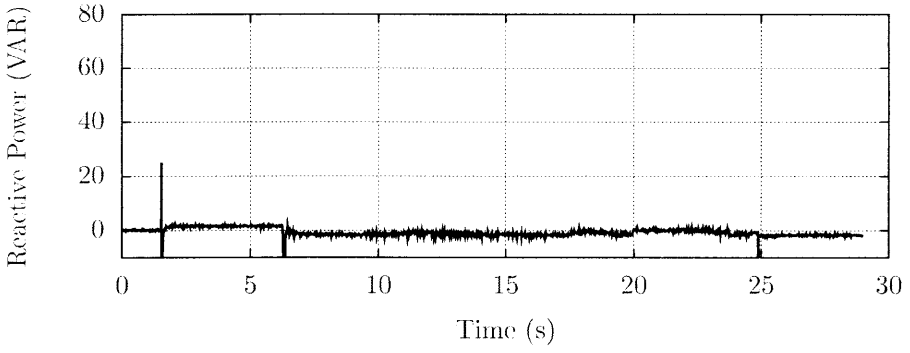


(c) Estimated reactive power consumption of the incandescent light

Figure 4.20: Demonstration the waveform-based estimator extracting the reactive power consumption of the light dimmer from the incandescent light. The measured reactive power consumption of both the incandescent light and the light dimmer is shown in (a). The estimated reactive power consumed by the light dimmer is shown in (b). The estimated reactive power consumed by the incandescent light bulb is shown in (c).

paper details the iterative procedures to translates five waveform features into a set of linear equations based on the Fourier synthesis relation. The estimator uses a four-step process to transform the waveform features to the estimator. These five structural features in the current waveforms are translated into linear equations based on the Fourier synthesis equations. A simple linear algebra such as the Gaussian elimination method is applied to reduced the set of linear equations to the desired estimator. Finally, the derived estimator is evaluated and the four-step process can be repeated if desired. Experimental results have confirms the ability and flexibility of the proposed method. The cyclotomic field representation solves the computational error from the floating-point arithmetic. This waveform-based estimator allows the energy score-keeping and load monitoring applications to resolve and track with variable power loads in the aggregate measurements of data without fully analyzing the load in details.

# *Chapter 5*

# *Conclusion and Future Work*

As electricity demand continues to increase, the electricity generation technologies have been developed to satisfy the demand from the supply side. Smart Grid technology is one of many potential instruments to keep the power system ready for higher electricity demand in the future. The "smart grid" relies on the extensive communication network that can direct necessary and useful information for utilities, generators, grid operators and consumers to efficiently and optimally deal with their electricity operations. The information can be collected and measured by a smart metering device. The smart metering device can provide the required information such as power consumption, which can be used by both utilities and consumers. For example, the electricity consumption can be used for billing as well as planning the electricity supply. In addition, the power consumption can be used in the demand side management program to lower the electricity bill for the customer as well. However, the electrical voltage and current signals can provide valuable information about loads at the metered site.

The nonintrusive load monitoring (NILM) has demonstrated the ability to extract crucial diagnostic and device parameters from the voltage and current signals from the aggregate measurements at a central location. As shown in many past experiments and this thesis, the NILM system can also be classified a "smart" metering device that can provide compact and useful information for both utilities and consumers.

Modern technologies have produces many complex machines and electrical appliances that can operate optimally. As the NILM expands the load monitoring

and diagnostic coverage, loads with power electronics are likely to be encountered. These power electronics loads present an opportunity for NILM to perform diagnostic assessments and to track power consumption of these power electronic loads. Many power electronics loads such as VSDs and computers belong to a class of variable power loads. The NILM is required to adjust the load disaggregation method to deal with these variable power loads.

As the NILM is installed to monitor more loads, the current sensor must be able to measure a larger range of current signal. The NILM can resolve the issue by using a larger current sensor, possibly trading bandwidth and resolution for dynamic range. This trade-off can affect many diagnostic applications that rely on the extraction of a small and high frequency signals embedded in a large but low frequency current signal. These two issues have presented inevitable challenges for a future nonintrusive load monitoring research and must be addressed.

This thesis has demonstrates three solutions for the nonintrusive load monitoring (NILM) system in both sensing and signal processing aspects. The solutions include the improved sensor design and two algorithms to compute the power estimators for variable power loads.

The physically-windowed sensor has been designed and prototyped to demonstrate an alternative way to exploit the frequency separation of the slow moving envelop and the small but fast dynamic signal in the current sensor design. The sensor design separates the system into two sub-systems to take care of two different frequency ranges. By separating the design for each frequency region, each sub-system can be optimized for the input signal in the specified frequency range. Specifically, the "windowing" concept allows the sensor design to take advantage of trade-offs between bandwidth and dynamic range. Experimental results from the prototyped circuit have shown the ability to design the current sensor with a $\pm 80$ A at 10 mA resolution, approximately 14 bits. By constructing this prototype, this thesis has demonstrated and confirmed the concept that the signal measurement can be done

in sections or "windows". This "windowing" concept has been applied in many measurement applications and can be further improved to meet a specific requirement with available technologies.

Furthermore, the thesis also addresses the problem of disaggregating variable power loads in the aggregate current measurements. Two solutions have been proposed to address this problem. The first solution uses a model-based estimator to approximate the behavior of a three-phase uncontrolled rectifier to compute the coefficients that relate a set of higher harmonic currents to the fundamental harmonic. Using the reduced model, the model-based estimator can track the power consumption of variable speed drives (VSDs) accurately. The model-based estimator provides a closed form equation for the estimator. As a result, the computation cost is relatively low. Experimental results have shown that the model-derived VSD power estimator can track the power even with small variations of the input voltage: voltage harmonics and distortions. This technique eliminates the need to recompute the estimator for every possible input variation that always occur in the field.

The second solution for tracking variable power loads presented in this thesis is the waveform-based estimator. The waveform-based estimator exploits five structural features in the current waveforms to compute the estimator coefficients. The algorithm is based on the Fourier analysis and synthesis equations to compute the relationship between the higher harmonics and the fundamental harmonics. The waveform-based estimator is different from the model-based estimator because the waveform-based estimator does not require the analysis of internal circuits of the load. The ability to compute the power estimator of a variable power only from the current waveform allows the NILM to possibly disaggregate and track any variable power load with structural features in the current waveform. Experimental results have shown that the waveform-based estimators can be computed for common variable power loads such as VSDs, computers, and light dimmers.

There are many possible extensions from the results of this thesis. For exam-

ple, both the model-based estimator and the waveform-based estimator for the VSD assume that the VSD is operated in the discontinuous conduction mode (DCM). This assumption holds very well for the voltage-source-inverter (VSI) type. In the case of a current-source-inverter (CSI), line currents can not be restricted by the ideal switching function or the region of zero-current because line currents can commutate between two phases. This operating region is called a continuous conduction mode (CCM), indicating that the dc-bus current never becomes zero. Future researches can be explored to find an power estimator for the VSD operated in CCM. One possible option is to modify the model-based estimator to use a different switching function, i.e. a trapezoidal function, to derive the estimator.

In the case of a TRIAC-based light dimmer, the waveform-based estimator has computed the estimator primarily based on the regions of zero-current. However, there is an alternative way to parameterize the current waveform of the TRIAC-based light dimmer. The dimmer adjusts the brightness by nulling the voltage waveform at the appropriate electrical angle. In the ideal situation, the voltage waveform can be considered a pure sinusoidal waveform. Conceptually, the dimmer applies a rectangular modulation function to the sinusoidal waveform to produce the voltage waveform applied to a resistive load, i.e. an incandescent light bulb. The current consumed by the light dimmer is proportional to the modulated voltage because the load is resistive. The problem of finding the amount of the fundamental harmonic from higher harmonics can possibly be done by a deconvolution procedure because the voltage is assumed to be a pure sinusoidal voltage. The waveform-based estimator uses the cyclotomic field representation to accurately compute the reduced row echelon form (RREF) of the Fourier matrix equation. The deconvolution could be done accurately under this restricted condition using the cyclotomic field representation as well.

Another possible application is to improve the four-step iterative process in the waveform-based estimator by studying the current harmonic consumed by the load. The proposed waveform-based estimator has established a systematic procedure to

derive an estimator for a variable power load whose current contains any structural features. The proposed algorithm is also useful for reducing the estimation error or lowering the number of input harmonics in the estimating function. The introduction of the cyclotomic field representation has improved the computational accuracy significantly. However, the underlying method remains an iterative method. That is the estimator coefficients are derived and tested iteratively until the estimation error just satisfies the accuracy requirement. In addition, the selection of the input harmonics is currently based on the magnitude only. The study of the higher harmonics associated with each load could reveal a better strategy to determine a necessary set of harmonics required for a given accuracy requirement.

In addition, the physically-windowed sensor design also enables different methods to measure the input signal. In the current design, the "window" of the input current is fixed and moved dynamically according to a simple algorithm. The window is moved by a fixed amount when the signal grows beyond the thresholds. However, more sophisticated "windowing" algorithms can be applied, a predictive windowing for example. Hence, the "windowing" strategy is a possible research extension to this thesis.

Furthermore, the physically-windowed concept can be applied in other areas such as mechanical and biological sensing, where the input signals contain two separate frequency groups.

*Appendix A*

# *Circuit Schematic for Physically-Windowed Sensor*

---

This section includes the schematics for of the physically-windowed sensor described in Chapter 2. The reference design for the physically-windowed sensor are shown in Figures A.1 through A.12.

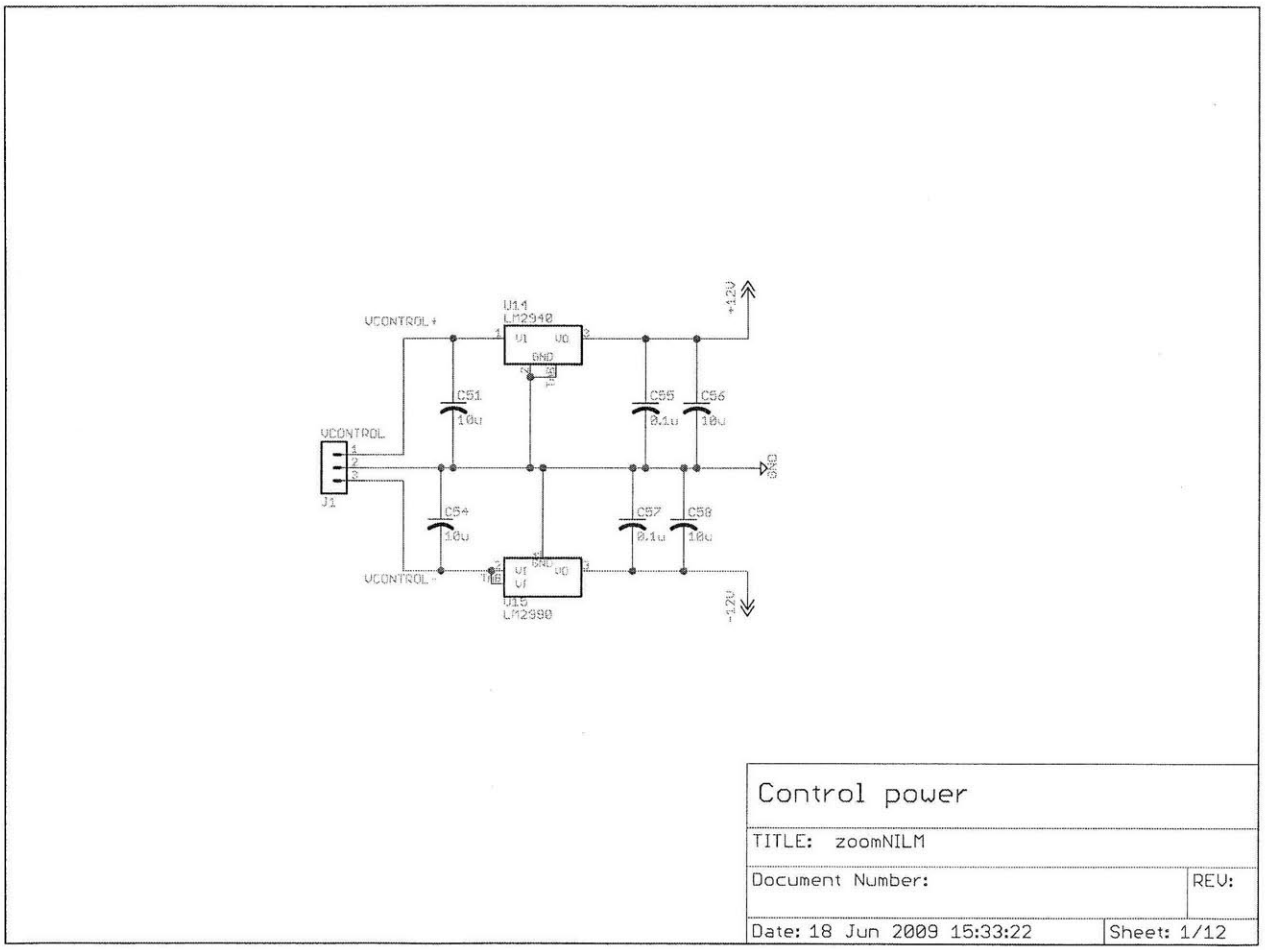


Figure A.1: Schematic of the control power

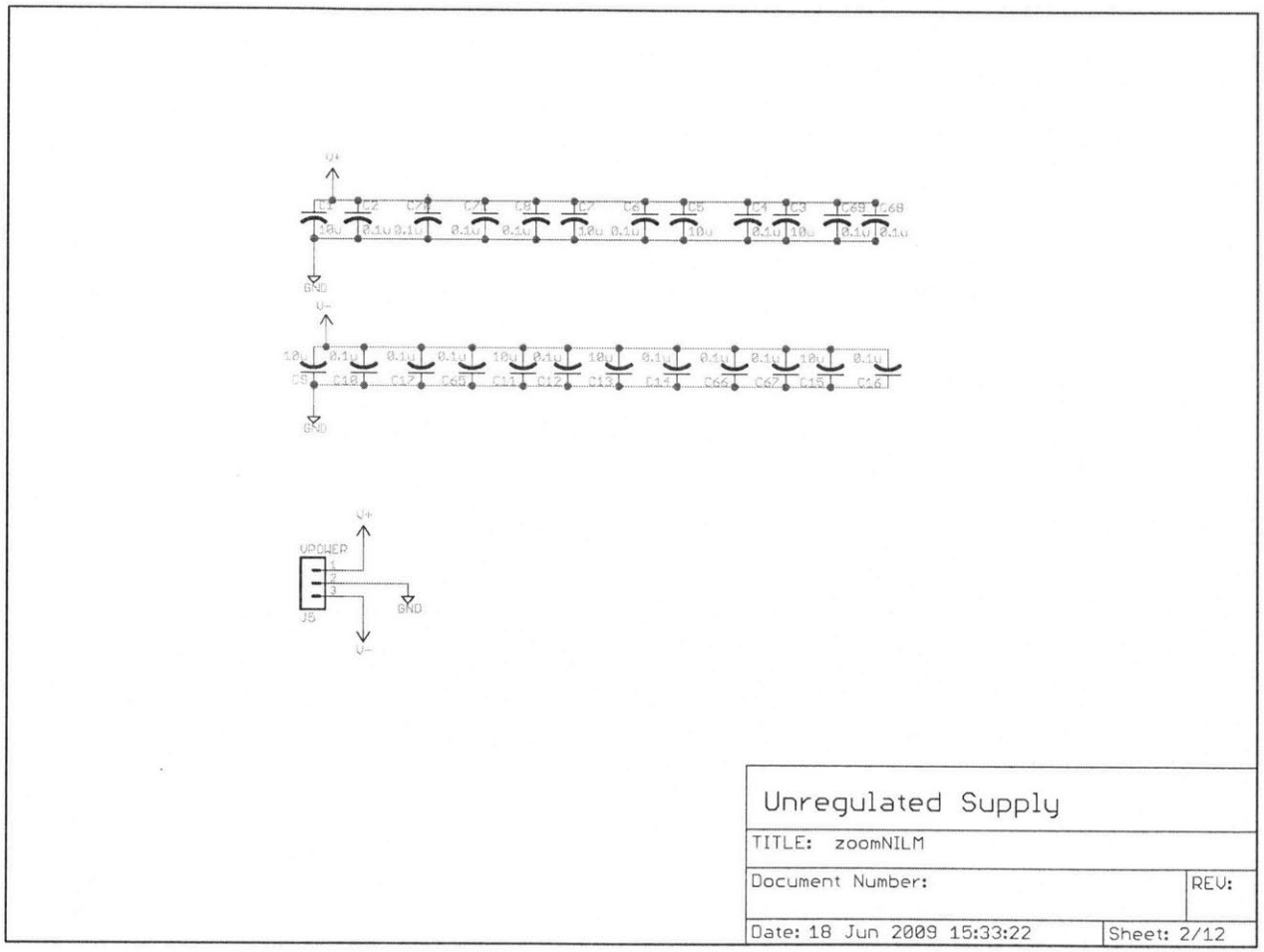


Figure A.2: Schematic of the unregulated power supply

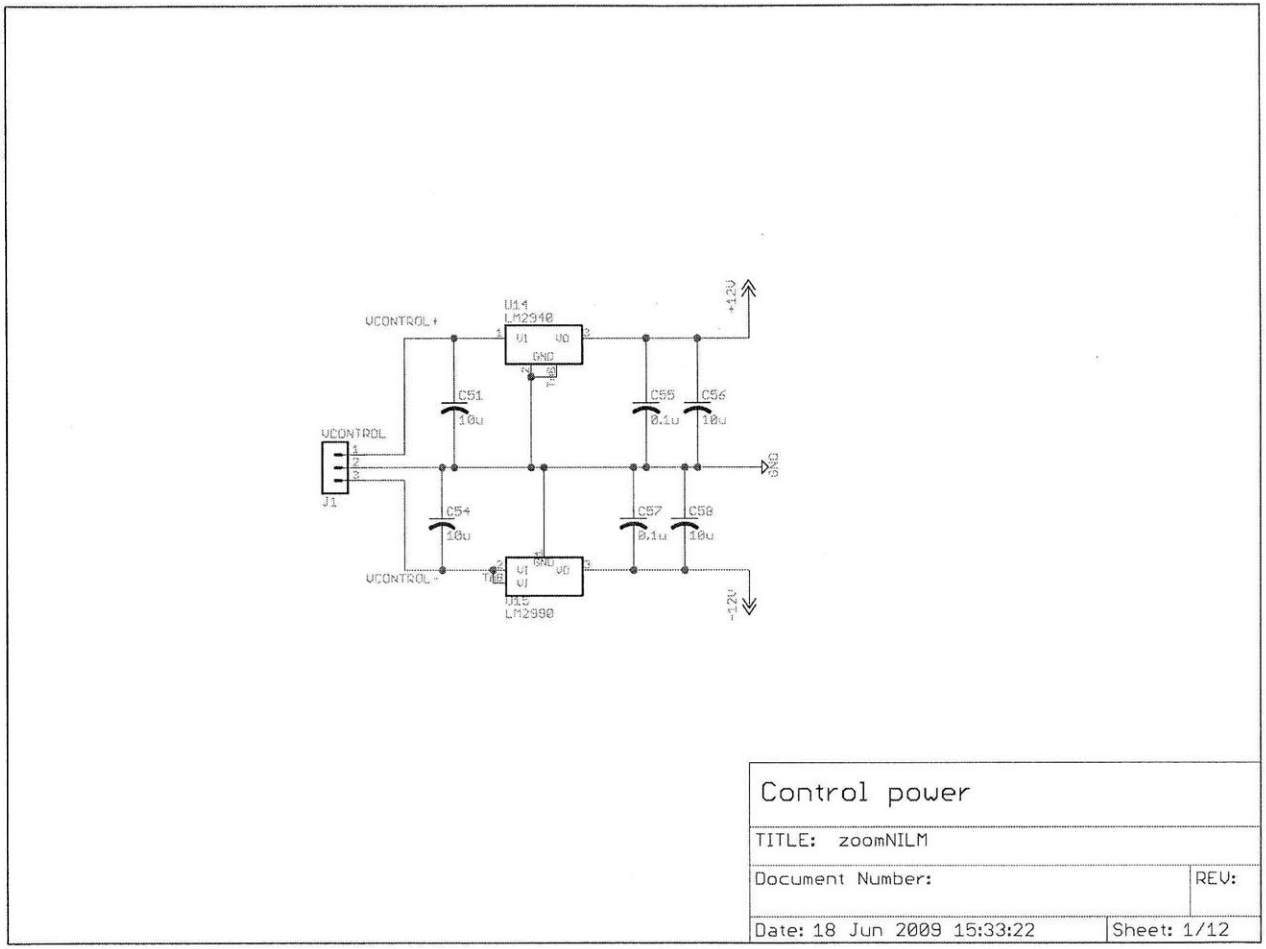


Figure A.3: Schematic of the power supply for the control circuit

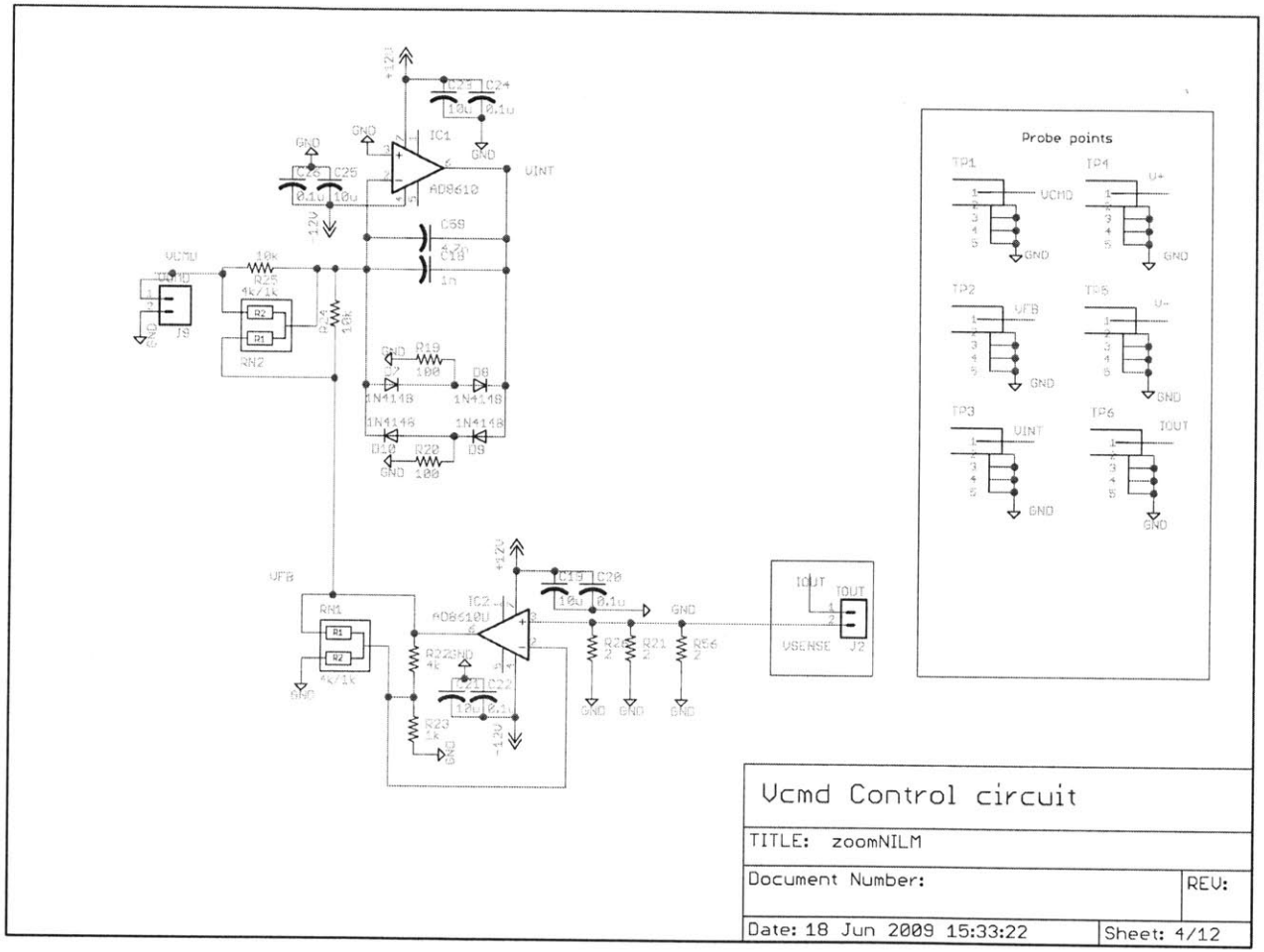


Figure A.4: Schematic of the command voltage

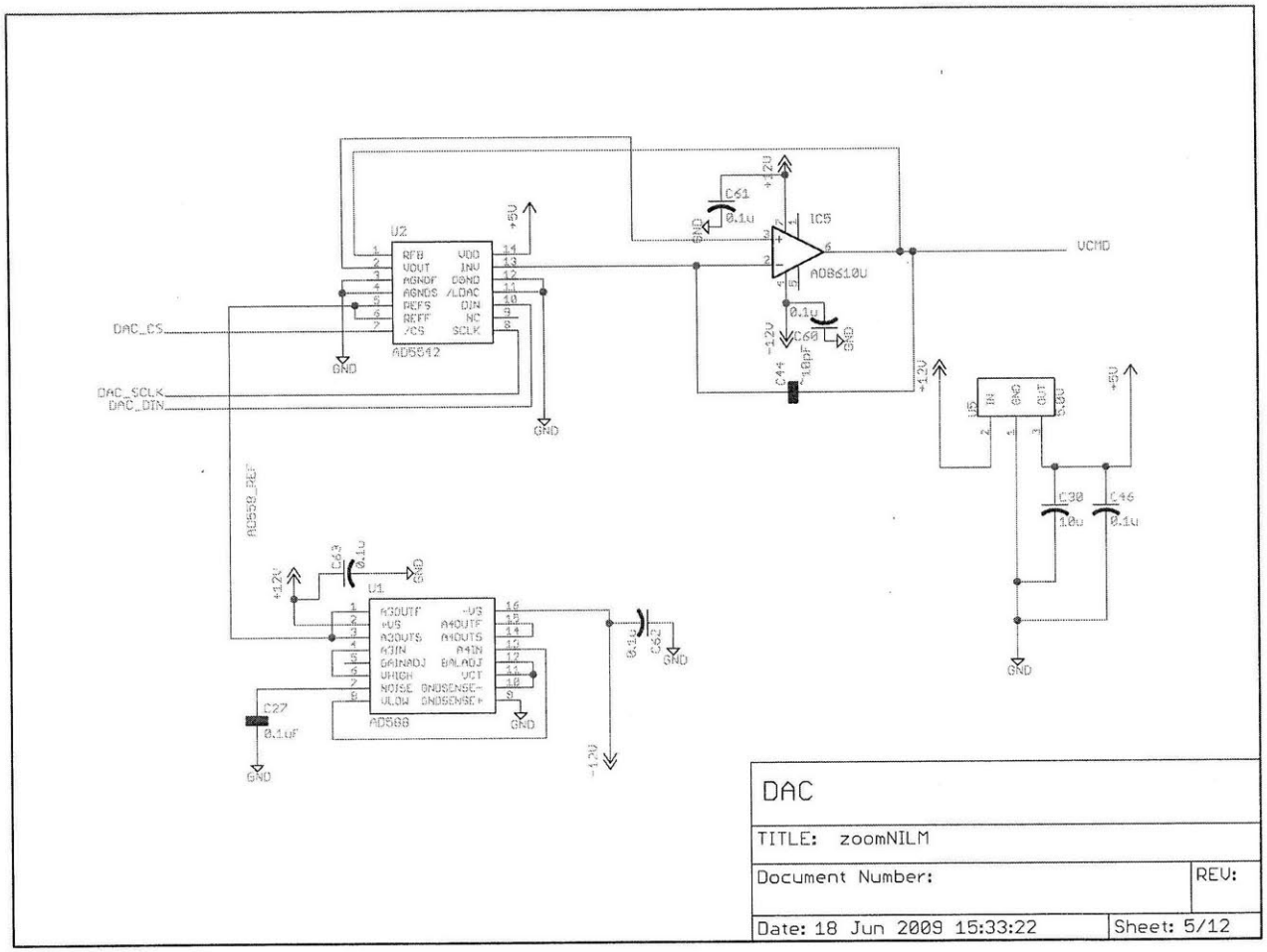


Figure A.5: Schematic of the digital-to-analog converter (DAC)

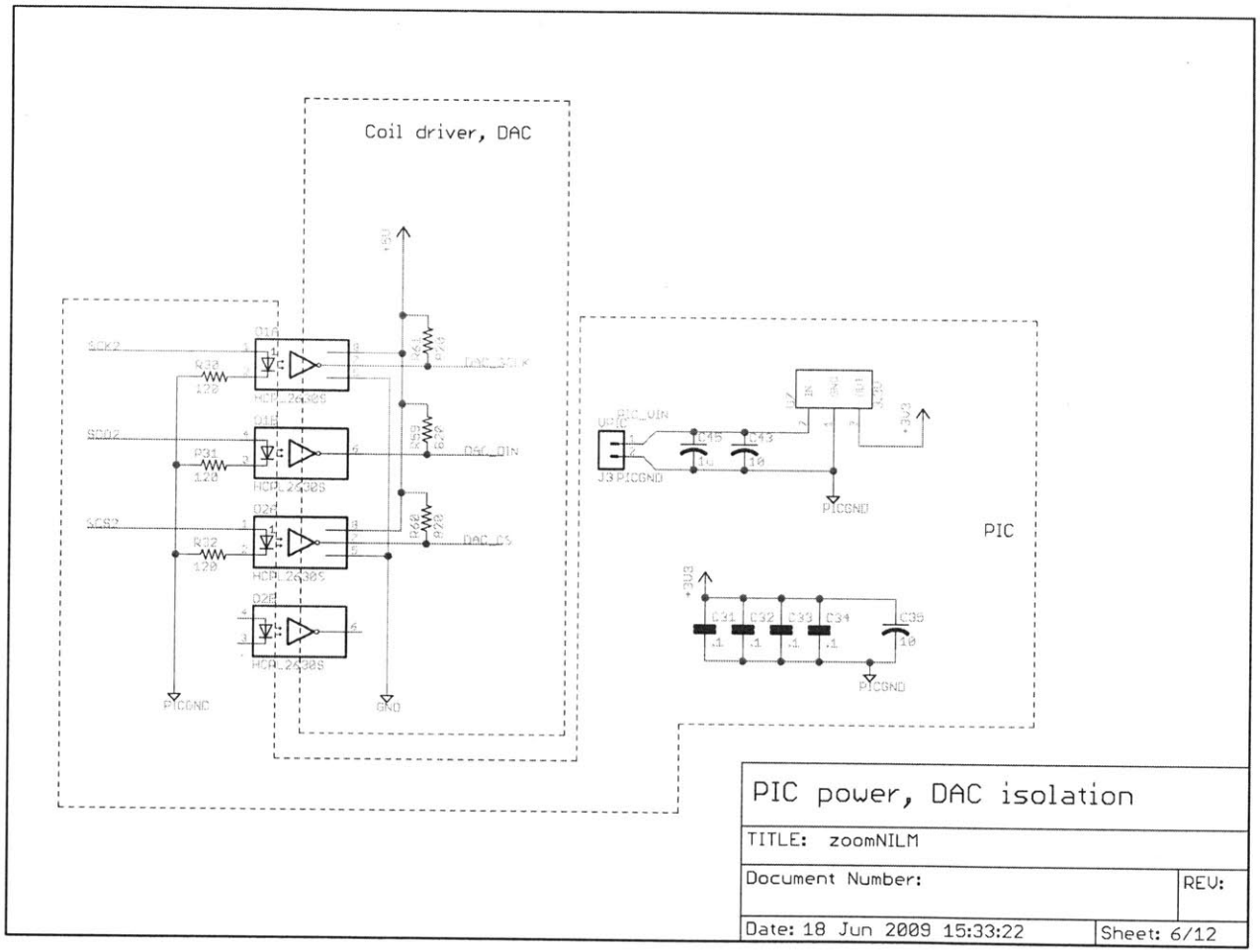


Figure A.6: Schematic of the DAC isolation circuit and the microcontroller power supply

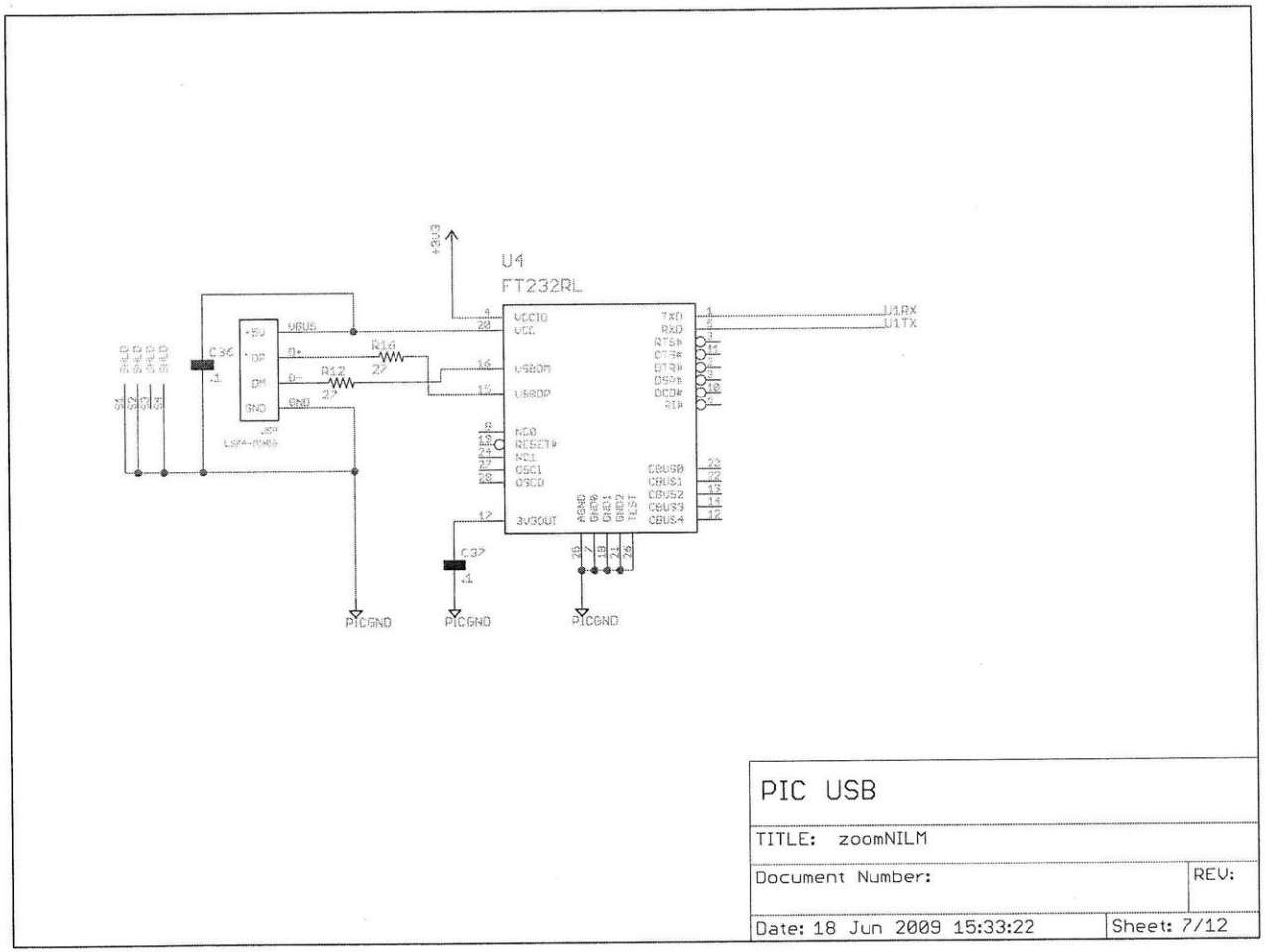


Figure A.7: Schematic of the USB peripheral

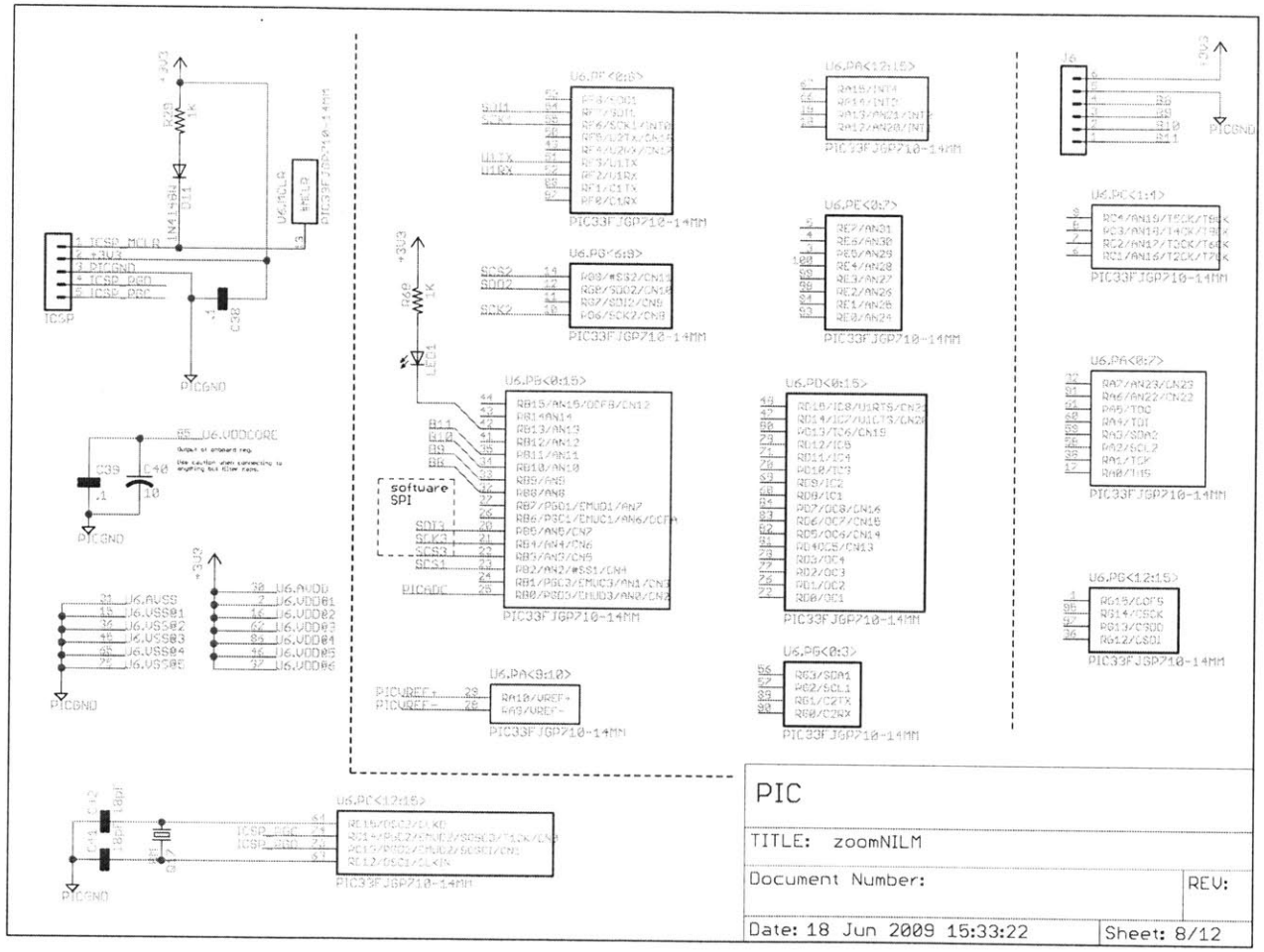


Figure A.8: Schematic of the microcontroller connection

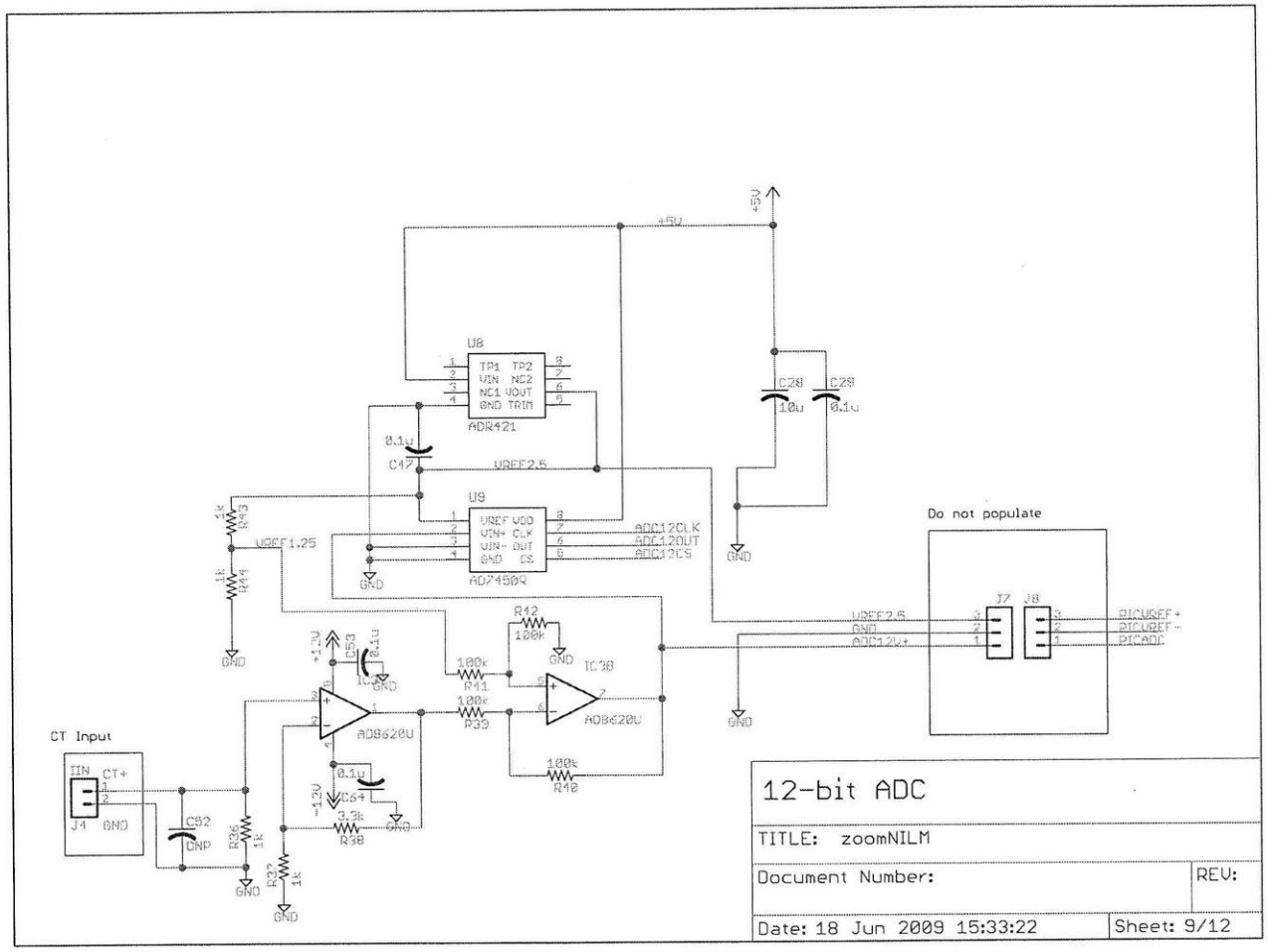


Figure A.9: Schematic of the 12-bit analog-to-digital converter (ADC)

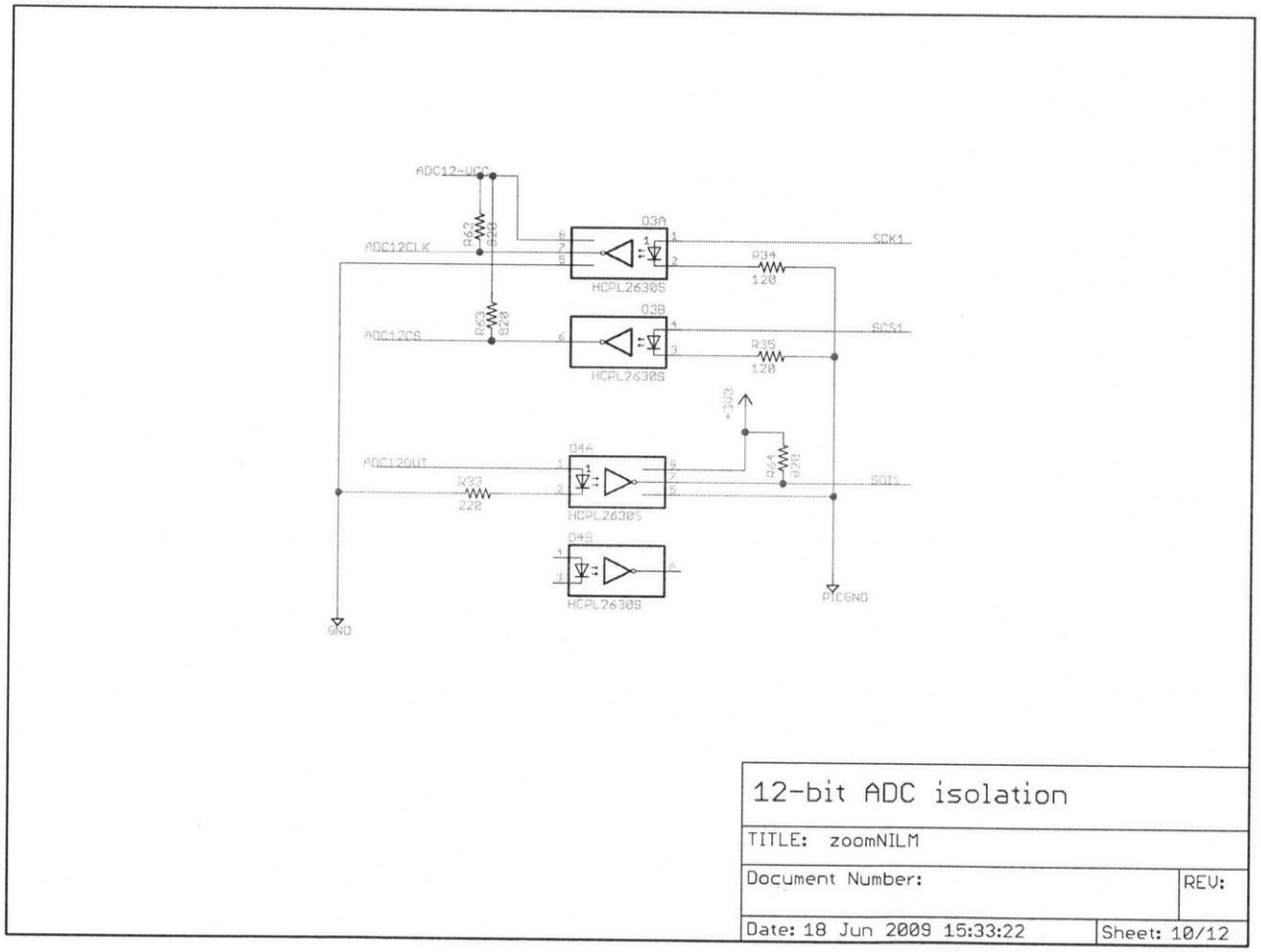


Figure A.10: Schematic of the 12-bit ADC isolation circuit

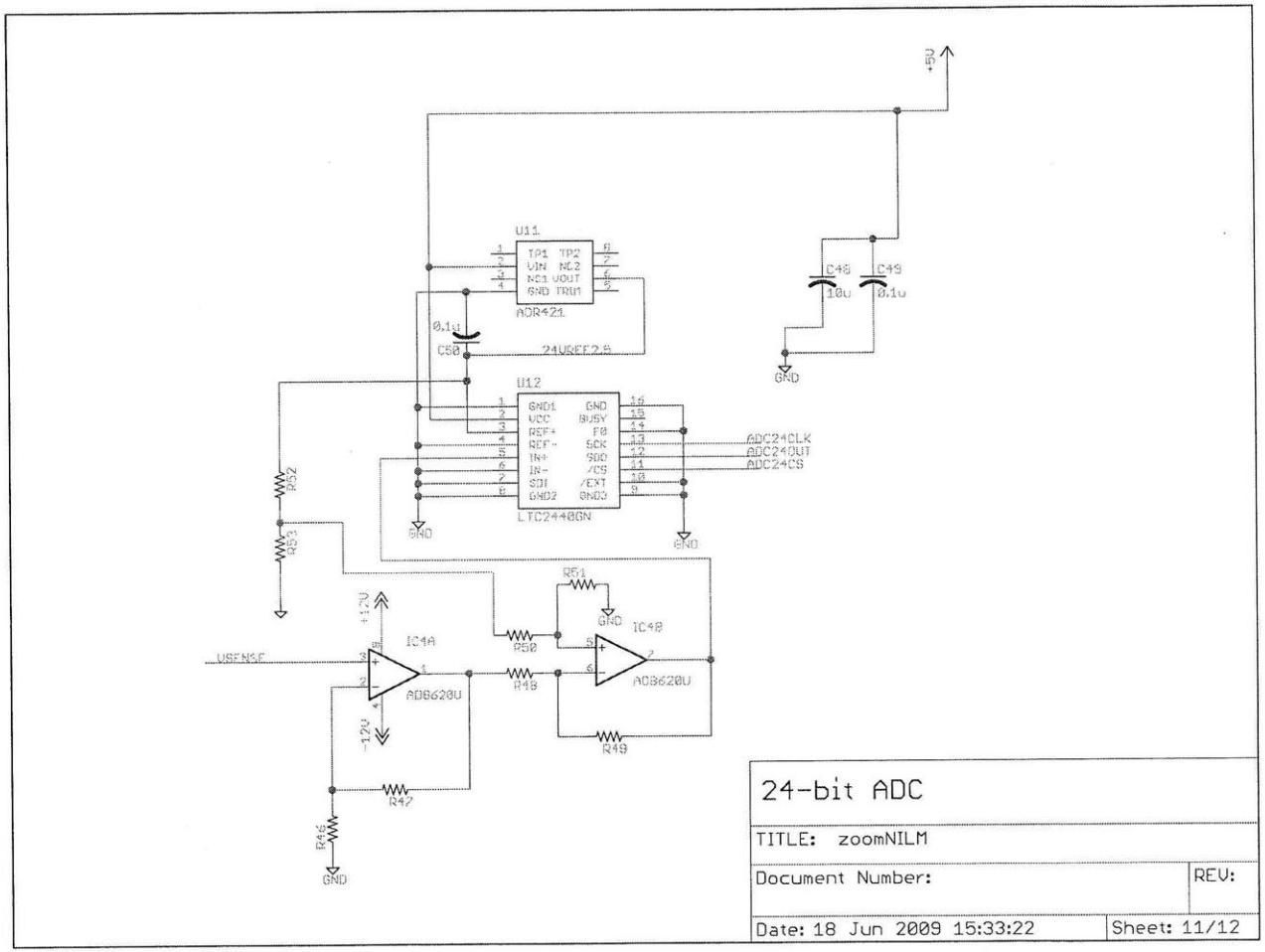


Figure A.11: Schematic of the the 24-bit ADC

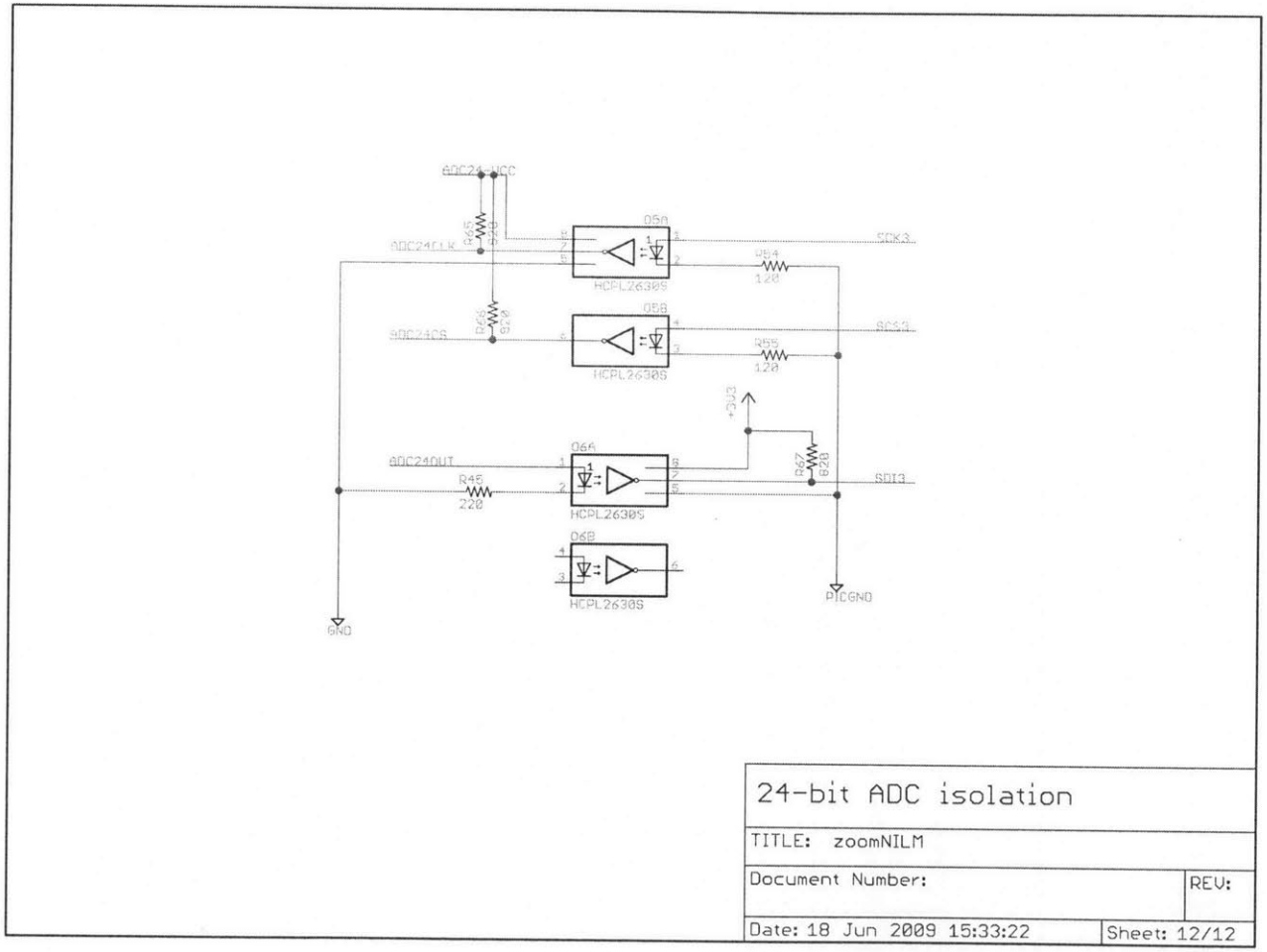


Figure A.12: Schematic of the 24-bit ADC isolation circuit

## *Appendix B*

# *Computations of weighting coefficients for the VSD estimator*

---

This section shows the computation of weighting coefficients for the vsd estimator using switching function method. The steps shown in this section can be applied to all switching functions described in Chapter 3. The key idea is to compute the coefficients of the switching function, specifically $S^0$, $S_n^{\mathrm{p}}$, and $S_n^{\mathrm{q}}$. The final coefficients can be computed by realizing the corresponding line-side current harmonic given the harmonics of the switching fuction ($n$) and dc-side current ($m$). This section summarizes the result for all the coefficients for cases.

Let recall that the dc-component of the line current is given in (3.12) as

$$I^0 = W^{00} I^{0\mathrm{dc}} + W^{0\mathrm{p}} I^{\mathrm{pdc}} + W^{0\mathrm{q}} I^{\mathrm{qdc}}$$

where $W^{00}$, $W^{0\mathrm{p}}$, and $W^{0\mathrm{q}}$ are the row vectors of the switching function coefficients. These vectors $W^{00}$, $W^{0\mathrm{p}}$, and $W^{0\mathrm{q}}$ can be written as

$$W^{00} = S^0, \tag{B.1}$$

$$W^{0\mathrm{p}} = \begin{bmatrix} -\frac{1}{2}S_1^{\mathrm{q}} & -\frac{1}{2}S_2^{\mathrm{q}} & -\frac{1}{2}S_3^{\mathrm{q}} & \cdots \end{bmatrix}, \tag{B.2}$$

and

$$W^{0\mathrm{q}} = \begin{bmatrix} \frac{1}{2}S_1^{\mathrm{p}} & \frac{1}{2}S_2^{\mathrm{p}} & \frac{1}{2}S_3^{\mathrm{p}} & \cdots \end{bmatrix}. \tag{B.3}$$

The in-phase component of the $k$th line current harmonic is given in (3.13) as

$$I_k^{\mathrm{p}} = W_k^{\mathrm{p0}} I^{\mathrm{0dc}} + W_k^{\mathrm{pp}} I^{\mathrm{pdc}} + W_k^{\mathrm{pq}} I^{\mathrm{qdc}}$$

where the quantities $W_k^{\mathrm{p0}}$, $W^{\mathrm{pp}}$, and $W^{\mathrm{pq}}$ are the row vectors of the switching function coefficients. These coefficients can be described by

$$W_k^{\mathrm{p0}} = S_k^{\mathrm{p}}. \tag{B.4}$$

$$W_k^{\mathrm{pp}} = \begin{bmatrix} w_{k,1}^{\mathrm{pp}} & w_{k,2}^{\mathrm{pp}} & w_{k,3}^{\mathrm{pp}} & \cdots & w_{k,m}^{\mathrm{pp}} & \cdots \end{bmatrix}. \tag{B.5}$$

Each coefficient of the matrix $w_{k,m}^{\mathrm{pp}}$ can be computed as

$$w_{k,m}^{\mathrm{pp}} = \begin{cases} \dfrac{1}{2}(S_{m+k}^{\mathrm{p}} + S_{k-m}^{\mathrm{p}}) & \text{for } m < k, \quad \text{(B.6a)} \\ \dfrac{1}{2}S_{m+k}^{\mathrm{p}} + S^0 & \text{for } m = k, \quad \text{(B.6b)} \\ \dfrac{1}{2}(S_{m+k}^{\mathrm{p}} - S_{m-k}^{\mathrm{p}}) & \text{for } m > k, \quad \text{(B.6c)} \end{cases}$$

where the variable $m$ represents the dc-side harmonic number, i.e. $m = 1, 2, 3, \ldots$. Similarly, the vector $W_k^{\mathrm{pq}}$ can be represented as

$$W_k^{\mathrm{pq}} = \begin{bmatrix} w_{k,1}^{\mathrm{pq}} & w_{k,2}^{\mathrm{pq}} & w_{k,3}^{\mathrm{pq}} & \cdots & w_{k,m}^{\mathrm{pq}} & \cdots \end{bmatrix}. \tag{B.7}$$

Each coefficient of the matrix $w_{k,m}^{\mathrm{pq}}$ can be computed as

$$w_{k,m}^{\mathrm{pq}} = \begin{cases} \dfrac{1}{2}(S_{m+k}^{\mathrm{q}} - S_{|m-k|}^{\mathrm{q}}) & \text{for } m \neq k, \quad \text{(B.8a)} \\ \dfrac{1}{2}S_{m+k}^{\mathrm{q}} + S^0 & \text{for } m = k. \quad \text{(B.8b)} \end{cases}$$

The quadrature component is given in (3.14) as

$$I_k^{\mathrm{q}} = W_k^{\mathrm{q0}} I^{\mathrm{0dc}} + W_k^{\mathrm{qp}} I^{\mathrm{pdc}} + W_k^{\mathrm{qq}} I^{\mathrm{qdc}},$$

where the coefficient $W_k^{\mathrm{q0}}$, $W_k^{\mathrm{qp}}$, and $W_k^{\mathrm{qq}}$ can be easily computed.

$$W_k^{\mathrm{q0}} = S_k^{\mathrm{q}}. \tag{B.9}$$

$$W_k^{\mathrm{qp}} = \begin{bmatrix} w_{k,1}^{\mathrm{qp}} & w_{k,2}^{\mathrm{qp}} & w_{k,3}^{\mathrm{qp}} & \cdots & w_{k,m}^{\mathrm{qp}} & \cdots \end{bmatrix}. \tag{B.10}$$

Each coefficient of the matrix $w_{k,m}^{\mathrm{qp}}$ can be computed as

$$w_{k,m}^{\mathrm{qp}} = \begin{cases} \dfrac{1}{2}(S_{m+k}^{\mathrm{q}} + S_{|m-k|}^{\mathrm{q}}) & \text{for } m \neq k, \quad \text{(B.11a)} \\ \dfrac{1}{2} S_{m+k}^{\mathrm{q}} - S^0 & \text{for } m = k. \quad \text{(B.11b)} \end{cases}$$

Similarly, the vector $W_k^{\mathrm{qq}}$ can be represented as

$$W_k^{\mathrm{qq}} = \begin{bmatrix} w_{k,1}^{\mathrm{qq}} & w_{k,2}^{\mathrm{qq}} & w_{k,3}^{\mathrm{qq}} & \cdots & w_{k,m}^{\mathrm{qq}} & \cdots \end{bmatrix}. \tag{B.12}$$

Each coefficient of the matrix $w_{k,m}^{\mathrm{qq}}$ can be computed as

$$w_{k,m}^{\mathrm{qq}} = \begin{cases} -\dfrac{1}{2}(S_{m+k}^{\mathrm{p}} - S_{k-m}^{\mathrm{p}}) & \text{for } m < k, \quad \text{(B.13a)} \\ -\dfrac{1}{2} S_{m+k}^{\mathrm{p}} - S^0 & \text{for } m = k, \quad \text{(B.13b)} \\ -\dfrac{1}{2}(S_{m+k}^{\mathrm{p}} + S_{m-k}^{\mathrm{p}}) & \text{for } m > k. \quad \text{(B.13c)} \end{cases}$$

# *Appendix C*

# *Waveform-Based Estimator Program*

---

The waveform-based estimator program is summarized in this appendix. This program is written in GP/PARI mathematical language. The program used GP/PARI version 2.3.5 from [48]. All codes have been successfully complied using "gcc (Ubuntu 4.3.3-5ubuntu4) 4.3.3".

This program generates the estimator for the fundamental harmonic using a subset of higher harmonics in the following form,

$$\widehat{I}_1 = \sum_{m=1}^{2K} (c_m I_m). \tag{C.1}$$

The number $2K$ represents the number of input harmonics for the estimator. The input harmonics are always used with the complex conjugates. The coefficient $c_m$ is the complex coefficient for each harmonic. The current harmonic $I_m$ represents the input harmonics. In order to compute the estimator, the user must specify the following parameters:

1. regions of zero-current,

2. symmetry points in the waveform,

3. input harmonics, and

4. non-zero harmonics listed according to their magnitude

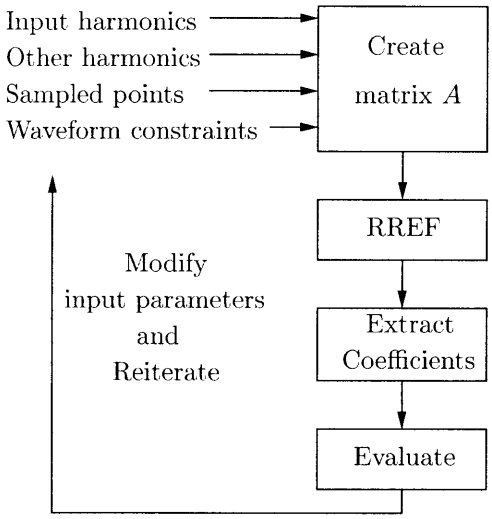


Figure C.1: Pseudo-code for the waveform-based estimator

The program is designed to perform three steps:

1. set up a matrix $A$,

2. perform the RREF algorithm, and

3. extract the coefficients.

The program does not perform the evaluation step in the four-step process. The user must evaluate and reiterate program manually. The program can be summarized in a flow diagram in Figure C.1.

```
/*
 * Name: runscript1.gp
 * Input: parameter.gp -- specify necessary waveform constraint
 * Main program:
 *     nfcreatematrix.gp -- create coefficient matrix A
 *     generateVector.gp -- list the order of non-zero harmonics
 *                          not including the input harmonics
 *     estimator.gp      -- compute the estimator
 */
{
/* load necessary libraries */
install("nfmul","D0,G,D0,G,LL","nfmul","./nfmul.gp.so");
install("init_nfmul","v","init_nfmul","./nfmul.gp.so");

install("getleadingnonzero","D0,G,","getleadingnonzero", \
        "./getleadingnonzero.gp.so");
install("init_getleadingnonzero","v","init_getleadingnonzero", \
        "./getleadingnonzero.gp.so") ;

install("nfcreatematrix","LD0,G,D0,G,D0,G,","nfcreatematrix", \
        "./nfcreatematrix.gp.so");
install("init_nfcreatematrix","v","init_nfcreatematrix", \
        "./nfcreatematrix.gp.so");

install("generateVector","LD0,G,LL","generateVector", \
        "./generateVector.gp.so");
install("init_generateVector","v","init_generateVector", \
        "./generateVector.gp.so");

/* these libraries has not been converted into c program */
read("nfrref.gp");
read("estimator.gp");

/* input parameters */
read("parameter.gp");

/* rounding threshold */
MYTHRES = 1E-23;
/* create the matrix A */
A = nfcreatematrix(N,Vz,Ve,Vo);
/* generate the vector according to their importance */
```

```
H = generateVector(N,Set(K),Opt,Hx);
/* compute the estimator */
Q1 = estimator(N,K,H,A,REDUCED_MATRIX,MULTHRESHOLD);
print("done");

/* for scripting purpose */
system("echo \"test\" > ./flag");
/* convert into the floating point */
r0 = exp(2*Pi*I/N);
gout = substpol(vecextract(lift(Q1), \
                concat([Str(-2*matsize(K)[2]), ".."])),x,r0);

/* saving the coefficient into file */
str1 = concat([Str(N), ", ", Str(matsize(K)[2])]);

for(ind = 1, matsize(gout)[2],
    if(abs(real(gout[ind])) > MYTHRES, \
       str2 = Str(real(gout[ind]));, str2 = "0.0");
    if(abs(imag(gout[ind])) > MYTHRES, \
       str3 = Str(imag(gout[ind]));, str3 = "0.0");
    str1 = concat([str1, ", ", str2, ", ", str3]);
);

write(OUTPUTFILE,str1);
write(CONFIGFILE,"----------------------------");
write(CONFIGFILE,OUTPUTFILE);
system(concat(["cat ", "parameter.gp", ">>", CONFIGFILE]));
system("rm -f ./flag");
}
```

```
/*
 * Name: nfcreatematrix.gp
 * Function: create matrix A in a necessary according to the
 * the dimensions given below
 *
 * N  = number of samples per line cycle
 * Vz = vector of zero sample points in electrical degree
 *      i.e. [0, 60, 120, 180] for only first half of the cycle
 * Ve = vector of symmetry, expecting two columns
 * Vo = vector of odd-symmetry, expecting two columns
 */

nfcreatematrix(N:small,Vz,Ve,Vo)=
{
local(poly_temp:pol,ind1:small,ind2:small);
local(Nz:vec,Ns:vec,Ns1:vec,Ns2:vec,No:vec);
local(Vtemp:vec,A:vec,numCols:small,numRows:small,unpaired:bool);
local(row:small, col:small, Offset1:small);

/*
 * Let calculate the actual data points that's zero
 *
 * Nz should be in the form of indeces
 * Ns should be in the form of indeces
 * No should be in the form of indeces
 */
Vtemp = floor(Mat(Vz)*N/360);
Nz = [];
for(ind1 = 1,matsize(Vtemp)[1],
    Nz = concat(Nz,vector(Vtemp[ind1,2]-Vtemp[ind1,1]+1,\
                          i,i+Vtemp[ind1,1]-1));
);
/* convert the pair to the actual time index */
Vtemp = floor(Mat(Ve)*N/360);
Ns1 = [];
Ns2 = [];
for(ind1 = 1, matsize(Vtemp)[1],
    Ns1 = concat(Ns1,vector(Vtemp[ind1,2]-Vtemp[ind1,1]+1,\
                            i,i+Vtemp[ind1,1]-1));
    Ns2 = concat(Ns2,vector(Vtemp[ind1,2]-Vtemp[ind1,1]+1,\
                            i,i+Vtemp[ind1,3]-1));
```

```
);

Ns = matrix(length(Ns1),2); Ns[,1] = Ns1~; Ns[,2] = Ns2~;
Vtemp = floor(Mat(Vo)*N/360);
Ns1 = []; Ns2 = [];
for(ind1 = 1, matsize(Vtemp)[1],
    Ns1 = concat(Ns1,vector(Vtemp[ind1,2]-Vtemp[ind1,1]+1,\
                            i,i+Vtemp[ind1,1]-1));
    Ns2 = concat(Ns2,vector(Vtemp[ind1,2]-Vtemp[ind1,1]+1,\
                            i,i+Vtemp[ind1,3]-1));
);

No = matrix(length(Ns1),2);
No[,1] = Ns1~;
No[,2] = Ns2~;

/* debug */
print(concat(["Generating matrix: N = ",Str(N), " Nz: ", \
              Str(matsize(Nz)[2]), " Nsym: ", \
              Str(matsize(Ns)[1]), " Nodd: ", Str(matsize(No)[1])]));

/* prepare the data */
poly_temp = polcyclo(N);
/* number of harmonics are N-1, ignoring the DC value for now */
numCols=floor(N);
/* number of constraints are just number of zeroes and symmetry */
numRows=floor(length(Nz)+matsize(No)[1]+matsize(Ns)[1]);
/* create the matrix holder */
A = matrix(numRows,numCols);
/* generate a list of possible coefficients */
coeffs=vector(N+1,j,Mod(x^(j-1),poly_temp));
/* check if number of columns is odd */
unpaired=(lift(Mod(numCols,2))==1);

/* do the zero constraint first */
for(row:small=1,length(Nz),
    /* find the right index */
    ind1=lift(Mod(Nz[row],N))+1;
    /* distributing the coefficients
     * we do two at a time because the structure is
     * [1 -1  2 -2  3 -3 ... ]
```

```
     * The reduction of even harmonics can be done in the later part.
     */
    for(col = 1,floor(numCols/2),
        A[row,2*col-1] = coeffs[ind1];
        if(2*col != numCols,
           A[row,2*col] = coeffs[N-ind1+2];,
           A[row,2*col] = coeffs[1];
        );
        /* update the index */
        ind1+= Nz[row];
        /* perform modulo operation if index exceeds N */
        if(ind1>N,ind1-=N;);
    );

    if(unpaired,
       ind1 = 1;
       A[row,numCols]=coeffs[ind1];
    );
);
Offset1 = length(Nz);
/* fill up coefficients for the even-symmtry constraints */
for(row = 1, matsize(Ns)[1],
    /* find the right index */
    ind1=lift(Mod(Ns[row,1],N))+1;
    ind2=lift(Mod(Ns[row,2],N))+1;
    for(col = 1, floor(numCols/2),
        A[row + Offset1,2*col-1] = coeffs[ind1] - coeffs[ind2];
        if(2*col != numCols,
           A[row + Offset1,2*col] = coeffs[N-ind1+2] - \
                                    coeffs[N-ind2+2];,
           A[row + Offset1,2*col] = 0;
        );
        /* update the index */
        ind1+= Ns[row,1];
        ind2+= Ns[row,2];
        /* perform modulo operation if index exceeds N */
        if(ind1>N, ind1-=N);
        if(ind2>N, ind2-=N);
    );
    if(unpaired,
       ind1=lift(Mod(Ns[row,1]*(2*numCols-1),N))+1;
```

```
        ind2=lift(Mod(Ns[row,2]*(2*numCols-1),N))+1;
        A[row + Offset1,numCols] = 0;
    );
);

Offset1 = length(Nz)+matsize(Ns)[1];
/* fill up coefficients for the odd-symmtry constraints */
for(row = 1, matsize(No)[1],
    /* find the right index */
    ind1=lift(Mod(No[row,1],N))+1;
    ind2=lift(Mod(No[row,2],N))+1;

    for(col = 1, floor(numCols/2),
        A[row + Offset1,2*col-1] = coeffs[ind1] + coeffs[ind2];
        if(2*col != numCols,
           A[row + Offset1,2*col] = coeffs[N-ind1+2] + \
                                    coeffs[N-ind2+2];,
           A[row + Offset1,2*col] = coeffs[1] + coeffs[1];
        );

        /* update the index */
        ind1+= No[row,1];
        ind2+= No[row,2];
        /* perform modulo operation if index exceeds N */
        if(ind1>N, ind1-=N);
        if(ind2>N, ind2-=N);
    );

    if(unpaired,
       ind1=lift(Mod(No[row,1]*(2*numCols-1),N))+1;
       ind2=lift(Mod(No[row,2]*(2*numCols-1),N))+1;
       A[row + Offset1,numCols] = coeffs[1] + coeffs[1];
    );
);

/* return the matrix */
return(A);
}
```

```
/*
 * Name: generateVector.gp
 * Function: generate an index vector that should take care
 *           of the redundancy in the matrix
 */

generateVector(N:small,KnownH,Opt:small,Hx:small)=
{
local(ind, zx, v1, v2);
v1 = vector(floor(N/2),i,i);
/* index vector */
zx = vector(floor(N/2));

/* vsd case: ignore tripplen and even harmonic */
if(Opt == 0,
   for(ind = 1, floor(N/2),
       if(lift(Mod(v1[ind],2))==0 || lift(Mod(v1[ind],3))== 0,
          zx[ind] = 0;,
          if(setsearch(KnownH,v1[ind]),
             zx[ind] = -N;,
             zx[ind] = N-v1[ind];
          );
       );
   );
);

/* single phase full wave rectifier case:
 * contain only odd harmonic
 * push priority of the even harmonics to the end
 */
if(Opt == 1,
   for(ind = 1, floor(N/2),
       if(lift(Mod(v1[ind],2))==0,
          zx[ind] = -v1[ind];,
          if(setsearch(KnownH,v1[ind]),
             zx[ind] = -N;,
             zx[ind] = N-v1[ind];
          );
      );
   );
```

```
);

/* Dimmer case:
 * contain only odd harmonic
 * push priority of the even harmonics to the end
 */
if(Opt == 2,
   for(ind = 1, floor(N/2),
       if(setsearch(KnownH,v1[ind]),
          x[ind] = -10*N - v1[ind];,
          if(lift(Mod(v1[ind],2))==1 && v1[ind] < Hx,
             x[ind] = N-v1[ind];,
             zx[ind] = -v1[ind];
          );
       );
   );
);

zx = vecsort(zx,,5);
v2 = vector(N,i,i);
for(ind = 1, length(zx),
    v2[2*ind-1] = 2*zx[ind]-1;
    v2[2*ind]   = 2*zx[ind];
);

return(v2);
}
```

```
/*************************************************
 ** function: estimator(N,K,A,ReduceMatrixFlag,MULTHRESHOLD)
 ** descriptoin: generate the coefficeints for the
 **    vsd estimator given the parameters
 **    N = number of constraints,
 **    K = list of harmonics
 **    H = list of harmonics to be eliminated in
 **        decreasing order of importance
 **    A = the Fourier constraint matrix
 **    ReduceMatrixFlag = flag to reduce matrix size
 **    MULTHRESHOLD = threshold for using custom nfmul.gp.c
 *************************************************/
estimator(N:small,K:vec,H:vec,A, \
          ReduceMatrixFlag:small,MULTHRESHOLD:small) =
{

local(B,R,Rx,Q,Gx,extractColumn);
local(columnIndex,rowIndex:small,inSize,ind:small);

/* check the corner case */
if(length(setintersect(Set(K),Set([0, N]))) != 0,
   error("estimator::Undertermined case for using \
          DC harmonic as a dependent variable");
);

print(concat(["Prepare matrix: N = ", \
              Str(N), ", K = ", Str(length(K))]));

/* reduce row echelon form */
OPTION_ROW_ECHELON_FORM = 1;
/* create a target index
 * This vector contains the indices of the target harmonics
 * [1 -1  2 -2 ... ] translates to
 * [1  2  3  4 ... ]
 */
targetHarmonic = vector(2*length(K));
for(ind = 1, length(K),
    targetHarmonic[2*ind-1] = 2*K[ind]-1;
    targetHarmonic[2*ind]   = 2*K[ind];
);
```

```
if(length(K) > 0,
   extractColumn = matrix(matsize(A)[1],2*length(K));
   for(ind = 1, length(targetHarmonic),
       extractColumn[,ind] = A[,targetHarmonic[ind]];
   );
);

/* make the matrix a square matrix */
if(ReduceMatrixFlag == 1, B=matrix(matsize(A)[1],matsize(A)[1]);,
   /* just follow the H vector */
   if(ReduceMatrixFlag == 2, B=matrix(matsize(A)[1],matsize(H)[2]);,
      /* concat */
      B=matrix(matsize(A)[1],matsize(A)[2]-length(targetHarmonic));
   );
);

/* copy the coefficient over to matrix B */
for(ind=1,matsize(B)[2],B[,ind] = A[,H[ind]];);

/* append the input harmonics to the end */
if(length(K) > 0 && ReduceMatrixFlag != 2, \
   B = concat(B,extractColumn));
print(concat(["Perform rref: ", Str(N), \
              " Total: ", Str(matsize(B)[1]), " rows"]));

/* RREF for cyclotomic matrix */
Q = nfrref(B,OPTION_ROW_ECHELON_FORM,MULTHRESHOLD,N,K,H);

Q[1,] = Q[1,]/Q[1,1];
return(Q[1,]);
}
```

```
\*
 * Name: nfrref.gp
 * Function: perform Gaussian elimination method
 *           to get the reduced row Echelon form
 *\
nfrref(A,OptionRowEchelonForm:small,OP_THRESH:small,N:small,KH,H)=
{
local(numRows:small,numCols:small,colIndex:small);
local(rowIndex:small,rowCounter:small,found:small);
local(M,temp,pivotVal,k:small,lNeigh);

M=A;
numRows=matsize(A)[1];
numCols=matsize(A)[2];
colIndex=1;
rowCounter=1;

numColsx = numCols;
swapCol = numCols - 2*matsize(KH)[2];
HTemp = H;
swapFlag = 0;

system("rm -f swapFlag.log error.log hVector.log");

while((colIndex<=numColsx) && (rowCounter<=numRows),
    print(concat(["Column:",Str(colIndex)]));
    rowIndex=rowCounter;
    found=0;
    while(rowIndex<=numRows && !found,
        if(M[rowIndex,colIndex]==0,rowIndex++;,found=1;);
    ); /* end while */

    if(found,
        if(rowCounter!=rowIndex,
            temp=M[rowIndex,];
            M[rowIndex,]=M[rowCounter,];
            M[rowCounter,]=temp;
        ); /* end if */

        pivotVal=1/M[rowCounter,colIndex];
        for(j=colIndex,numCols,
```

```
            M[rowCounter,j] = nfmul(M[rowCounter,j],\
                                    pivotVal,OP_THRESH,N);
        );

        /* eliminate every row */
        for(k=1,numRows,
            if((OptionRowEchelonForm && \
                ((k == 1 && rowCounter != 1) || k > rowCounter)) || \
                (!OptionRowEchelonForm && k!=rowCounter),

                lNeigh=M[k,colIndex];

                for(j=colIndex,numCols,
                    M[k,j]=M[k,j]-nfmul(M[rowCounter,j],\
                                        lNeigh,OP_THRESH,N);
                );
            ); /* end if */
        ); /* end for */
        rowCounter++;,
        /* need to swap column */
        tempCol = M[,colIndex];
        tempH = HTemp[colIndex];
        for(p = colIndex + 1, swapCol,
            M[,p-1] = M[,p];
            HTemp[p-1] = HTemp[p];
        );
        M[,swapCol] = tempCol;
        HTemp[swapCol] = tempH;
        swapCol--;
        colIndex--;
        swapFlag = 1;
    ); /* end if(found,..) */
    colIndex++;
);

return(M);
}
```

```
/*-*- compile-command:
"/usr/bin/gcc -c -o nfmul.gp.o -O3 -Wall -fno-strict-aliasing \
 -fomit-frame-pointer -D_REENTRANT -fPIC -I"/usr/local/include" \
 nfmul.gp.c &&
 /usr/bin/gcc -o nfmul.gp.so -shared -O3 -Wall -fno-strict-aliasing \
 -fomit-frame-pointer -D_REENTRANT -fPIC -Wl,-shared nfmul.gp.o
 -lc -lm -L"/usr/local/lib"
-lpari";
-*-*/
#include <pari/pari.h>
/*
GP;install("nfmul","D0,G,D0,G,LL","nfmul","./nfmul.gp.so");
GP;install("init_nfmul","v","init_nfmul","./nfmul.gp.so");
*/
GEN nfmul(GEN a, GEN b,long NUM_OP_THRESHOLD, long N);
void init_nfmul(void);
/*End of prototype*/

void init_nfmul(void)
{
/*
  pari_sp ltop = avma;
  avma = ltop;
 */
  return;
}

GEN nfmul(GEN a, GEN b,long NUM_OP_THRESHOLD, long N)
{
  GEN t, x,y, dt,dx,dy,X, z = cgetg(3,t_POLMOD);
  GEN inputshort, inputlong, coefftemp;
  int index, cx=0, cy=0,count,target;
  int maxterm,foundOddX=0,foundEvenX=0,foundOddY=0,foundEvenY=0;
  int *indexshort;
  GEN *coeffshort, *outputcoeff;
  long v;
  pari_sp ltop;

  x = gel(a,2);
  y = gel(b,2);
  X = gel(a,1);
```

```
if(isexactzero(a) || isexactzero(b)){
  return(gen_0);
}

if(typ(x) == t_INT || typ(y) == t_INT){
  return(gmul(a,b));
}

maxterm = lg(x) + lg(y) - 5;
if(maxterm > N){
  maxterm = N;
}

for(index = 2; index < lg(x); index++){
  if(!isexactzero(gel(x,index))){
      cx++;
      if(index&1)
          foundOddX=1;
      else
          foundEvenX=1;
  }
}

for(index = 2; index < lg(y); index++){
    if(!isexactzero(gel(y,index))){
        cy++;
        if(index&1)
            foundOddY=1;
        else
            foundEvenY=1;
    }
}

if(cx*cy > NUM_OP_THRESHOLD){
    if((foundOddX ^ foundEvenX)&(foundOddY ^ foundEvenY)){
        dx=cgetg(((lg(x)-3)>>1)+3,t_POL);
        dy=cgetg(((lg(y)-3)>>1)+3,t_POL);
        dx[1]=x[1];
        dy[1]=y[1];
        if(foundEvenX){
```

```
            for(index=2;index<lg(dx);index++)
                dx[index]=x[(index<<1)-2];
        }
        else{
            for(index=2;index<lg(dx);index++)
                dx[index]=x[(index<<1)-1];
        }
        if(foundEvenY){
            for(index=2;index<lg(dy);index++)
                dy[index]=y[(index<<1)-2];
        }
        else{
            for(index=2;index<lg(dy);index++)
                dy[index]=y[(index<<1)-1];
        }

        dt=RgX_mul(dx,dy);
        count=foundOddX+foundOddY;
        t=cgetg((lg(dt)<<1)-3+count,t_POL);

        t[1]=dt[1];
        for(index=0;index<count;index++)
            t[index+2]=gen_0;

        for(index=0;index<lg(dt)-3;index++){
            target=(index<<1)+2+count;
            t[target]=dt[index+2];
            t[target+1]=gen_0;
        }
        t[lg(t)-1]=dt[lg(dt)-1];
    }
    else{
        t = RgX_mul(x, y);
    }
}
else{
    outputcoeff = (GEN *)(malloc(maxterm*sizeof(GEN)));
    if(cx < cy){
        inputshort = x;
        inputlong = y;
    }
```

```
else{
    inputshort = y;
    inputlong = x;
    index = cx;
    cx = cy;
    cy = index;
}
indexshort = (int *)malloc(cx*sizeof(int));
coeffshort = (GEN *)malloc(cx*sizeof(GEN));

count=0;
for(index = 2; index < lg(inputshort); index++)
    if(!isexactzero(gel(inputshort,index))){
        indexshort[count] = index;
        coeffshort[count] = gel(inputshort,index);
        count++;
    }

for(index = 0; index < maxterm; index++)
    outputcoeff[index] = gen_0;
for(index = 2; index < lg(inputlong); index++)
    if((coefftemp = gel(inputlong,index))){
        for(count=0;count<cx;count++){
            target=(indexshort[count]+index-4) % N;
            outputcoeff[target] = gadd(outputcoeff[target],
                                       gmul(coeffshort[count],
                                            coefftemp));
        }
    }
maxterm--;

while(maxterm >= 0 && isexactzero(outputcoeff[maxterm]))
    maxterm--;

t = cgetg(maxterm+3,t_POL);
t[1] = x[1];
for(index = 0; index <= maxterm; index++)
      gel(t,index+2) = outputcoeff[index];

free(outputcoeff);
free(indexshort);
```

```
      free(coeffshort);
   }

   gel(z,1) = gcopy(X);
   ltop = avma;

   if(typ(t) == t_POL  && (v = varn(X)) == varn(t) &&
      lg(t) >= lg(X)){
       gel(z,2) = gerepileupto(ltop, RgX_divrem(t, X, ONLY_REM));
   }
   else{
      gel(z,2) = t;
   }
   return z;
}
```

```
/*
 * Name: getleadingnonzero.gp
 * Function: get the leading non-zero element in the row
 */
getleadingnonzero(v)=
{
for(i=1,length(v),
    if(v[i] != 0,
        return(v[i])
    );
);
return(1);
}
```

```
/*
 * sweeping the coefficient N for a single file
 */
{
/* loading custom functions */
MYID = "DIMMER";
EULER_LIMIT = 400;
MINIMUM_N = 60;
MAXIMUM_N = 100;
REDUCED_MATRIX = 1;
K = [3,5];
K_PARAMETER = length(K);
SAVE_COEFFICIENT = 1;
GAINPARAMETER = 4;
NUMBER_ITERATION = 1;
Hx = 100;
Opt = 2;
Vz = [0, 105];
Ve = [];
Vo = [];

system("date +%Y%m%d%H%M%S > temptime.txt");
mytime = read("temptime.txt");

/* generate output file name */
OUTPUTFILE = concat(["result_K", Str(matsize(K)[2]),"_Vz" ,\
                     Str(Vz[2]), "_", MYID, "_", mytime]);
CONFIGFILE = concat(["config_K", Str(matsize(K)[2]),"_Vz" , \
                     Str(Vz[2]), "_", MYID, "_", mytime, ".log"]);

/* construct the vector of N*/
NVectorTemp = vector(MAXIMUM_N-MINIMUM_N+1,x,x+MINIMUM_N-1);
LengthNVector = length(NVectorTemp);
NVector = [];
for(index1 = 1,LengthNVector,
    if(eulerphi(NVectorTemp[index1])<= EULER_LIMIT && \
       NVectorTemp[index1]%4 == 0,
       NVector = concat(NVector,NVectorTemp[index1])
    );
);
```

```
/* construct the vector of N*/
for(count = 1,length(NVector),
    print("\n-------------------------------------\n");
    print(concat("Vector index: ", Str(count)));

    TIMEBOUND = floor(NVector[count]^3*\
                      (eulerphi(NVector[count]))^2/4147979673.0);
    Hx = round(NVector[count]/2 + 2);
    MULTHRESHOLD = GAINPARAMETER*eulerphi(NVector[count]);
    system("rm -f parameter.gp");
    write("parameter.gp", \
          concat(["N = ", Str(NVector[count]), \
                  ";\nK = ",Str(K_PARAMETER), ";\n", \
                  "MULTHRESHOLD = ", Str(MULTHRESHOLD), ";\n", \
                  "REDUCED_MATRIX = ", Str(REDUCED_MATRIX), ";\n", \
                  "OUTPUTFILE = \"", OUTPUTFILE, "\";\n", \
                  "CONFIGFILE = \"", CONFIGFILE, "\";\n", \
                  "K = ", Str(K), ";\n", \
                  "Vz = ", Str(Vz), ";\n", \
                  "Ve = ", Str(Ve), ";\n", \
                  "Vo = ", Str(Vo), ";\n", \
                  "Opt = ", Str(Opt), ";\n", \
                  "Hx = ", Str(Hx), ";\n"]));

    system(concat(["./run-with-timeout.sh ", \
                   Str(TIMEBOUND), " gp -s 1G -q runscript1.gp"]));
); /* end for(count */

/* remove temporary file */
system("rm -f temptime.txt");

/* quit gp */
quit();
}
```

```
#!/bin/bash
# Name: run-with-timeout.sh
if [ $# -lt 2 ] ; then
    echo "usage: $0 <timeout-in-seconds> <command> [args...]"
    exit 2
fi

timeout=$1
shift
end=$(expr $(date +%s) + $timeout)

echo "timeout: $timeout"
echo "cmd: $@"
"$@" &
pid=$!

ok-to-kill() {
    if [ -e /tmp/flag ] ; then
return 1  # don't kill it
    else
return 0  # ok to kill
    fi
}

while kill -0 $pid 2>/dev/null; do
    if [ $(date +%s) -ge $end ] && ok-to-kill ; then
echo killing it now
kill -INT $pid 2>/dev/null
sleep 1
kill -KILL $pid 2>/dev/null
sleep 1
    else
sleep 0.25
    fi
done

if wait $pid ; then
    echo "success"
else
    echo "failed"
fi
```

# Bibliography


[1] Public Law 110-140, 2007.

[2] Institute for Energy Efficiency. (2010) Utility-scale smart meter deployments, plans & proposals, september 2010. [Online]. Available: http://www.edisonfoundation.net/IEE/issuebriefs/SmartMeter_Rollouts_0910.pdf

[3] Office of Gas and Electricity Market, UK. (2010) Smart metering. [Online]. Available: http://www.ofgem.gov.uk/e-serve/sm/Pages/sm.aspx

[4] ——. (2010) Energy demand research project: Review of progress for the period march 2009 – september 2009. [Online]. Available: http://www.ofgem.gov.uk/Sustainability/EDRP/Documents1/EDRP%20Progress%20Report%204%20final.pdf

[5] S. B. Leeb, S. R. Shaw, and J. L. Kirtley, "Transient event detection in spectral envelope estimates for nonintrusive load monitoring," *IEEE Trans. Power Del.*, vol. 10, no. 3, pp. 1200 1210, Jul 1995.

[6] S. R. Shaw, S. B. Leeb, L. K. Norford, and R. W. Cox, "Nonintrusive load monitoring and diagnostics in power systems," *IEEE Trans. Instrum. Meas.*, vol. 57, no. 7, pp. 1445 1454, Jul 2008.

[7] A. Cole and A. Albicki, "Nonintrusive identification of electrical loads in a three-phase environment based on harmonic content," in *Proc. IMTC 2000*, vol. 1, May 2000.

[8] C. R. Laughman, S. R. Shaw, S. B. Leeb, L. K. Norford, R. W. Cox, K. D. Lee, and P. Armstrong, "Power signature analysis," *IEEE Power and Energy Magazine*, pp. 56–63, March 2003.

[9] K. D. Lee, "Electric load information system based on non-intrusive power monitoring," Ph.d. Thesis, Mass. Inst. of Tech., Jun 2003.

[10] J. S. Ramsey, S. B. Leeb, T. DeNucci, J. Paris, M. Obar, R. Cox, C. Laughman, and T. J. McCoy, "Shipboard applications of non-intrusive load monitoring," in *American Society of Naval Engineers Reconfigurability and Survivability Symposium*, Atlantic Beach, Florida, February 2005.

[11] T. DeNucci, R. Cox, S. B. Leeb, J. Paris, T. J. McCoy, C. Laughman, and W. Greene, "Diagnostic indicators for shipboard systems using non-intrusive load monitoring," in *IEEE Electric Ship Technologies Symposium*, Philadelphia, Pennsylvania, July 2005.

[12] K. D. Lee, S. B. Leeb, L. K. Norford, P. R. Armstrong, J. Holloway, and S. R. Shaw, "Estimation of variable-speed-drive power consumption from harmonic content," *IEEE Trans. Energy Convers.*, vol. 20, no. 3, pp. 566–574, Sep 2005.

[13] R. W. Cox, P. Bennett, D. McKay, J. Paris, and S. B. Leeb, "Using the non-intrusive load monitor for shipboard supervisory control," in *IEEE Electric Ship Technologies Symposium*, Arlington, VA, May 2007.

[14] S. R. Shaw and C. Laughman, "A kalman-filter spectral envelope preprocessor," *IEEE Trans. Instrum. Meas.*, vol. 56, no. 5, pp. 2010–2017, Oct 2007.

[15] E. Proper, R. W. Cox, S. B. Leeb, K. Douglas, J. Paris, W. Wichakool, L. Foulks, R. Jones, P. Branch, A. Fuller, J. Leghorn, and G. Elkins, "Field demonstration of a real-time non-intrusive monitoring system for condition-based maintenance," in *Electric Ship Design Symposium*, National Harbor, Maryland, February 2009.

[16] J. Paris, Z. Remscrim, K. Douglas, S. B. Leeb, R. W. Cox, S. T. Gavin, S. G. Coe, J. R. Haag, and A. Goshorn, "Scalability of non-intrusive load monitoring for shipboard applications," in *American Society of Naval Engineers Day 2009*, National Harbor, Maryland, April 2009.

[17] W. Wichakool, A. Avestruz, R. W. Cox, and S. B. Leeb, "Modeling and estimating current harmonics of variable electronic loads," *IEEE Trans. Power Electron.*, no. 12, pp. 2803 2811, Dec 2009.

[18] U. Orji, Z. Remscrim, C. Laughman, S. Leeb, W. Wichakool, C. Schantz, R. Cox, J. Paris, J. Kirtley, and L. Norford, "Fault detection and diagnostics for non-intrusive monitoring using motor harmonics," Feb. 2010, pp. 1547 –1554.

[19] Z. Remscrim, "The theory and applicaiton of non-intrusive load monitoring," Master's thesis, MIT, 2010.

[20] R. W. Cox, J. Mosman, T. McKay, S. B. Leeb, and T. McCoy, "Diagnostic indicators for shipboard cycling systems using non-intrusive load monitoring," in *American Society of Naval Engineers Day 2006*, Arlington, VA, June 2006.

[21] R. W. Cox, G. Mitchell, P. Bennet, M. Piber, J. Paris, W. Wichakool, and S. B. Leeb, "Improving shipboard maintenance practices using non-intrusive load monitoring," in *American Society of Naval Engineers Intelligent Ships Symposium VII*, Philadelphia, PA, May 2007.

[22] T. W. DeNucci, "Diagnostic indicators for shipboard systems using non-intrusive load monitoring," Master Thesis, Mass. Inst. of Tech., Jun 2005.

[23] J. P. Mosman, "Evaluation of non-intrusive load monitoring for shipboard cycling system diagnostics," Master Thesis, Mass. Inst. of Tech., Jun 2006.

[24] M. A. Piber, "Improving shipboard maintenance practices using non-intrusive load monitoring," Master Thesis, Mass. Inst. of Tech., Jun 2007.

[25] D. Son and J. D. Seivert, "A new current sensor based on the measurement of the apparent coercive field strength," *IEEE Trans. Instrum. Meas.*, vol. 38, no. 6, pp. 1080–1082, Dec 1989.

[26] S. Ogasawara, K. Murata, and H. Akagi, "A digital current sensor for pwm inverters," in *Industry Applications Society Annual Meeting, 1992., Conference Record of the 1992 IEEE*, vol. 1, Oct 1992, pp. 949–955.

[27] T. Sonoda, R. Ueda, and K. Koga, "An ac and dc current sensor of high accuracy," *IEEE Trans. Ind. Appl.*, vol. 28, no. 5, pp. 1087–1094, Sept/Oct 1992.

[28] J. Pankau, D. Leggate, D. Schlegel, R. Kerkman, and G. Shibiniski, "High frequency modeling of current sensors," *IEEE Trans. Ind. Appl.*, vol. 35, no. 6, pp. 1374–1382, Nov/Dec 1999.

[29] D. Li and G. Chen, "A wide bandwidth current probe based on rogowski coil and hall sensor," in *Power Electronics and Motion Control Conference, 2006. IPEMC 2006. CES/IEEE 5th International*, vol. 2, Aug 2006, pp. 1–5.

[30] J. Lenz and A. S. Edelstein, "Magnetic sensors and their applications," *IEEE Sensors J.*, vol. 6, no. 3, pp. 631–649, Jun 2006.

[31] M. M. Ponjavić and R. Durić, "Nonlinear modeling of the self-oscillating fluxgate current sensor," *IEEE Sensors J.*, vol. 7, no. 11, pp. 1546–1553, Nov 2007.

[32] C. Moreland, F. Murden, M. Elliott, J. Young, M. Hensley, and R. Stop, "A 14-bit 100-msample/s subranging adc," *IEEE J. Solid-State Circuits*, vol. 35, no. 12, pp. 1791–1798, Dec 2000.

[33] K. D. Hurst and T. G. Habetler, "Sensorless speed measurement using current harmonic spectral estimation in induction machine drives," *IEEE Trans. Power Electron.*, vol. 11, no. 1, pp. 66–73, 1996.

[34] J. Paris, Ph.d. Thesis, Mass. Inst. of Tech., to be published.

[35] S. W. D. Haan, "Analysis of the effect of source voltage fluctuations on the power factor in three-phase controlled rectifiers," *IEEE Trans. Ind. Appl.*, vol. IA-22, no. 2, pp. 259–266, Mar 1986.

[36] Y. Baghzouz, "An accurate solution to line harmonic distortion produced by ac/dc converters with overlap and dc ripple," *IEEE Trans. Ind. Appl.*, vol. 29, no. 3, pp. 536–540, May/Jun. 1993.

[37] M. Sakui and H. Fujita, "An analytical method for calculating harmonic currents of a three-phase diode-bridge rectifier with dc filter," *IEEE Trans. Power Electron.*, vol. 9, no. 6, pp. 631–637, Nov. 1994.

[38] D. E. Rice, "A detailed analysis of six-pulse converter harmonic currents," *IEEE Trans. Ind. Appl.*, vol. 30, no. 2, pp. 294–304, Mar./Apr. 1994.

[39] W. Xu, H. W. Dommel, M. B. Hughes, G. W. Chang, and L. Tan, "Modelling of adjustable speed drives for power system harmonic analysis," *IEEE Trans. Power Del.*, vol. 14, no. 2, pp. 595–601, Apr. 1999.

[40] M. Grötzbach and R. Redmann, "Line current harmonics of vsi-fed adjustable-speed drive," *IEEE Trans. Ind. Appl.*, vol. 36, no. 2, pp. 683–690, Mar./Apr. 2000.

[41] M. Grötzbach and M. Bauta, "Modeling of ac/dc converters under unbalanced voltage supply using complex switching functions," in *Proc. in Harmonics and Quality of Power*, vol. 2, Nov. 2002.

[42] V. Caliskan, D. J. Perreault, T. M. Jahns, and J. G. Kassakian, "Analysis of three-phase rectifiers with constant-voltage loads," *IEEE Trans. Circuits Syst.*, vol. 50, no. 9, pp. 1220–1226, Nov. 2003.

[43] F. Wang, G. Chen, D. Boroyevish, S. Ragon, M. Arpilliere, and V. R. Stefanovic, "Analysis and design optimization of diode front-end rectifier passive components for voltage source inverters," *IEEE Trans. Power Electron.*, vol. 23, no. 5, pp. 2278–2289, Sep. 2008.

[44] L. C. Washington, *Introduction to Cyclotomic Fields*, 2nd ed. Springer, 1997.

[45] J. H. W. Lenstra, "Euclid's algorithm in cyclotomic fields," *Journal of the London Mathematical Society*, vol. 2, no. 10, pp. 457–465, 1975.

[46] J. M. Masley and H. L. Montgomery, "Cyclotomic fields with unique factorization," *Journal fr die reine und angewandte Mathematik*, no. 286 - 287, pp. 248 256, 1976.

[47] A. V. Oppenheim, R. W. Schafer, and J. R. Buck, *Discrete-time Signal Processing*, 2nd ed. Prentice-Hall, 1999.

[48] K. Belabas. (2010) PARI/GP development headquarters. [Online]. Available: http://pari.math.u-bordeaux.fr/